

# AD-A239 269

## ITATION PAGE

Form Approved  
OMB No. 0704-0188



ed to Average 1 hour per response, including the time for reviewing instructions, searching existing data sources, viewing the collection of information. Send comments regarding this burden estimate or any other aspect of this order to Washington Headquarters Services, Directorate for Information Operations and Reports, 1215 Jefferson Office of Management and Budget, Paperwork Reduction Project (0704-0188), Washington, DC 20503

1. AGENCY USE ONLY (Leave blank)		2. REPORT DATE		3. REPORT TYPE AND DATES COVERED <del>TEXTS</del> /DISSERTATION	
4. TITLE AND SUBTITLE Oscillating Shock Impingement on Low-Angle Gas Injection into a Supersonic Flow				5. FUNDING NUMBERS	
6. AUTHOR(S) Charles W. Wood, Major					
7. PERFORMING ORGANIZATION NAME(S) AND ADDRESS(ES) AFIT Student Attending: Virginia Polytechnic Institute & State University				8. PERFORMING ORGANIZATION REPORT NUMBER AFIT/CI/CIA-91-008d	
9. SPONSORING / MONITORING AGENCY NAME(S) AND ADDRESS(ES) AFIT/CI Wright-Patterson AFB OH 45433-6583				10. SPONSORING / MONITORING AGENCY REPORT NUMBER	
11. SUPPLEMENTARY NOTES					
12a. DISTRIBUTION / AVAILABILITY STATEMENT Approved for Public Release IAW 190-1 Distributed Unlimited ERNEST A. HAYGOOD, 1st Lt, USAF Executive Officer				12b. DISTRIBUTION CODE	
13. ABSTRACT (Maximum 200 words)					
14. SUBJECT TERMS				15. NUMBER OF PAGES 191	
				16. PRICE CODE	
17. SECURITY CLASSIFICATION OF REPORT		18. SECURITY CLASSIFICATION OF THIS PAGE		19. SECURITY CLASSIFICATION OF ABSTRACT	
20. LIMITATION OF ABSTRACT					

36 **91-07355**

**OSCILLATING SHOCK IMPINGEMENT ON LOW-ANGLE GAS INJECTION  
INTO A SUPERSONIC FLOW**

by

Charles W. Wood

Major, USAF

1991

191 Pages

PhD, Aerospace Engineering

Virginia Polytechnic Institute & State University



A-1

OSCILLATING SHOCK IMPINGEMENT ON LOW-ANGLE GAS INJECTION  
INTO A SUPERSONIC FLOW

by

Charles Wade Wood

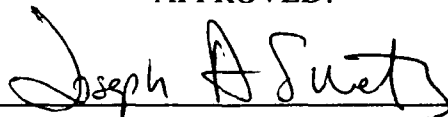
Dissertation Submitted to the Faculty of the  
Virginia Polytechnic Institute and State University  
in partial fulfillment of the requirements for the degree of

DOCTOR OF PHILOSOPHY

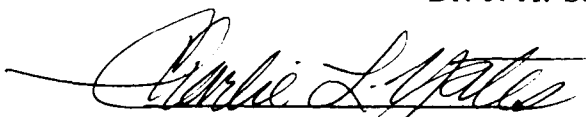
in

Aerospace Engineering

APPROVED:



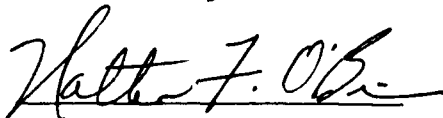
Dr. J. A. Schetz, Chairman



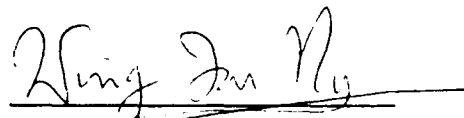
Dr. C. L. Yates



Dr. A. L. Wicks



Dr. W. F. O'Brien



Dr. W. F. Ng

April, 1991  
Blacksburg, Virginia

**OSCILLATING SHOCK IMPINGEMENT ON LOW-ANGLE GAS INJECTION  
INTO A SUPERSONIC FLOW**

by

Charles Wade Wood

Joseph A. Schetz, Chairman

Aerospace Engineering

(ABSTRACT)

Experiments were performed to determine the effects of impinging oscillating shocks of different frequencies on a 15° downstream angled, underexpanded, sonic helium jet injected into a supersonic airflow. Information on mixing, penetration, total pressure loss and turbulence structure from these experiments was used to estimate mixing control achieved by adding an oscillating shock to the helium injection flow field. Tests were conducted at Mach 3.0, with a total pressure of 6.5 atm, a total temperature of 290 K and a Reynolds number of  $51.0 \times 10^6$  per meter. Oscillating shocks of three different frequencies were studied. The frequencies selected were designed to allow tuning of the shock frequency to the estimated frequency, about 100 - 150 kHz, of the largest eddies in the approach boundary layer. Visualization using nanoshadowgraph photography showed large turbulent structures in all cases. In addition, there were clear changes in eddy size with changing shock frequency visible on the nanoshadowgraphs. The primary measurement made for the mixing studies was the molar concentration of helium. Concentration data, as well as mean flow data, was collected at nine lateral positions at each of three axial stations downstream of the helium injector. The resulting data

produced contours of helium concentration, total pressure, Mach number, velocity, mass flux and static flow properties. Additional tests were conducted to determine the shock oscillation frequency, the correlation between the oscillating shock and the turbulence in the shear layer and the angle of large-scale structures in the flow. Mixing and penetration rates were determined from the helium concentration data. The major result of this study was that impingement of an oscillating shock on a high-speed shear layer can be used to control the rate of mixing. Depending on the shock oscillation frequency, mixing enhancement or inhibition can be produced. It was found that increasing shock oscillation frequency resulted in more rapid injectant concentration decay and increased freestream air entrainment leading to a stoichiometric H<sub>2</sub>-air mixture ratio while also reducing penetration of the helium injectant. A strong correlation was found between the highest frequency shock and changes in the mixing flow field. The maximum oscillation frequency was approximately 140 kHz, which was consistent with numerical estimates for the frequency necessary for mixing augmentation under these test conditions. It was concluded that oscillating shock impingement has promise as a means of controlling gaseous mixing in a high-speed cross-flow.

## ACKNOWLEDGEMENTS

I would like to thank Dr. J.A. Schetz for his advice, encouragement, expertise, and support during the course of this study. I would also like to thank Dr. W.F. O'Brien, Dr. C.L. Yates, and Dr. W.F. Ng for serving as members of my committee. Thanks are also due to Dr. A.L. Wicks for his advice and help with many of my signal processing questions and for substituting on my committee at the last minute.

Next, I would like to thank two of my fellow students, Rich Mays and Eric Fuller, for their help and advice on this project. I am also indebted to Ken Chadwick, Rodney Bowersox, Phil Andrew, Gary Stafford, Peter King, Olivier Ferrandon, and John Mills for their contributions. Thanks are also in order for Frank Shelor, Jake Frazier, and Kent Morris of the AOE Shop for their help in making or modifying hardware for these experiments.

I am also grateful to the NASA Langley Experimental Flow Physics Branch, D. Bushnell, S. Robinson, and M. Walsh for their support of this project.

Thanks also to the United States Air Force Academy and the Air Force Institute of Technology for providing this educational opportunity.

Sincere and everlasting gratitude is due my wife, Melissa, and our two terrific sons, Doug and Jeff, for their loving support and many sacrifices during the course of this investigation. Extra special thanks are also due to my wife for typing this manuscript.

## TABLE OF CONTENTS

NOMENCLATURE .....	ix
LIST OF TABLES .....	xiii
LIST OF FIGURES .....	xiv
1. INTRODUCTION .....	1
2. DESCRIPTION OF THE EXPERIMENT .....	8
2.1 General Description .....	8
2.2 Facilities and Equipment .....	12
2.2.1 The Wind Tunnel .....	12
2.2.2 Helium Injector Model .....	13
2.2.3 Water Injector Model .....	14
2.2.4 Helium Supply System .....	15
2.2.5 Water Supply System .....	16
2.2.6 Traversing System .....	17

2.3	Instrumentation . . . . .	18
2.3.1	Tunnel Control Computer . . . . .	18
2.3.2	Data Acquisition Systems . . . . .	18
2.3.3	Stagnation Properties . . . . .	20
2.3.4	Optical System . . . . .	21
2.3.5	The Helium Concentration Probe . . . . .	21
2.3.6	Other Mean Flow Probes . . . . .	23
2.3.7	Position Measurement . . . . .	24
2.3.8	Kulite Pressure Transducer . . . . .	25
2.3.9	Hot-Wire Probes . . . . .	25
2.4	Experimental Methods . . . . .	27
2.4.1	Calibrations . . . . .	27
2.4.2	Data Acquisition Procedure . . . . .	30
2.4.3	Concentration Reduction . . . . .	31
2.4.4	Mean Flow Reduction . . . . .	32
2.4.5	Eddy Structure Angle Reduction . . . . .	36
2.4.6	Kulite / Hot-Wire Reduction . . . . .	37
2.4.7	Nondimensionalization Scheme . . . . .	40
3.	RESULTS . . . . .	42
3.1	Nanoshadowgraphs . . . . .	42



3.2	Shock Frequency Results . . . . .	48
3.3	Helium Concentration Data . . . . .	50
	3.3.1 General Flowfield Structure . . . . .	50
	3.3.2 Helium Concentration Decay . . . . .	52
	3.3.3 Jet Core Penetration . . . . .	54
3.4	Other Mean Flow Results . . . . .	55
	3.4.1 Total Pressure Contours . . . . .	55
	3.4.2 Mach Number Profiles . . . . .	59
	3.4.3 Static Properties . . . . .	60
	3.4.4 Integrated Mass Flow Rate . . . . .	61
	3.4.5 Entrainment . . . . .	61
3.5.	Combined Kulite/Hot Wire Tests . . . . .	63
3.6	Parallel Array Results . . . . .	66
4.	DISCUSSION . . . . .	67
5.	CONCLUSIONS AND RECOMMENDATIONS . . . . .	73
	BIBLIOGRAPHY . . . . .	77
	TABLES . . . . .	80

<b>FIGURES</b> .....	<b>90</b>
<b>APPENDIX A: ERROR ANALYSIS</b> .....	<b>171</b>
<b>VITA</b> .....	<b>174</b>

## NOMENCLATURE

$a$	speed of sound
$a$	concentration probe calibration constant
$A$	area
$b$	concentration probe calibration constant
$d$	helium injector diameter
$d_j$	water injector diameter
$D$	discharge coefficient
$f$	frequency
$f$	function
$G_{xx}$	auto-spectral density function
$G_{yy}$	auto-spectral density function
$G_{xy}$	cross-spectral density function
$HW$	hot-wire
$k$	thermal conductivity
$l$	hot-film length
$m$	concentration probe calibration constant
$\dot{m}$	mass flow rate
$M$	Mach number
$MW$	molecular weight
$n_1$	concentration decay rate

$n_2$	core penetration rate
$n_d$	number of data blocks
$N$	samples
$N_w$	jet column wave frequency
$P$	power
$P$	pressure
$q$	dynamic pressure
$\bar{q}$	dynamic pressure ratio, $(\rho U^2)_j/(\rho U^2)_\infty$
$R$	resistance
$R$	gas constant
$Re$	Reynolds number
$S_{12}$	cross-correlation function
$S_{11}$	auto-correlation function
$t$	time
$T$	temperature
$U$	streamwise velocity
$U_e$	edge velocity
$V$	voltage
$w$	wire separation distance
$x$	axial distance downstream of helium jet
$X$	signal
$y$	transverse coordinate, width across jet

$Y$	signal
$z$	vertical coordinate, height above floor
$z/d_{\max}$	vertical location of maximum concentration
$\alpha$	mass fraction
$\beta$	probe inclination angle
$\beta_1$	concentration decay rate intercept
$\beta_2$	core penetration intercept
$\gamma$	ratio of specific heats
$\hat{\gamma}_{xy}^2$	coherence function
$\delta$	boundary layer thickness
$\epsilon$	time delay
$\theta$	structure angle
$\mu$	viscosity
$\rho$	density
$\rho U$	mass flux
$\sigma$	surface tension of liquid
$\varphi$	phase factor
$\chi$	mole fraction
Subscripts	
c	cone-static
crit	critical
ent	entrained

fs	free stream
He	helium
i	imaginary
j	liquid jet
l	liquid
max	maximum
mix	mixture
r	real
RMS	root mean square
s	series
struct	structure
t	total/stagnation
w	wire/film property at operating temperature
$\infty$	freestream
1	before normal shock
1	local property
2	after normal shock
<b>Superscripts</b>	
*	complex conjugate

## LIST OF TABLES

Table 1. Test Conditions and Parameters . . . . .	81
Table 2. Maximum Helium Concentrations ( $\alpha_{max}$ ) . . . . .	82
Table 3. Locations of Maximum Concentration ( $z/d_{max}$ ) . . . . .	83
Table 4. Mixing Distance and Decay Exponent . . . . .	84
Table 5. Penetration Growth Rate Exponents . . . . .	85
Table 6. Total Pressure Loss Parameter . . . . .	86
Table 7. Integrated Mass Flow Rates (kg/s) . . . . .	87
Table 8. Air Entrainment Rates (kg/s) . . . . .	88
Table 9. Parallel Array Results . . . . .	89

## LIST OF FIGURES

Figure 1. Example Scramjet Operating Conditions . . . . .	91
Figure 2. Virginia Tech Wind Tunnel . . . . .	92
Figure 3. Sketch of Test Setup . . . . .	93
Figure 4. Sketch of Helium Injector . . . . .	94
Figure 5. The Test Stations . . . . .	95
Figure 6. Water Injector Model . . . . .	96
Figure 7. Schematic of Water Injection System . . . . .	97
Figure 8. Sketch of the Nanoshadowgraph Optical System . . . . .	98
Figure 9. Concentration Probe Schematic . . . . .	99
Figure 10. Concentration Probe Hot-Film Sensor . . . . .	100
Figure 11. Pitot Pressure Probe . . . . .	101
Figure 12. Total Temperature Probe . . . . .	102
Figure 13. Cone-Static Probe . . . . .	103
Figure 14. Concentration Probe Calibration Curves . . . . .	104
Figure 15. Sketch for Structure Angle Calculation . . . . .	105
Figure 16. Nanoshadowgraph of Baseline Helium Injection . . . . .	106
Figure 17. Nanoshadowgraph of Combined Injection ( $d_i = 0.159$ cm) . . . . .	107
Figure 18. Nanoshadowgraph of Combined Injection ( $d_i = 0.079$ cm) . . . . .	108
Figure 19. Nanoshadowgraph of Combined Injection ( $d_i = 0.040$ cm) . . . . .	109
Figure 20. Kulite Power Spectrum, Baseline Injection . . . . .	110
Figure 21. Kulite Power Spectrum, Combined Injection ( $d_i = 0.159$ cm) . . . . .	111



Figure 22. Kulite Power Spectrum, Combined Injection ( $d_j = 0.040$ cm) . . . . .	112
Figure 23. Helium Concentration, Baseline Injection, $x/d = 20$ . . . . .	113
Figure 24. Helium Concentration, Baseline Injection, $x/d = 40$ . . . . .	114
Figure 25. Helium Concentration, Baseline Injection, $x/d = 90$ . . . . .	115
Figure 26. Helium Concentration, Combined Injection, $x/d = 20$ . . . . .	116
Figure 27. Helium Concentration, Combined Injection, $x/d = 40$ . . . . .	117
Figure 28. Helium Concentration, Combined Injection, $x/d = 90$ . . . . .	118
Figure 29. Helium Concentration, Combined Injection, $x/d = 20$ . . . . .	119
Figure 30. Helium Concentration, Combined Injection, $x/d = 40$ . . . . .	120
Figure 31. Helium Concentration, Combined Injection, $x/d = 90$ . . . . .	121
Figure 32. Helium Concentration, Combined Injection, $x/d = 20$ . . . . .	122
Figure 33. Helium Concentration, Combined Injection, $x/d = 40$ . . . . .	123
Figure 34. Helium Concentration, Combined Injection, $x/d = 90$ . . . . .	124
Figure 35. Helium Concentration Decay . . . . .	125
Figure 36. Core Penetration . . . . .	126
Figure 37. Total Pressure Contours, Baseline Injection, $x/d = 20$ . . . . .	127
Figure 38. Total Pressure Contours, Combined Injection, $x/d = 20$ . . . . .	128
Figure 39. Total Pressure Contours, Combined Injection, $x/d = 20$ . . . . .	129
Figure 40. Total Pressure Contours, Combined Injection, $x/d = 20$ . . . . .	130
Figure 41. Total Pressure Contours, Baseline Injection, $x/d = 40$ . . . . .	131
Figure 42. Total Pressure Contours, Combined Injection, $x/d = 40$ . . . . .	132
Figure 43. Total Pressure Contours, Combined Injection, $x/d = 40$ . . . . .	133

Figure 44. Total Pressure Contours, Combined Injection, $x/d = 40$ . . . . .	134
Figure 45. Total Pressure Contours, Baseline Injection, $x/d = 90$ . . . . .	135
Figure 46. Total Pressure Contours, Combined Injection, $x/d = 90$ . . . . .	136
Figure 47. Total Pressure Contours, Combined Injection, $x/d = 90$ . . . . .	137
Figure 48. Total Pressure Contours, Combined Injection, $x/d = 90$ . . . . .	138
Figure 49. Mach Number Contours, Baseline Injection, $x/d = 20$ . . . . .	139
Figure 50. Mach Number Contours, Combined Injection, $x/d = 20$ . . . . .	140
Figure 51. Mach Number Contours, Combined Injection, $x/d = 20$ . . . . .	141
Figure 52. Mach Number Contours, Combined Injection, $x/d = 20$ . . . . .	142
Figure 53. Typical Velocity Contour, Combined Injection, $x/d = 20$ . . . . .	143
Figure 54. Mach Number Contours, Baseline Injection, $x/d = 90$ . . . . .	144
Figure 55. Mach Number Contours, Combined Injection, $x/d = 90$ . . . . .	145
Figure 56. Mach Number Contours, Combined Injection, $x/d = 90$ . . . . .	146
Figure 57. Mach Number Contours, Combined Injection, $x/d = 90$ . . . . .	147
Figure 58. Velocity Contours, Baseline Injection, $x/d = 90$ . . . . .	148
Figure 59. Velocity Contours, Combined Injection, $x/d = 90$ . . . . .	149
Figure 60. Velocity Contours, Combined Injection, $x/d = 90$ . . . . .	150
Figure 61. Velocity Contours, Combined Injection, $x/d = 90$ . . . . .	151
Figure 62. Typical Static Pressure Contours, Combined Injection, $x/d = 90$ . .	152
Figure 63. Static Temperature Contours, Baseline Injection, $x/d = 20$ . . . . .	153
Figure 64. Static Temperature Contours, Combined Injection, $x/d = 20$ . . . . .	154
Figure 65. Static Temperature Contours, Combined Injection, $x/d = 20$ . . . . .	155

Figure 66. Static Temperature Contours, Combined Injection, $x/d = 20$ . . . . .	156
Figure 67. Static Temperature Contours, Baseline Injection, $x/d = 90$ . . . . .	157
Figure 68. Static Temperature Contours, Combined Injection, $x/d = 90$ . . . . .	158
Figure 69. Static Temperature Contours, Combined Injection, $x/d = 90$ . . . . .	159
Figure 70. Static Temperature Contours, Combined Injection, $x/d = 90$ . . . . .	160
Figure 71. Helium Mass Flux, Baseline Injection, $x/d = 90$ . . . . .	161
Figure 72. Helium Mass Flux, Combined Injection, $x/d = 90$ . . . . .	162
Figure 73. Helium Mass Flux, Combined Injection, $x/d = 90$ . . . . .	163
Figure 74. Helium Mass Flux, Combined Injection, $x/d = 90$ . . . . .	164
Figure 75. Coherence Function, Combined Injection ( $d_j = 0.079$ ) . . . . .	165
Figure 76. Coherence Function, Combined Injection ( $d_j = 0.040$ ) . . . . .	166
Figure 77. Hot-Wire Power Spectrum, Baseline Injection . . . . .	167
Figure 78. Hot-Wire Power Spectrum, Combined Injection ( $d_j = 0.159$ ) . . . . .	168
Figure 79. Hot-Wire Power Spectrum, Combined Injection ( $d_j = 0.079$ ) . . . . .	169
Figure 80. Hot-Wire Power Spectrum, Combined Injection ( $d_j = 0.040$ ) . . . . .	170

## 1. INTRODUCTION

When the National Aerospace Plane (NASP) was announced in January 1986, it represented the most ambitious undertaking, to date, in the field of hypersonic flight. It was intended to be a single stage to orbit, primarily airbreathing, vehicle for use in research and development and leading to future vehicle concepts based on the knowledge gained in this program. High speed airbreathing propulsion was not new when the program was announced. The ramjet, using subsonic combustion, had been studied as early as the 1930's by Leduc and saw further development after World War II.<sup>1</sup> In such a propulsion device, supersonic air was slowed to below Mach 1.0 before fuel was added in the combustor. This was acceptable at speeds up to approximately Mach 5.0, but above Mach 5.0, at speeds needed for the NASP, there is a severe reduction in total pressure recovery of the inlet system and an extreme rise in static temperature at the combustor entrance, if the flow is decelerated below Mach 1.0. This results in increased dissociation of combustion products and an increase in losses associated with the frozen flow expansion process.<sup>2</sup> Some of these problems can be countered by allowing the combustion to take place at supersonic velocities using a scramjet, or supersonic combustion ramjet.

One of the most important and persistent problems in scramjet propulsion is fuel/air mixing and combustion.<sup>3</sup> Figure 1 shows typical engine flow conditions for a scramjet operating at Mach 25.0 at 200,000 feet. As can be seen in the figure, combustor velocities are on the order of  $10^4$  ft/sec. It is also necessary to keep the

combustor length down to reduce wall heat transfer, to reduce viscous losses due to wall shear, and to avoid adding excess weight to the flight vehicle. The combination of high combustor velocity and the desire for minimum length leads to residence times of  $10^{-3}$  to  $10^{-4}$  sec. This short time drives the need for rapid entrainment and fuel/air mixing followed by significant energy release in the combustor. The inherently low mixing rates at high Mach numbers necessitate a better understanding of the mixing and mixing augmentation processes.<sup>3,4</sup> A further overview of the scramjet mixing problem can be found in Ref. 5.

Studies have been conducted on the use of liquid fuels for scramjets as well as the use of gaseous fuels, such as hydrogen, with its high energy release.<sup>6</sup> The use of gaseous fuels has gained interest over the past several years and many researchers have looked at the problem of penetration and mixing of gases injected into a supersonic stream.

An overview and analysis of much of the experimental data on gaseous injection can be found in Ref. 7. That work reviews the available data on injection of light gases into a supersonic air stream with emphasis on the experiments where downstream species concentration measurements were available.

One of the most studied cases is that of normal injection into a supersonic flow. Schetz and Billig<sup>8</sup> presented an analysis of this configuration and extended subsonic solid body models to supersonic flows to develop a method for predicting the trajectory of the injected gas. Their predictions were found to agree closely with experiment. Schetz and Billig also introduced the effective back pressure concept. This pressure was defined as the average pressure between the jet interaction shock and the jet itself. It can be thought

of as the pressure to which the jet will expand after leaving the injector. The jet expansion ratio was then defined as the ratio of the static pressure at the injector exit plane to the effective back pressure. Thus, an underexpansion would be indicated by an expansion ratio greater than 1. While this analysis predicted the jet trajectory very well, it could not be used to predict downstream mixing. Cohen, Coulter and Egan<sup>9</sup> performed experiments to study the penetration and mixing of non-reacting gases injected into subsonic and supersonic air flows. They used schlieren photographs, total temperature measurements and species concentration profiles to develop correlations for penetration height, distance required to achieve two-dimensional flow and kinematic eddy viscosity. Among other things, they found that using upstream blowing dramatically increased both penetration and mixing rate.

While normal injection shows significant penetration, there is no downstream fuel momentum contribution. This can be overcome by means such as downstream facing slot injection. Kwok, et al, Ref. 10, and others have studied such a flow configuration. They found that there was very poor initial penetration and mixing in this configuration. In addition they saw a small total pressure loss in the helium injection studied.

One compromise between normal injection and slot injection would be to angle the injector at some angle between those two extremes. Mays<sup>11</sup> summarized the downstream angled work of McClinton who looked at transverse angles as low as 30° and extended that work studying injection angles of 15° and 30° with matched exit pressures and with a 5X underexpanded exit condition. Mays found that the underexpanded jets showed substantially better penetration and mixing than the matched jets. When total

pressure losses were considered with the decay rates and penetration results, Mays concluded that the 15° underexpanded jet was the best case of the four he studied.

In addition to studies of various injection schemes, both experimental and computational studies have been conducted on other means to enhance the supersonic mixing process. Many of these studies have involved the interaction of a shock wave with the mixing region and have studied the changes due to such an interaction. Marble, et al, (Ref. 12) performed computational and experimental studies in which a weak shock interacted with a fuel jet flowing parallel to the air stream and the combustor wall. The interaction between the nominally steady shock and the flow generated strong longitudinal vorticity which in turn caused rapid distortion in the fuel-air interface. This distortion caused a greatly increased mixing rate.

Menon<sup>13</sup> also studied a steady shock mixing enhancement configuration. In this work, a steady shock, generated by a wedge in the flow, was caused to impinge on a shear layer downstream of a rearward facing step. Preliminary results indicated there may be increased spreading of the shear layer downstream of the shock/shear layer interaction region. A similar study by Shau and Dolling<sup>14</sup> found little effect of the shock on spreading rate either near the shock or further downstream of the interaction zone.

Kumar, Bushnell and Hussaini<sup>4</sup> performed numerical studies of another means for providing turbulence and for mixing enhancement in a scramjet-type flow field. In this study, an oscillating shock was studied as the driver for mixing enhancement. The interaction of an oscillating shock with a mixing zone could provide mixing augmentation through the transfer of fluctuation energy from the mean flow to the mixing zone.<sup>4,15</sup> This

mixing augmentation could be improved by "tuning" the oscillating shock frequency to the frequency of the large-scale turbulence in the flow field. Bushnell<sup>4</sup> suggested estimating the large-scale structure frequency from:

$$f_{struct} = \frac{0.7 U_e}{\delta} \quad [1.1]$$

This eddy frequency could then be used as the "target" frequency for the "tuning" process. This paper also suggested several means for producing an oscillating shock disturbance in the flow field.

Based on the limited studies available, it was decided that oscillating shock impingement provided a good chance for augmentation of gas jet mixing in supersonic flow. A simple, passive means of generating such an oscillating shock is the introduction of a nominally steady liquid jet into the flow field. The behavior of a liquid jet in a supersonic crossflow has been studied extensively. Less and Schetz<sup>16</sup> describe the process of liquid injection into a supersonic crossflow. As the liquid penetrates the crossflow, waves develop along the surface of the jet column and propagate along the liquid plume with increasing amplitude and speed. The plume curves downstream due to aerodynamic drag and eventually fractures, shedding slumps of the liquid injectant. Wave growth and fracture contribute to the unsteadiness observed in high-speed photographic studies of liquid injection. In this study, they were concerned primarily with liquid jet breakup, fracture frequency, clump dispersal, and jet column wave frequency. The jet column



wave frequencies were initially related to a modified Strouhal number for vortex shedding past a rigid cylinder as:

$$N_w = \frac{0.4 U}{d_j} \quad [1.2]$$

This equation did not account for variations in liquid injectant properties so a modified equation was developed:

$$N_w = 0.0000325 \sqrt{\left(\frac{\sigma \times P_{tot}}{\mu_l \times \rho_l}\right) \times \frac{U_2}{d_j} \times U_j^{0.2}} \quad [1.3]$$

In both equations, the frequency of the jet column waves was seen to vary as the inverse of the liquid injector diameter. The curved bow shock present during injection into a supersonic crossflow is affected by the unsteady nature of the jet and oscillates as well. No measurements of the frequency of shock oscillation were made; however, a close relationship between wave frequency and shock oscillation frequency was presumed. Such a curved oscillating shock also produces vorticity, another potentially influential mechanism in the mixing process.

The purpose of these experiments was to document any changes in mixing performance which would result from oscillating shock impingement "tuned" to the large-scale turbulence in a mixing flow field. A previously documented injection configuration was selected as the baseline for these studies. Helium injection was used to simulate hydrogen injection for safety reasons. Water was selected as the liquid injectant because

of its ease of handling and ready availability in the laboratory. In addition to NASP, there are other applications for mixing augmentation in supersonic flow such as thrust vector control and vehicle control with transverse jets.

## 2. DESCRIPTION OF THE EXPERIMENT

### 2.1 General Description

Tests were conducted in a supersonic wind tunnel with free-stream conditions:

$$M_{\infty} = 3$$

$$P_{\infty} = 6.5 \text{ atm}$$

$$T_{\infty} = 290 \text{ K}$$

$$Re = 51 \times 10^6 / \text{m}$$

These conditions are similar to those of an airbreathing hypersonic-cruise flight vehicle operating at a Mach number of 9.0 at 58 km altitude. An inlet diffusion ratio of 3 has been assumed. In a cold-flow tunnel, such as the one used here, it was not possible to simulate the 5000 K total temperature in the vehicle combustor. These experiments are useful, however, to establish trends and relative magnitudes for mixing and penetration, and to assess the influence of different parameters on the flow field.

The baseline injector for these tests was the 15° downstream-angled, underexpanded, sonic, helium jet studied by Mays.<sup>11</sup> Mays selected this configuration as the best of the four he studied based on a compromise of costs and benefits. This injector exhibited good concentration decay, relatively low total pressure loss, and the fastest approach to concentration values equivalent to a stoichiometric hydrogen-air mixture with axial distance downstream of the jet. The jet was mounted flush with the wind tunnel floor and operated at a total temperature of 295 K and a total pressure of 3.7 atm.

Two separate sets of experiments were conducted for this investigation. In the first experiments, the effects of shock impingement location and  $\bar{q}$  were studied. Water was injected through a circular injector at  $\bar{q} = 2$  and  $\bar{q} = 6$  and the plate was positioned to cause the oscillating shocks to impinge at three different locations on the test plate. Shock impingement locations were selected downstream of the helium nozzle, on the leading edge of the helium injector, and upstream of the injector. The two  $\bar{q}$  values and different injection locations were selected as bounds to begin the process of "tuning" the shock oscillation frequency to the large-scale turbulence in the flow field. Shocks of different strength and frequency were generated by injecting at  $\bar{q} = 2$  and  $\bar{q} = 6$ . Initial studies indicated the most effective combination was  $\bar{q} = 6$  with the shock impingement downstream of the helium injector.

The remaining tests were conducted on this baseline configuration with three different diameter water injectors and  $\bar{q} = 6$ . No direct measurements of shock oscillation frequency were available from the earlier work by Less and Schetz<sup>16</sup>, so for this study, a direct connection was assumed between the jet column wave frequency and the shock oscillation frequency. Equation [1.3] was then used to three water injector diameters which would produce oscillating shocks over a range of frequencies<sup>17</sup> which bracketed the large-scale structure frequency predicted by Equation[1.1]. Selecting three injector diameters allowed further refinement of the "tuning" process. The shock frequency increased, for fixed  $\bar{q}$ , as the water injector diameter decreased. The injection flow field was documented for all four cases. Test conditions are summarized in Table 1.

Short exposure time nanoshadowgraphs were made of the four flow fields from upstream of the water injector to approximately 100 jet diameters downstream of the helium injector. The very short exposure time allowed "freezing" of the rapidly changing flow field and showed details of the large-scale eddies including size, shape and inter-eddy spacing.

High frequency response pressure transducers were used to determine the shock oscillation frequencies for three different water injectors. Additionally, simultaneous pressure transducer and hot-wire measurements were conducted to determine what relationship existed between the shock oscillation frequency and changes in the helium injection flow field. At an axial location 90 helium jet diameters downstream of the injector, measurements were made with parallel sensor hot-wire arrays to detect the presence of large-scale structures in the flow field and to determine the relative angles of the large-scale structures.

At axial locations 20, 40 and 90 helium jet diameters downstream of the jet, helium concentration, Pitot pressure, cone-static pressure, and total temperature were measured in continuous vertical profiles. Measurements were made on the jet centerline and at four lateral stations on each side of the centerline. Spacing between these lateral stations was one jet diameter. Calculations from these measurements provided helium concentration, Mach number, local speed of sound, static temperature, static pressure, density, flow speed, mass flux, total temperature and total pressure.

With this plan, it was possible to determine both the gross effects of oscillating shock impingement flow field features such as mean concentration decay and some of the details of the complex process involved.

## 2.2 Facilities and Equipment

### 2.2.1 *The Wind Tunnel*

The present experiments were conducted in the Virginia Tech 23 cm x 23 cm Supersonic Wind Tunnel shown in Fig. 2. The tunnel is a blowdown facility which exhausts to the atmosphere. It can be operated at Mach numbers from 2.4 to 4.0 and at total pressures up to 20 atm. The compressed air supply for the tunnel is provided by an Ingersoll-Rand, type HHE, four stage, water-cooled compressor. The air is dried and prefiltered to remove moisture and oil. Dust and dirt particles are removed by an afterfilter system. The air is then stored in two large steel tanks with a combined volume of 23 m<sup>3</sup>. During a tunnel run, the air from the tanks is released to the tunnel settling chamber by a computer-controlled pneumatic butterfly valve. A hydraulic valve controlled by a feedback servo-control circuit sets and holds chamber pressure. Valve position is determined by a control signal from the tunnel control computer and a settling chamber total pressure signal from a pressure transducer. This system maintains tunnel total pressure to within four percent during a typical run.

A transition cone and set of five screens in the settling chamber reduce flow angularity and turbulence. Next, air enters a two-dimensional, converging-diverging, Mach 3.0 nozzle. For these experiments, the bottom half of the nozzle was replaced by a flat plate insert as shown in Fig. 3. The nozzle has a throat area of 61.5 cm<sup>2</sup> and is designed to compensate for boundary layer growth. The flow then enters the test section which contains the models and instrumentation.

The test section is an 11.5 cm high x 23 cm wide constant area duct of rectangular cross-section. Both sides of the test section have large access doors with glass windows. These doors provide easy access to the test section and allow photography of the models and flow field. The air flow is then diffused and exhausted to the atmosphere through a muffler.

### 2.2.2 Helium Injector Model

The baseline model was designed to inject helium into a flat plate flow at a downstream angle of  $15^\circ$  relative to the horizontal. A gas supply system provided compressed helium to a plenum chamber with an internal volume of approximately 4930  $\text{cm}^3$ . The gas was injected into the Mach 3.0 flow through a sonic nozzle with a conical converging inlet. The half-angle of the converging section was  $14^\circ$ . This injector had a 0.318 cm throat diameter and was of constant cross-sectional area for one throat diameter. The injector was mounted flush with the tunnel floor in a nozzle block which covered the top of the plenum chamber. A right-hand coordinate system was fixed with the origin at the leading edge of the jet and positive-x in the streamwise direction. Figure 4 shows the design of the injector and the orientation of the coordinate system.

A test plate was mounted on the downstream side of the plenum chamber. This plate was flush with the top surface of the plenum chamber and extended approximately 100 jet diameters downstream of the helium injector as shown in Fig. 5. Slots in the plate allowed both lateral and vertical probe movement. The slots were located 45, 65 and 115 jet diameters downstream of the helium jet. Probe tips were designed to extend 25 diameters upstream of the slots, thus allowing measurements at axial stations 20, 40



and 90 throat diameters downstream of the jet. The slots provided room for probe placement up to 12 diameters off the jet centerline. When in use, the slots were covered with a flat plate which restricted the probe to vertical movement only. When not in use, the slots were plugged with brass inserts and sealed with vacuum grease.

### *2.2.3 Water Injector Model*

Water was injected into the tunnel to cause the oscillating shocks in the mixing flow field. This injectant was chosen because it was readily available in the laboratory and was easily handled. The water was injected through a flat plate model with a sharp leading edge, Fig. 6. The plate was made of brass and measured 22 cm wide x 48 cm long and was 0.65 cm thick. The plate had a leading edge angle of  $20^\circ$ . Fences 1.9 cm high mounted to the sides of the plate and covered with foam rubber were used to seal the plate against the test section doors and prevent spillage from the top of the plate into the test section. Struts installed through the upper wall of the test section held the plate in place and allowed vertical movement of the plate to control the oscillating shock impingement location. Additionally, nine mounting holes for each strut were drilled into the flat plate on 1.27 cm centers. These holes provided for plate movement in the streamwise direction to further refine the shock impingement location. The plate installation is shown schematically in Fig. 3.

The water injector orifice was located on the plate centerline 8.9 cm downstream of the plate leading edge. Three circular injectors, with orifice diameters of 0.040 cm, 0.079 cm and 0.159 cm were used. The discharge coefficient of the injectors was approximately 0.9. Each injector had a 1.3 cm straight run. All were made of brass and

were interchangeable from above the flat plate. A 3.24 cm I.D. plenum chamber was fitted to the flat plate above the injector and sealed with a rubber O-ring. The size of the plenum chamber compared to the size of the injector reduced any disturbances in the water injectant. Water was supplied to the plenum chamber by two 0.635 cm O.D. copper tubes. Injection through a flat plate was chosen over injection through the test section walls to allow for movement of the injector and to reduce the effect of wall boundary layer thickness on the water jet.

#### *2.2.4 Helium Supply System*

Compressed helium was supplied from a bank of twelve commercial helium bottles feeding into a common manifold. Manifold pressure was reduced from a range of 34 to 170 atm to 20 atm by a Grove RBX 204-015 dome pressure regulator. Reference pressure for the dome regulator was provided by a regulated commercial air bottle. The output pressure was monitored on an oil-filled pressure gage. Helium flow was controlled by a Nupro SS-6PCT pneumatic valve which was triggered by pressurized air from an Asco electric-powered, solenoid valve. Signals from the tunnel control computer were used to start and stop helium flow to the plenum chamber. A manual shut-off valve was connected in series with the pneumatic valve as a safety precaution, so that the helium flow could be stopped if the pneumatic valve failed. Following the shut-off valve, the helium moved through 1.27 cm O.D. copper tubing to a needle valve for final pressure reduction and fine tuning. The helium was then fed into the bottom of the plenum chamber through two 1.27 cm O.D. copper tubes. This system maintained jet total pressure to within four percent of the desired value.

### 2.2.5 Water Supply System

A diagram of the water injection system is shown in Fig. 7. The water reservoir was a stainless steel tank with a volume of 3000 ml. Driving pressure for the injectant tank was provided by a pair of regulated commercial air bottles. Tank pressure was monitored on a Heise CMM-4386 pressure gage. The size of the tank played an important role in maintaining a constant injection pressure in the plenum chamber during each run because the volume of water injected during each run was small compared to the total volume of water stored in the tank. The volumetric flow rate for each injector was determined to provide  $\bar{q} = 6$  for the given tunnel free-stream conditions. The injectors were tested at different reservoir pressures until the desired flow rates were achieved. The reservoir pressure was monitored during each run to ensure the desired pressure was maintained.

As in the helium supply system, water to the plenum chamber was controlled by a computer-operated pneumatic valve connected in series with a manual safety valve. The tunnel control computer signal used to start the helium was also used to start the water flow. In the water system, the signal to the Asco electric-powered solenoid was delayed by a variable-delay relay. Once the delay, nominally three seconds for these experiments, expired, the solenoid triggered a Whitey Model SS-43X54-151-DA pneumatic valve which started water flow to the plenum chamber. The water then passed through a Nupro B6-TF-140 filter which was capable of removing foreign particles larger than 140 microns from the water. High-pressure 0.953 cm diameter plastic tubing was

used to pipe the water from the filter to the plenum chamber feed lines. All other tubing in this system was 0.635 cm diameter copper.

### *2.2.6 Traversing System*

Probes used during the experiments were raised and lowered with a computer controlled traversing system. The traverse assembly was equipped with a Trans-Tek Series 240 Linear Voltage Displacement Transducer (LVDT) powered by a Computer Devices Model 340-9200A Stepper Motor. The motor rotated a geared wheel which moved a slotted rod 0.013 cm per step. Attached to the rod was a probe mounting bracket which could slide laterally on two tightening screws. The entire assembly was secured to a mounting stand beneath the tunnel test section. Probes were mounted through slots in the test plate into a 0.635 cm hole in a collar which was then tightened on the probe stem. Once the probe was aligned at the desired measurement location, all screws were tightened and the probe could only move vertically.

The stepper motor was controlled by an American Precision Industries DMA-64 Stepper Motor Controller driven by a UAI 3701 Command Processor Board which communicated with the tunnel control computer through a standard RS-232C serial communications port. The wind tunnel user specified stepper motor speed, traversing distance and direction required for the measurements being conducted.

## **2.3 Instrumentation**

### *2.3.1 Tunnel Control Computer*

An IBM PC with an installed MetraByte DAS-16F, High Speed Analog to Digital (A/D) conversion board was used as the tunnel control computer. One of the digital-to-analog (D/A) output channels on the DAS-16F was used in the wind tunnel valve servo-control circuit to provide a "set point" control voltage and to activate a relay which opened the pneumatic butterfly valve on the wind tunnel. Another D/A channel was used for two purposes. When the wind tunnel valve opened, a 3.0 volt signal was sent which activated the helium supply system and the water supply timer as described in Sections 2.2.4 and 2.2.5. After allowing a suitable time delay for the tunnel starting transients to dampen, a 5.0 volt signal was sent to trigger the data acquisition system being used for a given experiment. At the end of a run, the signal was returned to zero, causing the helium system to shut down.

### *2.3.2 Data Acquisition Systems*

Most of the data taken during the wind tunnel runs was acquired with a MetraByte DAS-20, 12 bit, High Speed A/D conversion board installed in a Zenith Z-248 AT class computer. The data acquisition board had 20 twelve-bit data channels giving a resolution of 0.0024 volts for a zero to ten volt analog signal. Signals from thermocouple probes used in these tests were processed through a MetraByte EXP-20 Multiplexer/Amplifier which conditioned and amplified the millivolt level thermocouple outputs to a level readable by the DAS-20. The EXP-20 was wired in series with a MetraByte STA-20 Screw Terminal Adapter which received the voltage signals not requiring amplification

before being read by the DAS-20. The two units were then connected to the DAS-20 where the signals were collected and processed by the LabTech Notebook data acquisition software package. LabTech Notebook was used to sample and collect the voltage signals and convert them into readable ASCII data before storing the data on a fixed disk drive installed in the computer. In the case of pressure, temperature and position data, when proper calibrations were provided, Notebook converted and stored the data in engineering units. This A/D system was used for all concentration and mean flow data collection runs.

Data collection for the shock frequency measurements, the large-scale structure measurements, and the combined hot-wire/Kulite measurements required faster sampling rates than were available from the DAS-20 system just described. For these measurements, a LeCroy 6810 Waveform Recorder operated by the Waveform Catalyst software package was used with the software installed on the same Zenith computer. This combination allowed for sampling rates as high as 5,000,000 samples per second on a single channel or 2,000,000 samples per second on 2 channels. As with the DAS-20 system, data acquisition was started with a 5.0 volt signal from the tunnel control computer. All channels were sampled simultaneously with the data initially stored in buffers on the LeCroy then transferred to the Zenith computer for display by the Catalyst software. This allowed visual confirmation that the data was acceptable before continuing to the next wind tunnel run. This system was a 12-bit system giving a resolution of 0.001 mV on a zero to four volt signal.

### 2.3.3 Stagnation Properties

Wind tunnel stagnation pressure was measured with a Pitot tube installed in the tunnel settling chamber. The probe was connected to a 0 to 20.4 atm National Semiconductor pressure transducer. The transducer was powered by a  $\pm 12$  volt power supply. Output from the transducer was filtered and amplified before being read by the DAS-16F A/D system for use in the wind tunnel servo-control circuit. The signal was also sent to the DAS-20 for processing and storage for later use. In addition, the signal was sent to a Hewlett-Packard 17501A strip chart recorder mounted in the tunnel control console. The line graph displayed on the recorder was monitored by the tunnel operator to verify that the system was controlling properly at the desired operating pressure.

Omega Type-K Thermocouples with 0.13 mm beads were used to measure tunnel total temperature and helium plenum chamber total temperature. The thermocouples were connected to the EXP-20 with its built-in cold junction compensation circuit and amplifier and were then sampled and stored by the DAS-20.

Helium jet total pressure was measured with a Pitot tube in the plenum chamber. A Statham 0 to 6.8 atm pressure transducer converted the pressure information into a voltage signal which was amplified by an Ectron Differential D.C. Amplifier Model 562 and low-pass filtered by a four pole Bessel filter with a cut-off frequency of 340 Hz. Excitation voltage for the transducer was provided by an Ectron Model 516-5SG Excitation Power Supply. The filtered signal was sampled and stored by the DAS-20 A/D system. The total pressure was also visually monitored using a Heise C-53332 Analog Pressure Gage.

#### 2.3.4 *Optical System*

The nanoshadowgraph system used for these experiments is shown in Fig. 8. A Xenon Novatron 739-B Nanopulse Lamp powered by a Xenon Model 4237A Nanopulser provided the light source. This manually triggered lamp provided a 30 nanosecond light pulse. The short duration light pulse made it possible to examine phenomena that occurred too rapidly for longer exposure time systems to clearly record, such as features of the large-scale eddies in the flow field. This also provided a single exposure of the eddy movement. The light was reflected through the wind tunnel test section by a parabolic mirror with a 1.8 m focal length. The resulting image was recorded by a modified Burke and James View Camera equipped with a Polaroid Model 545 film holder. Polaroid Type 57 High Speed Instant Film recorded the image. Through trial and error, it was found that the nanoshadowgraph picture was most sharply focused when the plane of the film was 33 cm from the test section window.

#### 2.3.5 *The Helium Concentration Probe*

An aspirating, hot-film, concentration probe based on the original design of Ng, Kwok and Ninneman<sup>19</sup> was used to measure continuous, vertical, helium concentration profiles at each axial and lateral station. The probe is illustrated in Figs. 9 and 10. A continuous stream of the gas to be analyzed entered the probe diffuser tip through a 0.33 mm diameter orifice. After the inlet, there was an internal divergence to a circular cross-section duct of 3.86 mm diameter. The gas then passes over the sensor and exits via a 0.63 mm diameter hole located behind the sensor. By applying a vacuum behind this exit hole, the orifice can be choked, thus fixing the Mach number at the sensor. The probe



was designed to swallow its bow shock into the diffuser tip so that the zone of silence extended into the probe tip. This insured that no mass flow spillage occurred and exposed the hot-film sensor to the same gas composition which would be found at the measurement point if the flow were undisturbed by the probe. Because of the large expansion ratio in the probe, the velocity at the sensor was on the order of 1 m/s. A 10<sup>5</sup> cm<sup>3</sup> volume pressure vessel evacuated by a Duo Seal Model 1405 pump provided the vacuum to operate the probe. A more detailed description of the probe and its operation can be found in Ref. 19.

The sensor in this probe was a TSI Model 1210-20 General Purpose Cylindrical Hot Film Sensor. The 1210-20 consists of a platinum hot-film mounted on a cylindrical quartz substrate. The hot-film was 0.051 mm in diameter and had an active sensor length of 1.00 mm. A Dantec DISA Model 55M10 Standard CTA Bridge connected to a Dantec DISA Model 55M01 Main Unit drove the hot-film sensor. The bridge output signal was low-pass filtered by a Frequency Devices Model 9002 Dual-Channel Programmable Filter. The filter was set to a cut-off frequency of 50 Hz to prevent any 60 Hz electrical noise from being included with the signal. The DAS-20 A/D system read and recorded the voltage output from the filter.

Total temperature and pressure measurements were made in the probe at the sensor measurement location. An Omega Type-K thermocouple, with a 0.13 mm bead was mounted through the probe wall to provide the sample temperature at the sensor. A static pressure port was drilled through the probe wall and connected to a Statham 0 to 3.4 atm pressure transducer. Since the Mach number was very low, the static pressure was

assumed equal to the total pressure in the measurement chamber. With these sensors in place, one wind tunnel run provided the hot-film voltage, total temperature and total pressure required to determine the helium concentration of the sample.

### 2.3.6 *Other Mean Flow Probes*

Continuous vertical profiles of total pressure were made using the Pitot probe illustrated in Fig. 11. This probe was made from a section of stainless steel tubing with a 0.635 cm O.D. and a 0.386 cm I.D. The tube had a conical brass inlet cap with an orifice diameter of 0.65 mm giving it a capture area of 0.0032 cm<sup>2</sup>. A 1.6 mm tube was soldered into the exit end of the probe and connected by flexible tubing to a Statham 0 to 3.4 atm pressure transducer which converted the pressure to a voltage signal. The signal was amplified by the Ectron amplifier and filtered by the 340 Hz cut-off frequency Bessel filter before being sampled and stored by the DAS-20 A/D system. The time response of the probe was approximately 0.015 seconds.<sup>11</sup>

The total temperature probe was based on the classic design of Ref. 20 and is shown in Fig. 12. A section of 0.32 cm diameter stainless steel tubing was used as the probe housing. A conical, Lexan cap was fixed to the flow end of the tubing to reduce heat loss by radiation. At the tip of the cap, there was a 1.6 mm diameter orifice which allowed the flow to enter and stagnate inside the cap. The inlet orifice expanded to a 0.38 cm diameter chamber which contained an Omega Type-K Thermocouple with a bead diameter of 0.38 mm. The thermocouple was epoxied so that it extended approximately 4.0 mm from the stainless steel housing. Two vent holes of 0.34 mm diameter were placed just aft of the thermocouple bead. The thermocouple was connected through the

EXP-20 to the DAS-20 A/D system. This probe had a recovery factor of approximately 98 percent.

The cone-static probe, illustrated in Fig. 13, consisted of a 10° half-angle brass cone soldered to a 1.6 mm diameter stainless steel tube. The cone had four 0.33 mm diameter pressure taps located 2.7 cm from its vertex. The pressure taps were spaced 90° apart around the cone circumference. These taps emptied into a common chamber to reduce error due to flow angularity. The probe was soldered into a 0.64 cm stainless steel sleeve to prevent excessive probe deflection during tests. The probe had a capture area of 0.0034 cm<sup>2</sup> and a time response of 0.08 seconds.<sup>11</sup> Cone static pressure was read by an MB Electronics 0 to 0.68 atm pressure transducer which converted the pressure to a voltage readable by the DAS-20 A/D system.

### *2.3.7 Position Measurement*

Lateral probe position was fixed by a scale etched on the surface of the test plate in front of each slot. The scale had 13 lines, one at the helium jet centerline, and 6 to each side of the jet centerline. Interline spacing was equal to one jet throat diameter. The slot cover plate (Section 2.2.2) had a similar mark aligned with the probe centerline. To place the probe at a lateral station, the cover mark was matched to the appropriate mark on the test plate.

Vertical position was measured using the Trans-Tek LVDT described in Section 2.2.6. The transducer housing was fixed to part of the traverse which did not move relative to the wind tunnel. The core was fixed to the traverse rack and moved with the

probe. The LVDT could measure probe displacements up to 15 cm at an accuracy of 0.5 percent.

### *2.3.8 Kulite Pressure Transducer*

A Kulite XT-190-150D differential, piezo-electric pressure transducer was used for shock frequency measurements and shock/boundary layer fluctuation coherence tests. The transducer was mounted flush with the tunnel floor in the nozzle block 2.80 cm downstream of the injector leading edge. The reference side of the differential transducer was opened to the atmosphere. The sensor had a 0.386 cm sensor area covered by an M-screen to protect the sensor from particle damage. Excitation power for the Kulite was provided from the Ectron as was amplification for the output signal. The signal was low-pass filtered through a Thermo Systems Inc. IFA100 signal conditioner with a cut-off frequency of 200 KHz. The signal from the IFA was sampled at 500,000 samples per second by the LeCroy 6810 and stored on the Zenith PC with the Waveform Catalyst software.

### *2.3.9 Hot-Wire Probes*

Two types of hot-wire probes were used in these experiments. In the shock correlation experiments, a single wire probe using DANTEC Model 55P11 wires was used. The probe was connected through a DANTEC 55M12 Bridge to a DANTEC 55M01 Anemometer Main Unit. For these tests, the output of the anemometer was low-pass filtered at a 200 KHz cut-off frequency by the IFA 100 and sampled at 500,000 samples per second by the Waveform Catalyst/LeCroy 6810 system.

For the eddy structure angle experiments, a parallel wire probe using DANTEC Model 55P71 sensors was used. These wires, of 1.5 mm separation, were connected through identical 55M12 Bridges to 55M01 Anemometer Main Units as used in the correlation experiments. The IFA 100 was used as an anti-aliasing filter with a cut-off frequency of 500 KHz and the signals were sampled at 2,000,000 samples per second by the Catalyst/LeCroy system.

## 2.4 Experimental Methods

### 2.4.1 Calibrations

Electronic pressure transducers were used to measure settling chamber pressure, helium plenum chamber pressure, Pitot pressure, cone static pressure and the pressure in the concentration probe at the hot-film sensor. These transducers were calibrated using known pressures and measuring the voltage output from the transducer. During the calibration, the voltage was measured after it had been amplified and filtered, just as it would be during an actual data collection run. A linear, least-squares program was used to calculate the coefficients for an equation relating the known pressure to the transducer voltage. The coefficients for this fit were then input to LabTech Notebook so that pressure data measured during a tunnel run could be output and stored as pressure rather than voltage. Pressures above ambient were provided by a commercial air bottle and an Ametek MK100 pneumatic pressure tester which was attached to the transducer being calibrated. This pressure tester provided a range of pressures from 1 to 7 atm in 0.7 atm increments accurate to 0.017 atm. For calibrations below ambient, the pressure transducer and a 0 to 2.4 atm Heise gage were connected to a pressure vessel. The pressure vessel was connected to a vacuum pump through an on/off valve which, when opened, allowed air to bleed out of the vessel, lowering the pressure. Pressure was read from the Heise gage and voltage was sampled through the DAS-20 A/D system. The curve fit was also completed here and the coefficients input to LabTech Notebook for use in converting the pressure transducer voltage to engineering units.

Thermocouples require no calibration; however, the cold junction compensation (CJC) circuit on the EXP-20 requires periodic calibration. Calibration is accomplished by measuring the temperature at the CJC with a handheld digital thermometer while reading the CJC output voltage with a digital volt meter. The CJC calibration potentiometer is then adjusted until the volt meter reads a voltage corresponding to the measured temperature multiplied by 24.4 Mv/°C. No further adjustments are required for temperature measurement.

Concentration probe hot-film voltage is related to Reynolds number through the following equation:

$$V^2 = \frac{(R_s + R_w)^2}{R_w} \pi l k (a Re^m + b) (T_w - T_f) \quad [2.1]$$

$R_s$ ,  $R_w$ ,  $l$  and  $T_w$  were known,  $k$  was a function of the gas composition, and  $T_f$  was measured with the thermocouple located at the sensor location.<sup>19</sup> Constants  $a$ ,  $b$  and  $m$  were determined by the following calibration procedure.

An 11,500 cm<sup>3</sup> pressure vessel was filled with a known concentration of helium at 3 atm. Helium concentration was determined from the partial pressures of the helium and air in the vessel. A pressure gage was used to monitor the pressure in the vessel. One end of a 0.63 cm I.D. rubber hose was connected to a valve located on the pressure vessel and the other end to the probe inlet. Vacuum was applied to the probe and the valve on the pressure vessel was opened so that the gas mixture was drawn into the probe. Measurements of  $P_1$ ,  $T_1$ , and hot-film voltage were taken at vessel pressures from

2.4 atm to as low as 0.75 atm and at several helium concentrations. Since total temperature variation in the wind tunnel was small, all calibrations were done at the ambient temperature. A computer program was used to fit a logarithmic curve to the data for each helium concentration. Figure 14 shows a typical set of calibration curves and calibration data.

Calibration of the LVDT took place after each change of probe or probe location. Once a probe was installed and fully connected, a PTI, model 2210, cathetometer was used to measure probe location within 0.001 cm. A 1.3 cm square block was used as a reference height for determining the cathetometer reading corresponding to the surface of the test plate. Cathetometer readings were taken at each of four probe tip locations while corresponding voltages were read with the DAS-20 A/D system. The floor reading was subtracted from each measurement to determine the actual probe height above the wind tunnel test plate. A least-squares fit was performed on the resulting voltage, displacement data pairs to determine the coefficients for a linear equation relating voltage and displacement values. These coefficients were also input to LabTech Notebook where they were used to convert LVDT voltage to actual probe displacement during each wind tunnel run.

The discharge coefficient for a nozzle is an indication of viscous losses in the nozzle flow. It is defined as:

$$D = \frac{\dot{m}_{actual}}{\dot{m}_{ideal}} \quad [2.2]$$



The denominator was determined from measured total temperature and total pressure, in the helium plenum chamber, using isentropic relations and the mass flow equation. The actual mass flow was determined during a series of wind tunnel runs by reading the volumetric flow rate of helium on a Brooks Instrument Division Model 1307D08E1A1A rotameter installed in the helium supply line just before the plenum chamber. The rotameter reading was corrected for non-standard conditions using the measured gas supply temperature and pressure. The discharge coefficient for this helium injector was found to be 0.93.

#### *2.4.2 Data Acquisition Procedure*

The data acquisition procedure can best be described by giving an example of a typical wind tunnel run. Before each run, all equipment and connections were checked to ensure everything was functioning. The compressor was then allowed to pump the storage tanks to the desired holding pressure, approximately 19 atm. The appropriate data acquisition program, either LabTech Notebook or Waveform Catalyst, was initialized as was the FORTRAN program used for tunnel control.

When the air supply reached the desired pressure, the tunnel control PC initiated the run. After a user-selected delay, usually 5 seconds, the butterfly valve was opened, releasing compressed air into the tunnel. Valve opening was designated  $t = 0$  as a convenient reference point. At the same time, the helium supply was turned on to allow time for the plenum chamber pressure to reach the desired value before any data was collected. At  $t = 3$  seconds, the water injection was turned on. At  $t = 7$  seconds, signals were sent to begin upward movement of the traverse and to trigger data

acquisition in LabTech Notebook or Waveform Catalyst. The delays allowed all flow transients to dampen out before data collection began. Shadowgraphs were taken anytime after the first 7 seconds had passed.

The Zenith PC sampled data for 6 to 8 seconds and only on the upward traverse. When the probe reached the top of its traverse, the helium and water were shut off, the probe was brought down in approximately one second and the tunnel was shut down one second later. The total run time, from valve opening to valve closing, was approximately 18 seconds. Because of the blow-down nature of the wind tunnel, longer runs were not possible at the 6.5 atm free-stream pressure level.

The data acquisition program wrote the resulting data to the hard disk for later reduction and analysis. Both LabTech Notebook and Waveform Catalyst provided near real-time on-screen plots of selected data parameters. This allowed the operator a chance to check for problems before continuing to the next data collection run. If no incongruities were found in the data, the probe and/or camera were repositioned for another run.

#### *2.4.3 Concentration Reduction*

A FORTRAN program was written to determine helium concentration profiles from files of hot-film voltage, pressure, temperature and probe position. The program used data from vertical profiles taken with the concentration probe along with a calibration file which contained the calibration constants and parameters describing the hot-film used in the concentration probe. At each probe location, the reduction program used the values of  $P_1$  and  $T_1$  in equation [2.1] to calculate lower and upper bounds on the

voltage between two known concentrations. If the measured voltage did not fall within the calculated bounds, the program stepped up in concentration levels until the proper concentration boundaries were determined. Once the boundary concentrations were determined, the reduction program interpolated between them to calculate the experimental value of the helium mole fraction,  $\chi_{He}$ . The resulting mole fractions were converted to mass fractions using:

$$\alpha_{He} = \chi_{He} \times \frac{MW_{He}}{MW_{mix}} \quad [2.3]$$

#### 2.4.4 Mean Flow Reduction

The helium concentration, determined as described in Section 2.4.3, was combined with cone-static pressure, Pitot pressure, and total temperature profiles to calculate profiles of Mach number, mass flux, static temperature, static pressure, density and total pressure. The FORTRAN program used to calculate the profiles assumed the flow could be treated as an adiabatic flow of a calorically perfect gas. Values for the gas constant,  $R$ , and the ratio of specific heats,  $\gamma$ , were also determined in the data reduction program. These values were used, where appropriate, in the equations which follow. Since the total pressure, total temperature and cone-static pressure were not measured during the same run as the hot-film voltage, it was first necessary to align these profiles with the concentration profiles. This was done with a FORTRAN interpolation program. Once all profiles were aligned, the mean flow reduction began. Mach number was

calculated using the cone-flow and Rayleigh-Pitot equations. The cone-flow equation relates Mach number to the pressure on the surface of a cone by:

$$\frac{P_c}{P_1} = 1 + \frac{\gamma M_1^2 (P_c - P_1)}{2 q_1} \quad [2.4]$$

The dependence on static pressure can be eliminated by combining equation [2.4] with the Rayleigh-Pitot equation:

$$\frac{P_1}{P_2} = \frac{\left(\frac{2}{\gamma+1} M_1^2 - \frac{\gamma-1}{\gamma+1}\right)^{\frac{1}{\gamma-1}}}{\left(\frac{\gamma+1}{2} M_1^2\right)^{\frac{\gamma}{\gamma-1}}} \quad [2.5]$$

Since the last term in equation [2.4] is a function of  $M_1$ , and  $\gamma$  for a given cone, multiplying Equation [2.4] and [2.5] results in:

$$\frac{P_c}{P_2} = f(M_1, \gamma) \quad [2.6]$$

This relationship was used to generate a table of Mach number as a function of  $\gamma$  and  $P_c/P_2$  for the 10° half-angle cone. At sufficiently low Mach numbers, around  $M = 1.1$ , the cone shock detaches rendering the above equations invalid. In the data reduction program, this was indicated by a value of  $P_c/P_2$  greater than a critical value,  $(P_c/P_2)_{crit}$ .

The program calculated  $(P_c/P_2)_{crit}$  for a given  $\gamma$  by interpolating in the Mach number table.

For pressure ratios less than the critical value, the Mach number was determined by interpolating over  $\gamma$  and  $P_c/P_2$  in the previously generated Mach number table. The static pressure was then determined from Equation [2.5].

In cases where the pressure ratio was greater than the critical value, the program interpolated for  $P_1$  from values which surrounded the unknown point. The program then compared  $P_1/P_2$  to the value necessary for sonic flow,  $(P_1/P_2)_{crit}$ , determined from:

$$\left(\frac{P_1}{P_2}\right)_{crit} = \left(\frac{\gamma + 1}{2}\right)^{-\frac{\gamma}{\gamma - 1}} \quad [2.7]$$

If the value was less than the critical value, then the flow at that point was supersonic, and the Mach number was determined from the Rayleigh-Pitot Equation. For values greater than the critical ratio, the flow was subsonic and the Mach number was determined from isentropic relations, assuming  $P_{u1} = P_{u2}$ , as in:

$$M = \left[ \frac{2}{\gamma - 1} \left( \frac{P_1}{P_2} \right)^{\frac{1-\gamma}{\gamma}} - 1 \right]^{\frac{1}{2}} \quad [2.8]$$

With Mach number and static pressure determined, the remaining flow properties were calculated. With  $T_{e2} = T_{u1}$  across a normal shock and given the previously

determined Mach number, the static temperature was calculated by solving for it in the isentropic relations so that:

$$T_1 = \frac{T_2}{1 + \frac{\gamma - 1}{2} M_1^2} \quad [2.9]$$

The local sonic velocity, flow velocity and density were determined with the following set of equations:

$$a_1 = \sqrt{\gamma RT_1} \quad [2.10]$$

$$u_1 = M_1 a_1 \quad [2.11]$$

$$\rho_1 = \frac{P_1}{RT_1} \quad [2.12]$$

Mass flux,  $\rho_1 u_1$ , was determined by multiplying the density by the velocity at each point in the flow. Total pressure was determined from the Pitot pressure using the normal shock relation for total pressures:

$$P_{i1} = P_{i2} \left[ \frac{(\gamma - 1)M_1^2 + 2}{(\gamma + 1)M_1^2} \right]^{\frac{\gamma}{\gamma - 1}} \left[ \frac{2\gamma M_1^2 - (\gamma - 1)}{\gamma + 1} \right]^{\frac{1}{\gamma - 1}} \quad [2.13]$$

All mean flow values were then matched with corresponding probe displacements and written to computer files for further analysis.

#### 2.4.5 Eddy Structure Angle Reduction

The determination of the presence of organized structures in the flow field and corresponding structure angles required the wire separation distance, the time delay between measurements and the local velocity. Clark<sup>18</sup> described the data reduction process in detail; it is summarized here. The local velocity was determined from the concentration and mean flow data as described in Section 2.4.4. The other quantities were determined during separate hot-wire data runs. A relationship between the different quantities is shown graphically in Fig. 15. A structure passing the parallel wire probe at an angle will cause a time delay between the output of the hot-wires. From the time delay, wire separation and local velocity, the structure angle associated with average large-scale motion is calculated from:

$$\theta = \tan^{-1} \left[ \frac{w \cos \beta}{(\bar{U} * \Delta t - w \sin \beta)} \right] \quad [2.14]$$

The time delay between the two hot-wire signals was found by calculating a cross-correlation between the two signals. This gives a means of determining the dependence of one signal on the other. Here the cross-correlation was normalized by dividing by the root mean square of the two hot-wire signals. The cross-correlation is defined as:

$$S_{12} = \int_{-\infty}^{+\infty} \frac{HW_1(t)HW_2(t-\epsilon) dt}{HW_{1RMS} HW_{2RMS}} \quad [2.15]$$

This function gives a magnitude of correlation and a phase difference between the two signals. If the two systems see the same signal simultaneously, the peak value of the correlation will occur at zero time delay ( $\epsilon = 0$ ). If the signal is detected at discretely different times, the peak correlation will occur at the corresponding time shift.

The computer program described by Clark<sup>18</sup> was used to calculate both auto-correlations and cross-correlations. The auto-correlation was evaluated from:

$$S_{11} = \int_{-\infty}^{+\infty} \frac{HW_1(t)HW_1(t-\epsilon) dt}{HW_{1RMS} HW_{2RMS}} \quad [2.16]$$

This auto-correlation was integrated over time to provide an integral time scale for the flow. The integral time scale was then multiplied by the local velocity to determine a characteristic length of the turbulent structures in the flow field.

#### 2.4.6 Kulite / Hot-Wire Reduction

Raw voltage data from the Kulite pressure transducer was used to study the oscillating shock frequency for the three water injectors. The voltage data was divided into blocks of 1,024 data points and then transformed into the frequency domain using the Fast Fourier Transform (FFT) function built into LabTech Notebook. A power spectrum was also calculated for each block of data, again using LabTech Notebook, which determined the spectrum from:



$$P(db) = 10 \times \log_{10}(X_r^2 + X_i^2) \quad [2.17]$$

where  $X_r$  and  $X_i$  are the real and imaginary parts of the transformed data. Power spectra for 20 blocks of data were then averaged along each spectral line to smooth away any purely random noise present in the signals.

In attempting to determine the relationship between the shock oscillation and downstream fluctuations in the flow field, signals from the Kulite pressure transducer described previously were compared with signals from a hot-wire installed at the axial measurement station 20 helium jet diameters downstream of the jet. As with the shock frequency measurements, the Kulite and hot-wire voltage data were divided into blocks of 1,024 data points and transformed to the frequency domain using the FFT function of LabTech Notebook. Averaged one-sided auto-spectral density functions for both the Kulite and hot-wire were calculated from:

$$\bar{G}_{xx}(f_k) = \frac{2}{n_d N \Delta t} \sum_{i=1}^{n_d} |X_i(f_k)|^2 \quad [2.18]$$

for the Kulite signal and:

$$\bar{G}_{yy}(f_k) = \frac{2}{n_d N \Delta t} \sum_{i=1}^{n_d} |Y_i(f_k)|^2 \quad [2.19]$$

for the hot-wire signal, where  $\Delta t$  is the time between samples,  $n_d$  is the number of blocks of data and  $N$  is the number of samples per block. An average one-sided cross-spectral density function was determined using:

$$\bar{G}_{xy}(f_k) = \frac{2}{n_d N \Delta t} \sum_{i=1}^{n_d} [X_i^*(f_k) Y_i(f_k)] \quad [2.20]$$

These values were used to compute an ordinary coherence function along each spectral line using:

$$\hat{\gamma}_{xy}^2(f_k) = \frac{|\bar{G}_{xy}(f)|^2}{\bar{G}_{xx}(f) \bar{G}_{yy}(f)} \quad [2.21]$$

The phase shift between the two signals was determined by calculating the phase factor along each spectral line from:

$$\bar{\phi}(f) = \tan^{-1}[\bar{Q}_{xy}(f_k)/\bar{C}_{xy}(f_k)] \quad [2.22]$$

where  $\bar{C}_{xy}(f_k)$  and  $\bar{Q}_{xy}(f_k)$  were the real and imaginary parts of cross-spectrum estimate calculated from equation [2.20].

#### 2.4.7 Nondimensionalization Scheme

All probe displacements and measurements stations were nondimensionalized by the helium jet throat diameter. Where presented in nondimensional form, all other quantities were nondimensionalized using their respective free-stream values. Free-stream Mach number was found by averaging Mach number values at probe locations outside some user specified disturbance region. The calculated-free stream Mach number was then used with values of free-stream total temperature and total pressure measured in the wind tunnel settling chamber to determine the remaining free-stream properties according to the following hierarchy of equations:

$$T_{\infty} = \frac{T_{t\infty}}{1 + \frac{\gamma - 1}{2} M_{\infty}^2} \quad [2.23]$$

$$a_{\infty} = \sqrt{\gamma R T_{\infty}} \quad [2.24]$$

$$u_{\infty} = M_{\infty} a_{\infty} \quad [2.25]$$

$$P_{\infty} = \frac{P_{t\infty}}{\left(1 + \frac{\gamma - 1}{2} M_{\infty}^2\right)^{\frac{\gamma}{\gamma - 1}}} \quad [2.26]$$

where  $P_\infty$  was measured during the Pitot pressure probe runs. Free-stream density was found using the perfect gas law:

$$\rho_\infty = \frac{P_\infty}{RT_\infty} \quad [2.27]$$

Free-stream mass flux was found by multiplying the results of Equations [2.25] and [2.27]. Helium concentration was expressed as a non-dimensional mass fraction as given by Equation [2.3].

### 3. RESULTS

Composite nanoshadowgraph pictures of the injection flow field were assembled. Contour plots of helium concentration were generated for each configuration at each axial location. Plots of maximum concentration decay and core penetration were also made. Additionally, nondimensionalized contour plots of significant mean flow variables were created for all configurations and measurement stations. Power spectra were generated for Kulite pressure measurements of the oscillating shock frequencies as well as power spectra for some of the hot-wire measurements. Coherence estimates for simultaneous Kulite and hot-wire measurements were obtained and plotted for two injection configurations.

#### 3.1 Nanoshadowgraphs

Figures 16 through 19 are the composite nanoshadowgraphs for the four test cases. The Mach 3.0 free-stream runs from left to right in all photographs. The helium injection point, the axial measurement stations and the water injection location, where appropriate, are all shown on the pictures. These nanosecond ( $10^{-8}$  sec) exposure time photographs allowed recording of turbulent structures in the flow field which moved too rapidly to be photographed by other means.

Figure 16 shows the baseline,  $15^\circ$ , underexpanded, sonic helium injection flow field. Some flow field features normally expected to appear in such an injection configuration are not present in this picture. The barrel shock and separation region normally associated with underexpanded jets are not visible here. These tests had

$\delta/d \approx 1.6$ , and the non-appearance of such nearfield jet features is probably due to large density gradients in the boundary layer "washing out" the jet disturbance. Some features of the flow field are, however, clearly visible in the photograph. The water injection plate was installed during all wind tunnel runs, and in this picture the boundary layer on the plate is shown bounded by the plate to the top and a bright line indicating the flow side of the layer. Also visible is the boundary layer on the surface where the helium injector was installed. At the helium injector, the boundary layer was 1.6 helium injector throat diameters ( $d$ ) thick and grew to 2.0  $d$  by the  $x/d = 90$  axial location. The helium jet shock wave is also visible in this picture. In the boundary layer, the shock angle was  $35^\circ$ , decreasing to  $22^\circ$  in the free stream.

In this case, as Mays<sup>11</sup> also observed for his  $15^\circ$  underexpanded configuration, the helium jet has penetrated above the boundary layer by  $x/d = 20$ , creating a region of high turbulence and large eddy structures. From  $x/d = 20$  to  $x/d = 40$ , these large eddies are visible in the jet. Such large eddies are vital for significant initial entrainment of air into the mixing field. The actual outer boundary of the eddies is fuzzy or indistinct. From this figure, the approximate maximum eddy boundary height is 5.6  $d$ . The horizontal length of the eddies is on the order of 2.4  $d$ , and the streamwise distance between eddies is 5.8  $d$ . Past  $x/d = 50$ , the turbulent region becomes less distinct and by the final measurement station at  $x/d = 90$ , that region is nearly indistinguishable from the free stream. This is due to a reduction in the magnitude of the density gradient and is therefore an indicator of mixing between the jet and the free stream. There appear to

be eddies in the free-stream flow as well. It is believed that these eddies are in the boundary layer along the wind tunnel windows.

The addition of water injection to the helium injection flow field of Fig. 16 is shown in Fig. 17. In this configuration, water at  $\bar{q} = 6$  was injected through an injector of  $d_j = 0.159$  cm into the Mach 3.0 flow from the flat plate mounted to the wind tunnel ceiling. The water injector is marked near the upper left of the picture with the helium injection and axial measurement locations as shown before. Clearly visible are the water plume and the associated bow shock. Much of the upper  $\frac{1}{3}$  to  $\frac{1}{2}$  of the picture has been obscured by the water plume. The boundary layer thickness on the water injector plate was  $2.1 d_j$  at the water injector and is not visible downstream of the injector. In this configuration, as well as the other two water injection configurations, the flat plate housing the water injector has been positioned to cause the oscillating shock from the water injector to intersect the helium bow shock at a point approximately three helium jet diameters downstream of the leading edge of the helium nozzle. This position was selected as part of the process of "tuning" the oscillating shock to the large-scale turbulence in the flow field. In the free stream, the shock from the water injection measures approximately  $32^\circ$ , decreasing to about  $19^\circ$  after it intersects the helium bow shock. The helium shock is at about  $29^\circ$  between the boundary layer and the intersection with the water shock, but the angle decreases to  $22^\circ$  following the intersection.

As in Fig. 16, by  $x/d = 20$  the helium jet has penetrated the boundary layer and large eddies are visible in the flow above the boundary layer. In this instance, the eddy boundary appears more clearly defined and more clearly visible as well. Here, the

maximum eddy boundary height is  $5.9 d$ , the horizontal length is approximately  $1.7 d$  and the streamwise distance between eddies is about  $5.0 d$ . In this case, as in the baseline, by  $x/d = 90$ , the jet and mixing region are no longer as clearly defined as they were further upstream in the flow field.

Comparison of Figs. 17 and 18 reveals some of the differences which result from a change in water injector diameter. In the configuration of Fig. 18, the water was still injected at  $\bar{q} = 6$ , but the water injector diameter was reduced to  $d_i = 0.079 \text{ cm}$ . The results were a lower volumetric flow of water and a subsequent decrease in the penetration of the water plume into the free stream. Under these conditions, the upper plate boundary layer thickness was  $4.3 d_i$  at the injector and once again the boundary layer downstream of the water injector has been obscured by the water plume. The lower penetration results in a less severe disturbance to the flow and a decrease in the related water shock angle, which is further from the injector in dimensionless terms. Here in the free stream, the water shock is at  $27^\circ$ , decreasing to  $17^\circ$  following intersection with the helium bow shock. The helium shock is at nearly the same angle,  $28^\circ$ , before the intersection as in Fig. 17, and here it decreases only slightly to  $26^\circ$  following the intersection with the oscillating water shock.

The helium jet is again seen to penetrate the boundary layer by  $x/d = 20$ , however, the scale of the visible eddies is somewhat smaller and the eddies appear to be more organized than in previous figures. Here the eddy boundary is not as clearly defined as in Fig. 17, but it is still clearer than the eddy boundary of the baseline configuration shown in Fig. 16. Measurements similar to those done on the previous two



figures give an eddy boundary height of approximately  $5.1 d$ , a horizontal length of  $1.6 d$  and a streamwise separation distance of  $3.4 d$ . Once again, the turbulent region becomes less distinct downstream of  $x/d \approx 50$  until it is nearly indistinguishable from other parts of the free stream flow by  $x/d = 90$ .

The final injection configuration studied here is shown in Fig. 19. This configuration also has water injection at  $\bar{q} = 6$ ; however, the water injector diameter has been further decreased to  $d_i = 0.040$  cm. With this injector, the incoming boundary layer thickness was  $8.6 d_i$  at the water injector. As is apparent in the picture, such a small injector causes a further decrease in volumetric flow rate of water from the previous configuration. As a result, the water plume is barely visible in Fig. 19. The resulting decrease in penetration causes a weaker disturbance in the flow than the previous configuration and causes the water shock angle to decrease slightly below the  $d_i = 0.079$  cm case. Here the water shock angle is  $25^\circ$  in the free stream, and it decreases to  $16^\circ$  following intersection with the helium bow shock. The helium bow shock angle is virtually unchanged by intersecting with the water shock, changing only  $1^\circ$  as a result of the intersection of the two shocks.

As in all the previous cases, the helium jet has penetrated the boundary layer by  $x/d = 20$  and similar large eddy structures are visible in the flow downstream of that axial station. Once again, the eddy boundary is not as clearly defined as in Fig. 17, but it is still more distinct than the boundary in the baseline of Figure 16. Eddy size measurements here give a maximum boundary height of  $4.9 d$  with a horizontal length

of 1.6 d. The streamwise separation distance between eddies is 2.3 d. Once again, by  $x/d = 90$ , the eddy boundary is indistinguishable from the rest of the flow field.

It should be noted that, as previously discussed, the shocks resulting from the different water injection configurations are oscillating at different frequencies. Figures 17, 18 and 19, therefore, show "instantaneous" shock positions and water plume conditions.

### 3.2 Shock Frequency Results

Knowledge of shock oscillation frequency is important in establishing which schemes, if any, provide mixing enhancement. This series of tests was conducted in a "no helium" flow field. The Kulite pressure transducer was mounted in the cover of the helium plenum chamber approximately 9 d downstream of the leading edge of the helium injector. Using nanoshadowgraphs, the water injector plate was adjusted until the shock appeared to be striking the Kulite. The correct location was also confirmed by observing the change in Kulite output from the baseline tunnel run to runs with the water injection on.

Figure 20 shows the power spectral density plot for the no helium, no water tunnel run. As can be seen in the figure, there is a small frequency band, approximately 0 - 20 kHz, of activity which may indicate relatively low frequency pressure fluctuations in the wind tunnel boundary layer. In the rest of the plot, there is no significant energy content at any single frequency. This plot serves as a useful comparison for the water injection configurations since it represents the tunnel background noise which would be present in any run in this facility.

The graph in Fig. 21 is from the  $\bar{q} = 6$  water injection case with  $d_j = 0.159$  cm. The curve is similar in overall shape to the baseline tunnel run, but there are some readily apparent differences between the two figures. The "plateau" present from 0 to 20 kHz in the baseline run is not as readily apparent in this run. Additionally, the curve for the water injection is shifted along the entire frequency spectrum presented. The presence

of the oscillating shock and its resulting pressure fluctuations produced an increase in the Kulite output voltage monitored on the Waveform Catalyst display during the water injection run. This would explain the shift in this curve over the baseline curve. Missing from this curve, however, is any single frequency spike which would indicate the dominant shock oscillation frequency for this injector configuration.

Data acquisition errors, which were not detected at the time of these tests, resulted in the loss of data for the  $d_j = 0.079$  cm water injector. Data was correctly collected for the  $d_j = 0.040$  cm injector, however, and the power spectral density plot is presented in Fig. 22. Comparison with Figs. 20 and 21 shows that the overall power level is higher than the baseline and slightly lower on average than the power level for the largest water injector. This curve also does not follow the same shape as the data of Figs. 20 and 21. The most notable difference between the three curves is the distinct frequency spike at approximately 140 kHz. This indicates a well-defined oscillation frequency in the frequency range which Bushnell<sup>4</sup> computed should provide some mixing augmentation for this flow configuration.

### 3.3 Helium Concentration Data

Vertical concentration profiles for each axial station and each injection configuration were assembled to show a single picture of the helium concentration field at each axial station. These profiles were gridded and processed by the Surfer software package to produce contour plots of helium mass fraction or concentration. The coordinate system used by Surfer is opposite the coordinate system used in the wind tunnel; therefore, in the contour plots which follow, the helium jet should be thought of as coming out of the page.

#### 3.3.1 General Flowfield Structure

Contour plots for the baseline helium injection are shown in Figs. 23 - 25. At  $x/d = 20$ , as seen in the nanoshadowgraphs, the core of the jet has penetrated the boundary layer. This core is defined as the region in the jet which has the highest mass fraction ( $\alpha_{max}$ ). At this point, the core is about  $2.25 d$  off the floor and approximately  $+0.25 d$  off the jet centerline. The contour appears roughly symmetrical about the jet core as well. By  $x/d = 40$ , the core has moved further off the floor to  $3.9 d$  and the core of the jet has begun to elongate in the vertical direction. At this station, the core also appears to be centered at  $y/d = 0$ . There also appears to be some asymmetry in the lateral spreading of the jet. At  $x/d = 20$ , the jet was bounded by the  $y/d = -2.0$  and  $y/d = 2.0$  lines. Now, at  $x/d = 40$ , there is some lateral spreading so that the jet core is bounded by the  $y/d = -2.5$  and  $y/d = 2.0$  lines on the contour plot. By the last axial station,  $x/d = 90$ , shown in Fig. 25, more changes have taken place. The jet appears

to have bifurcated, showing two cores about  $4.4 d$  off the floor and at  $y/d = -0.25$  and  $y/d = 1.25$ . The helium also has spread more laterally, now essentially bounded by  $y/d = -2.5$  and  $y/d = 3.5$ . The jet also appears to have remained approximately symmetrical about the vertical axis of the core.

Figures 26 - 28 show the concentration contours for the first water injection case,  $d_i = 0.159$  cm. Here, the initial core penetration at  $x/d = 20$  is only  $z/d = 1.7$ . This value increases to  $z/d = 4.7$  by the final axial station. The core is initially centered above  $y/d = 0$  at  $x/d = 20$ . By the  $x/d = 40$  axial station, the core has begun to spread laterally and appears to be bifurcating, forming a second core, to the positive  $y/d$  side of the plot. This trend continues to  $x/d = 90$ , where there appears to be a second, lower concentration, core at  $z/d = 4.0$  above  $y/d = 3.0$ .

Some of the same trends are evident in the concentration contours for the  $0.079$  cm water injector shown in Figs. 29 - 31. At the  $x/d = 20$  station, the core has penetrated to  $z/d = 2.6$ , centered at  $y/d = 0$ . The contours appear roughly symmetrical about the jet vertical at this station. By  $x/d = 40$ , the main core is at  $z/d = 3.6$  and there is some vertical spreading leading to another small core at  $z/d = 1.8$ ,  $y/d = 0$ . There are also some initial indications of lateral spreading at this point. At the final measurement station, the jet has clearly split into two cores, one at  $y/d \approx 0$  and the other at  $y/d \approx -3.0$ . There has also been essentially no change in the  $z/d$  position of the core from the previous station to this one.

Contour plots for the final water injector,  $d_i = 0.040$  cm, are shown in Figs. 32 - 34. Again, the vertical movement of the core is similar to the previous cases. At

$x/d = 20$ , the core is at  $z/d = 2.3$  and the penetration increases to  $z/d \approx 3.2$  at  $x/d = 90$ . The core is at  $y/d \approx 0$  at  $x/d = 20$ , but has moved slightly to  $y/d \approx .25$  at  $x/d = 40$ . There is also evidence in Fig. 33 of lateral spreading of the core with indication of the beginnings of a second core at  $y/d = -1$ ,  $z/d = 2.5$ . The second core is also evident in Fig. 34, although it is not as clearly defined as the second core area in Fig. 31.

In all the cases just discussed, there were large gradients in helium concentration at  $x/d = 20$  for all injection configurations. The magnitude of these concentration gradients had decreased significantly by  $x/d = 90$  for all cases, indicating the presence of large amounts of mixing between the jet and the free stream in all configurations.

### 3.3.2 Helium Concentration Decay

The maximum concentrations ( $\alpha_{\max}$ ) and their locations were determined for all injection configurations and axial locations from the contour plots and are presented in Tables 2 and 3. The data in Table 2 was used to generate helium mass fraction decay curves. Since the concentration decayed exponentially, a power law curve fit of the form:

$$\alpha_{\max} = \beta_1 \left(\frac{x}{d}\right)^{-n_1} \quad [3.1]$$

was used, where  $\beta_1$  and  $n_1$  were determined from the curve fit. The exponent,  $n_1$ , represents the decay rate of the helium concentration. A larger  $n_1$  indicated a more rapid mixing of the jet with the free stream. Figure 35 shows the  $\alpha_{\max}$  data and curve fit results for all four injection configurations. These experiments are intended to model hydrogen-

air combustion, so the hydrogen mass fraction necessary for stoichiometric combustion with air is included in Fig. 35 as a reference. Mixing distance, defined as the distance necessary for concentration to decay to the stoichiometric hydrogen-air value, is also important for combustor design considerations. This distance was calculated from the curve fits of Equation [3.1] for each test configuration. The resulting mixing distances and  $n_1$ 's are tabulated in Table 4.

Figure 35 and Table 4 show some of the results of adding the oscillating shock to the helium injection flow field. The rate of concentration decay for the baseline helium injection is  $n_1 = 1.02$ . For the water injection with  $d_j = 0.159$  cm, the decay rate decreased by 36% to  $n_1 = .65$ . In the water injection with  $d_j = 0.079$  cm, the decay rate decreased by approximately 3%. A direct contrast is evident in the final water injection configuration ( $d_j = 0.040$  cm), where the decay rate has increased by 10% so that  $n_1 = 1.12$ . This trend is also evident in the mixing distances determined for the four different cases. In the baseline configuration, the jet would reach the stoichiometric  $H_2$ -air concentration at  $x/d = 109$ . This distance increases by 104% to  $x/d = 222$  for the largest water injector. The mixing distance also increases, but by only 20%, to  $x/d = 130$  for the  $d_j = 0.079$  cm water injector. Again, in direct contrast to the previous water injectors, the presence of the smallest water injector and its attendant oscillating shock causes the mixing distance to decrease by 16% to  $x/d = 91$ . This is also indicated in the concentration plot, Fig. 34, which shows a maximum concentration  $\alpha_{max} = 0.03$ , which is just above the stoichiometric  $H_2$ -air ratio, at  $x/d = 90$ .



### 3.3.3 Jet Core Penetration

The jet core penetration data presented in Table 3 was used to generate a plot of core penetration versus axial location, Fig. 36. The data for  $\alpha_{\max}$  penetration was fit with a logarithmic equation of the form:

$$\left(\frac{z}{d}\right)_{\text{core}} = n_2 \ln\left(\frac{x}{d}\right) + \beta_2 \quad [3.2]$$

where the rate of core penetration,  $n_2$ , and  $\beta_2$  were determined from the curve fit. These values are summarized in Table 5.

The effect of the oscillating shock on penetration can be seen in Fig. 36 and by examining the different penetration rates,  $n_2$ . For the baseline injection, the core penetration growth rate was  $n_2 = 1.42$ . Adding the oscillating shock from the largest water injector ( $d_j = 0.159$  cm) causes a 40% increase in  $n_2$ . The initial penetration is lower, but the penetration at  $x/d = 90$  is higher, increasing the penetration rate. As the water injector diameter is decreased from the first injector to  $d_j = 0.079$ , the core penetration rate drops to 0.68. This is a 52% decrease in core penetration rate over the baseline injector. The same trend continues with the smallest water injector,  $d_j = 0.040$  cm. Here, the penetration rate has decreased by 59% over the original helium-only configuration. These trends can also be seen by observation of Fig. 36. Core penetration at  $x/d = 20$ , from highest to lowest, is  $d_j = 0.079$ ,  $d_j = 0.040$ , helium only, and  $d_j = 0.159$ .

### 3.4 Other Mean Flow Results

Vertical profiles of other important mean flow variables were assembled into contour plots using the same Surfer software discussed earlier. Data was taken at each axial station for each flow configuration studied. The contour plots which will be presented and discussed in the following paragraphs have been nondimensionalized by their respective free-stream values as discussed in Section 2.4.6.

#### 3.4.1 Total Pressure Contours

Total pressure losses of any kind are undesirable in a high Mach number airbreathing engine and efforts must be taken to control these losses. Some of the sources of total pressure loss in such a system are fuel injection and any attendant shocks, viscous interactions near the walls, and freestream-jet mixing interaction. The oscillating shock introduced into the flow field in these experiments adds another source of total pressure loss which must be considered. Nondimensional total pressure contours are presented which will allow better study of the losses associated with these injection schemes.

Figures 37 - 40 present the contour plots of  $P_{t1}/P_{\infty}$  for all four configurations at  $x/d = 20$ . During a no-injection tunnel run, the total pressure climbs uniformly from a low value near the floor to the freestream value. There are no visible disturbances in the flow. This is in direct contrast to the plots in Figs. 37 - 40. In all four of these figures, there is a clear total pressure deficit close to  $y/d = 0$ , corresponding to the presence of the helium injector. Careful comparison of each of these figures with the corresponding helium concentration plot shows that the low total pressure region very nearly matches the injectant contours. This deficit region provides a means of locating the approximate

location of the jet in the flow field. Also noteworthy is the shape of the total pressure contours on either side of the low pressure region. In all four cases, the contours begin to "flatten out", outside of  $y/d = -2$  and  $y/d = 2$ , returning to an approximately uniform flow field. Also, in all four instances, the minimum total pressure ratio near the center of the plots is  $P_{t1}/P_{t\infty} \approx 0.2$ .

Similar information is presented in Figs. 41 - 44 for the four flow configurations at  $x/d = 40$ . As at the previous measurement station, the area with the largest total pressure deficit closely corresponds with the helium contours presented earlier. There are similar areas of near uniform flow on both sides of the high loss region. All four of the plots show some problem areas in the upper regions of the contours. In these areas,  $P_{t1}/P_{t\infty}$  is greater than 1.0, indicating some errors in the calculation of  $P_{t1}$  from the concentration and Pitot pressure data.

Total pressure contours for the last axial station are shown in Figs. 45 - 48. These plots show many of the same trends discussed for the two previous measurement stations. As before, there are areas of apparent calculation errors, indicated by  $P_{t1}/P_{t\infty} > 1.0$ , in the last 3 figures. The baseline contour and the contour for the 0.159 cm water injector are similar in appearance, with the water injection contour showing a larger area of low total pressure in the center of the plot. This may be the result of the strong oscillating bow shock induced by the water injection. Figures 47 and 48 for the other two water injection configurations are very similar in appearance and are very different from Figs. 45 and 46. While these figures provided some indication of the variations in total pressure for each injector configuration, a quantitative comparison

would also provide insight into the changes in total pressure loss between the 4 configurations.

Mays<sup>11</sup> developed a nondimensional total pressure parameter,  $P_{\varphi}$ , which could be used to compare the total pressure loss of each configuration. This total pressure parameter was formulated based on a single vertical profile taken at  $x/d = 90$ ,  $y/d = 0$ . As shown in Figs. 37 - 48, the total pressure changes in the flow field can not be adequately quantified by the single vertical profile. Fuller<sup>23</sup> has taken the original formulation of Mays and extended it to allow for a more accurate analysis of the total pressure losses in the flow field. This new total pressure parameter is then defined as:

$$P_{\varphi} = \frac{\int_{y_i}^{y_f} \int_{z_i}^{z_f} \rho u P_t dA}{\int_{y_i}^{y_f} \int_{z_i}^{z_f} \rho_{fs} u_{fs} P_{tfs} dA + \rho_j u_j A_j P_{tj}} \quad [3.3]$$

where the integral in the numerator represents the total pressure of the flow including any total pressure losses caused by shocks or jet-freestream interaction. The term  $\rho u P_t$  was found by multiplying the mass flux by the calculated values of  $P_t$  at the same measurement position. The integral was then evaluated by finding the volume below the surface defined by this weighted total pressure flux.<sup>23</sup>

The two terms in the denominator of Equation [3.3] represent the two "inputs" to this mixing flow field. Tunnel free-stream conditions measured at  $x/d = 90$  were used to find  $\rho_{fs}$ ,  $u_{fs}$  and  $P_{tfs}$  from the mean flow probes. The integral was then evaluated as

described for the numerator. The helium injectant conditions were used, in the isentropic relations, to determine the second term in the denominator.

The parameter,  $P_{\phi}$ , is then a ratio of the total pressure of the actual flow field to the total pressure of the combined tunnel free stream and the helium injector. If the flow field were "loss free", the calculated value of  $P_{\phi}$  would be one. Similarly, if  $P_{\phi}$  were equal to zero, it would indicate a complete loss of total pressure in the flow. Thus, if there are total pressure losses due to the oscillating shocks or due to jet-freestream interactions, the value of  $P_{\phi}$  would be between zero and one. A low total pressure loss would be represented by a value of  $P_{\phi}$  close to one and a high total pressure loss would show up as a small value of  $P_{\phi}$ .

As explained by Fuller, the limits of integration in both integrals of Equation [3.3] were set based on data taking limits and observation of the concentration flow field. Limits in  $z$  were set at  $z_i = 0$ , or the floor, and  $z_t = 8$ , or the upper limit of significant helium penetration. The limits in  $y$  were set at the limits of the data taking range,  $y/d = -4$  and  $y/d = 4$ . Mays' total pressure parameter used iteratively determined penetration heights for each  $P_{\phi}$  calculation. These heights were easily determined for a single vertical profile but would be much more difficult to determine for this type of two-dimensional flow field. This method should be more accurate than the method of Mays since it determines the total pressure parameter based on lateral and vertical total pressure measurements instead of the single centerline measurement.

The results of the  $P_{\phi}$  calculations are presented in Table 6. As can be seen there,  $P_{\phi} = 0.63$  for the baseline configuration and decreases to a low of  $P_{\phi} = 0.54$  for the

water injection with  $d_j = 0.159$ . These values agree with observations made earlier about the nanoshadowgraphs. Since the only major disturbance in the baseline injection is the helium itself, this configuration should have the highest value of  $P_{\text{tp}}$ . Also, in the water injection shadowgraphs, it was noted that the shock angles of the two smallest injectors were nearly the same, while the shock angle for the largest injector was higher, indicating a stronger shock and a larger total pressure loss.

### 3.4.2 Mach Number Profiles

Mach number contours are presented in Figs. 49 - 52, for  $x/d = 20$ , and Figures 54 - 57, for  $x/d = 90$ . In Figs. 49 - 52, there is a low Mach number region, at about  $M = 1.6$ , which corresponds with the approximate location of the jet core center. The nominal Mach number for these tests was 3, however, as can be seen in Figs. 49 - 52, the highest Mach number at the edge of the contours is approximately 2.7. This could be due to a slight misalignment of the water injector plate causing a slight decrease in Mach number or due to shocks from the plate or bow shocks from either of the injectors. As can also be seen in the first four figures, there is a point in each flow field where the Mach number begins to change very rapidly. This occurs approximately at the edge of the jet and was probably caused by the mixing of low Mach number gas from the helium jet with the higher Mach number gas from the free stream. The downstream component of the helium jet at the exit of the injector was approximately 1.4 times the freestream velocity. Figure 53 shows a typical contour plot of  $U_1/U_{\infty}$  at  $x/d = 20$ . As can be seen here, there is a region of higher velocity near the center of the plot corresponding to the jet core location. The maximum value will not be as high as that calculated above since

the jet has also passed through the oscillating shock before reaching the  $x/d = 20$  measurement location.

At the final axial station,  $x/d = 90$ , the Mach contours, Figs. 54 - 57, show smaller gradients and a somewhat more uniform appearance. This agrees well with the results from the concentration plots. For most configurations, the helium has mixed well with the freestream air producing a more uniform gas composition and Mach number profile. This is also shown in the velocity contours, Figs. 58 - 61. The velocities are relatively uniform and the jet velocity is nearly indistinguishable from the surrounding free stream velocity.

### *3.4.3 Static Properties*

The static pressure contour of Fig. 62 is typical of all the static pressure profiles for these tests. The static pressure is approximately uniform across the measurement station. The introduction of the oscillating shocks causes an increase in the static pressure above the calculated freestream value. There may also be static pressure changes due to the presence of the water injector plate in the test section.

Static temperature differences between the helium jet and the free stream provide a further means of "tracking" the helium injectant in the flow field. In these tests, the static temperature of the helium was approximately 2.1 times the free stream static temperature. At  $x/d = 20$ , as seen in Figs. 63 - 66, the static temperature ratio clearly shows the presence of the higher temperature helium injectant. By  $x/d = 90$ , Figs. 67 - 70, there is no longer a core of higher temperature fluid, the temperature profiles are

more uniform across the test section. The jet and the surrounding fluid have come to a more even temperature distribution than was present at  $x/d = 20$ .

#### *3.4.4 Integrated Mass Flow Rate*

From the calculated and measured mean flow parameters, the product of the mass flux and the helium mass fraction,  $\rho u \alpha_{He}$ , can be formed. Contours of  $\rho u \alpha_{He}$  at  $x/d = 90$  are shown in Figs. 71 - 74 for the four configurations. The higher values show the locations of significant helium concentration in the flow field. Integrating this parameter over the test section will yield the total mass flow rate of helium. The integration was done in the same manner described previously for  $P_{\psi}$ . Results for the mass flow integration at  $x/d = 90$  are given in Table 7. The actual mass flow, determined by the Rotameter installed in the helium supply line, was 0.0026 kg/s. As shown in Table 7, the integrated results were below this value for three out of four of the injection configurations.

#### *3.4.5 Entrainment*

Entrainment represents the amount of freestream air which is transported into the mixing region by turbulence. This entrained air mixes with the helium as the flow moves downstream. The amount of air entrained can be estimated by calculating the mass flow rate of air flowing into the injectant region. The total mass flow rate at  $x/d = 90$  can be determined by numerically integrating the  $\rho u$  profiles over the area of interest. The integration limits are similar to those determined for  $P_{\psi}$  in Section 3.4.1. The equation representing the mass flow rate is then:



$$\dot{m}_{tot} = \int_{y_i}^{y_f} \int_{z_i}^{z_f} \rho u dz dy \quad [3.4]$$

The results of Equation [3.4] can then be used in:

$$\dot{m}_{ent} = \dot{m}_{tot} - \dot{m}_{He} \quad [3.5]$$

to determine the mass flow rate of the entrained air. The mass flow rates of helium found by the analysis of the previous section were used in Equation [3.5] to determine the entrainment results. Air entrainment results for the four injection configurations are shown in Table 8. As can be seen in the table, the air entrainment rates varied from a low of 0.166 kg/s in the baseline configuration to 0.246 kg/s in the water injection configuration with  $d_j = 0.040$  cm. Some caution should be used when interpreting the entrainment data. The uncertainties in  $\rho u$ , as shown in Appendix A, are of the same order of magnitude as the helium mass flow rate.

### 3.5. Combined Kulite/Hot Wire Tests

The helium-off shock oscillation results discussed in the previous section give some information concerning the range of shock oscillation frequencies for the three different water injectors, but they do not give any means of determining if the shock oscillation was causing any changes in the helium mixing flow field. Another series of runs was conducted to determine any relationship which might exist between the oscillating shock and changes in the flow field downstream of the helium injector. For these tests, a single wire hot-wire probe was installed 12.4 d downstream of the Kulite location described in Section 3.2. The subsequent runs had both helium and water injection to allow study of the two together. The water injector plate was positioned to maintain the correct intersection point of the two bow shocks while allowing the oscillating water bow shock to hit the Kulite in the wind tunnel floor. Because of limitations in plate positioning, this particular test was conducted for only the two smaller water injectors ( $d_i = 0.079$  cm and  $d_i = 0.040$  cm). Data collected during these runs was reduced as described in Section 2.4.5 and the resulting coherence function was plotted for both injector configurations. The coherence function measures the extent to which one signal, in this case the hot-wire signal, can be predicted from another signal, such as the Kulite in these tests.<sup>22</sup>

Figure 75 is the resulting coherence function for the  $d_i = 0.079$  cm diameter water injector. The coherence function has variances which are defined by the number of averages used in calculating the coherence. For the number of averages used in this

analysis, values of  $\hat{\gamma}_{xy}^2$  above 0.3 are considered significant indications that the signals are related. As can be seen in this figure, there are two frequencies at which the coherence function is above the 0.3 threshold. One peak occurs in the lower frequency area between 10 kHz and 15 kHz at a coherence value of approximately 0.44 while there is another peak in the 80 kHz to 90 kHz range with a coherence value of about 0.32. These higher coherence values indicate a relationship between the two signals in the frequency ranges indicated above.

A more distinct peak can be seen in the coherence function plot for  $d_j = 0.040$  cm as shown in Fig. 76. Here the peak coherence value is 0.53 and occurs at a frequency of approximately 139 kHz. This is at approximately the same frequency as the shock oscillation frequency peak seen in Fig. 22. There are several peaks at frequencies lower than 139 kHz. These may be indications that there are other frequencies where the Kulite and hot-wire signals are related. The phase factor at the peak frequency was found to be approximately  $-42^\circ$ . This indicates that the Kulite signal was leading the hot-wire signal, which would be expected since the Kulite is mounted upstream of the hot-wire and should see the disturbance or change in the flow first.

Additional information about shock-induced changes in the flow was obtained with a hot-wire installed at the  $x/d = 90$  axial measurement station. This data is presented in Figs. 77 - 80 for the four different injection configurations. An FFT was performed on hot-wire data taken with the wire installed about 1.8 d from the floor at the most downstream measurement station. Figure 77 shows the resulting power spectrum for the baseline, helium-only, configuration. The hot-wire was tuned to a frequency response

of approximately 160 kHz so it is likely that the peak at 200 kHz is not an indication of a change in the measured flow field.

Figure 78 presents the same type of information for the 0.159 cm diameter water injector. Direct comparison with Fig. 77 shows that, on average, the power level in both cases is the same.

Similar information is presented in Fig. 79 for the next water injector,  $d_i = 0.079$  cm. In this case, comparing with the baseline, there are differences between the power level of the two signals. The overall shape of the curves is similar, but in this instance, the average power level is higher than it was in the baseline case. Additionally, there is a slight "plateau" in the signal in the frequency range of 60 kHz to 110 kHz.

Figure 80 shows the power spectral density for the  $d_i = 0.040$  cm water injector. As with Figs. 77 and 78, comparison of Figs. 79 and 80 shows that they are nearly the same. They show the same "plateau" feature and the same general shape for the rest of the frequency range considered. The overall power level is above that of the baseline, but essentially the same as the previous configuration. This indicates that the shocks resulting from the two smaller injectors had a similar effect on the turbulent flow field. Since the overall power levels for these two cases are higher than the baseline or the largest water injector case, this also indicates a more pronounced effect on the flow field due to the presence of the oscillating shocks.

### 3.6 Parallel Array Results

The methods of Section 2.4.6 were used to determine the large-scale structure angle, the integral time scale and the integral length scale for the turbulence structure of the flow field. These measurements were all made at  $x/d = 90$ . Cross-correlations with peak values of 0.3 and less were rejected in this analysis. Due to poor correlations at many of the measurement locations, comparisons between the four injection schemes are only possible at one vertical location. This location is approximately 2.0 d above the test plate.

As can be seen in Table 9, calculated structure angles varied from  $86^\circ$  in the baseline injection to  $60^\circ$  for the configuration with water injection through the 0.040 cm diameter injector. The  $86^\circ$  case is similar to the angles Clark<sup>18</sup> observed as the measurements approached the tunnel free stream.

Calculations of the integral time scale and integral length scale were also completed for this single measurement station. For the baseline, the integral time scale was approximately 9 microseconds with a corresponding integral length scale of 4.6 mm. With the addition of water injection through the 0.159 cm injector, the time scale is reduced to 6.6 microseconds and the length scale is reduced to 3.4 mm. For the other water injection cases, the results indicated a time scale of 6 microseconds or less. The hot-wires used in this test had a frequency response of 160 kHz; therefore, time scales of 6 microseconds or less could not be resolved.<sup>18</sup> Time scales of 6 microseconds and less correspond to length scales of 3.0 mm and lower. These length scales are dominant for the smaller diameter water injection cases.

## 4. DISCUSSION

Two sets of experiments were performed during this investigation. Both sets of tests were performed in the Virginia Tech supersonic wind tunnel at a freestream Mach number of 3.0. The baseline model for the tests was a single, sonic 5X underexpanded helium injector at a  $15^\circ$  downstream angle. During the first experiments, a single water injector of 0.159 cm diameter was used to investigate the effect of  $\bar{q}$  and shock impingement location on the mixing flow field. Injection at  $\bar{q} = 2$  and  $\bar{q} = 6$  was completed with shock impingement locations downstream of the helium injector, at the leading edge of the helium injector, and upstream of the helium injector. Initial concentration measurements indicated the most effective combination was a  $\bar{q} = 6$  jet with the oscillating shock impinging on the test plate downstream of the helium jet. Impingement upstream of the helium injector at either  $\bar{q}$  had little or no effect on the helium concentration. This is suspected to be the result of the oscillating shock disturbance being "filtered" by the boundary layer on the test plate. The remaining experiments were conducted with three different water injectors, each at  $\bar{q} = 6$ , with the shock impingement location held constant at a position downstream of the helium injector. Three different water injector diameters were selected to allow generation of oscillating shocks at different frequencies. Since the baseline injector was the same for all the experiments, the only variable in the experiments was the oscillating shock frequency. Therefore, any changes in helium mixing performance can be attributed to changes in shock frequency, shock strength or a combination of the two. For these tests,

it was hoped that the addition of a high frequency oscillating shock to the flow field would promote the helium mixing.

Nanoshadowgraphs of the four flow fields gave visual indications of oscillating shock angles, jet penetration and information on the mean size of the turbulent eddies in the injector flow field. Initial jet penetration was approximately the same for all four configurations. The helium jet had penetrated the boundary layer by  $x/d = 20$ , and by  $x/d = 90$ , the jet was indistinguishable from the rest of the flow field. As shock oscillation frequency increased, the maximum height of eddies above the tunnel floor decreased and the distance between eddies decreased as well. The average eddy length for all three shock oscillation configurations was approximately the same. As the eddies move into or out of the freestream, they will be able to entrain differing amounts of air and hence alter the mixing. Thus, a change in eddy size may be an indication of a change in the mixing performance.

Results of the shock oscillation frequency measurements indicated the presence of a high frequency, approximately 140 kHz, oscillation in the water injection experiments with  $d_j = 0.040$  cm. Tests with  $d_j = 0.159$  cm. showed a change in the level of the power spectrum over the level for the baseline case but there was no distinct shock frequency peak in this case.

While the shock frequency tests showed the presence of a high frequency oscillation, it was also important to determine if the shock oscillation was having any effect on the mixing flow field. The results of the Kulite/hot-wire coherence analysis showed a high coherence level between the Kulite, which was sensing the pressure

changes due to the oscillating shock, and the hot-wire sensing changes in the downstream flow field.

Helium concentration plots were developed from the helium concentration data. Results of the baseline experiments provide a basis for comparison of the three combined injection configurations. Examination of the contour plots at  $x/d = 90$  for the three combined injection configurations shows a definite trend. As the shock oscillation frequency increased, as a result of decreasing the water injector diameter, both the maximum concentration and its vertical position decreased. One possible explanation for this behavior is increased small-scale mixing with increasing frequency. As mixing increases, there is increased streamwise momentum transfer between the freestream and the helium jet plume. Thus, penetration may be affected by the interaction between the normal component of momentum from the jet and the streamwise component of momentum of the freestream. Increased mixing efficiency may also result in lower penetration.

Further examination of the same concentration plots, this time at  $x/d = 20$ , shows another interesting result of the introduction of the shock from the water jet into the flow field. The initial penetration of the  $d_j = 0.159$  cm water jet is lower than the initial penetration for the other two water injection cases. As was seen in the measurements of freestream shock angle, the shock caused by the injection using the 0.159 cm injector was the strongest of the three. The shock angles in the other two configurations were approximately the same. As the freestream air passes through the shocks, it is deflected downward toward the test plate. This flow deflection in the freestream may serve to



further "depress" the helium jet profile resulting in reduced initial penetration. The reduced penetration in the case with the strongest shock may be the result of this flow deflection.

An important basis for comparing gaseous injection schemes is the rate at which the mass fraction of the injectant decays with axial distance. A high decay rate indicates significant fuel-air mixing. It was found here that the presence of the oscillating shock resulting from the largest water injector caused a 36% decrease in decay rate over the baseline injection, while in the configuration with the highest frequency oscillating shock, the decay rate increased by 10% over the baseline. The middle-sized water injector caused a 3% decrease in injectant decay rate.

A major consideration in scramjet design is combustor length. This leads to the need to minimize mixing distances in order to keep the length of the combustor down. Since these tests were designed to simulate hydrogen-air combustion, the stoichiometric hydrogen-air ration was used in determining the required mixing lengths. As would be expected, the trends in mixing distance follow the trends in concentration decay. The mixing distance for the  $d_j = 0.159$  cm water injector was 222 d or a 104% increase over the baseline mixing length of 109 d. For the  $d_j = 0.079$  cm water injector, the mixing length increased by 20% over the baseline. In the case of the smallest water injector, the mixing length decreased by 17% to 91 d. This distance is just downstream of the last axial measurement station.

Jet penetration is another measure of mixing performance. High penetration values indicate improved entrainment and greater freestream mixing. The  $d_j = 0.159$  cm

water jet showed a 40% increase in penetration growth rate over the baseline configuration. The opposite behavior was observed with both the other water injectors. For  $d_j = 0.079$  cm, the penetration growth rate decreased by 52%. Similarly, for  $d_j = 0.040$  cm, the penetration growth rate decreased by 59% over the baseline penetration growth rate.

It is important to quantify any total pressure losses in the flow due to the oscillating shocks or the helium injection. This has been done by calculating the total pressure parameter,  $P_{\text{tp}}$ , as described in Section 3.4.1. As discussed earlier, the higher the value of  $P_{\text{tp}}$ , the less total pressure loss in the flow field. In the baseline configuration,  $P_{\text{tp}}$  was found to be 0.63. This indicates a 37% total pressure loss in the baseline flow configuration. The most significant total pressure loss, 46%, occurred in the combined injection configuration with the 0.159 cm diameter injector. In both of the other water injection configurations,  $P_{\text{tp}} = 0.58$ , indicating a 42% total pressure loss. This confirms that the introduction of the oscillating shock into the flow field increased the total pressure loss, as would be expected, and that the stronger shock caused the largest change in total pressure loss, again, as would be expected. The largest water injector caused a 14% increase in total pressure loss, while the other two injectors caused an approximately 8% increase in total pressure loss.

The final area of comparison for the four injection configurations is entrainment of freestream air into the mixing region. All three configuration with oscillating shocks present showed improved entrainment over the helium-only baseline configuration. The biggest increase, 48% came with the smallest diameter water injector ( $d_j = 0.040$  cm)

installed. The increases for the other injectors were 26% for  $d_j = 0.159$  cm and 47% for  $d_j = 0.079$  cm.

A decision on the best configuration requires consideration of trade-offs between injectant decay rates, penetration and mixing properties, and total pressure losses. The baseline used here was previously determined by Mays<sup>11</sup> to be the best of the four studied based on such a trade-off. Comparison of the three water injection configurations with the baseline shows some improvements and some losses. The 0.159 cm diameter water injector configuration, corresponding to the lowest oscillation frequency, showed a 36% decrease in decay rate, a 104% increase in mixing length, a 40% increase in penetration rate and a 14% increase in total pressure loss over the baseline. The second water injector configuration,  $d_j = 0.079$  cm, exhibited a 3% decrease in decay rate, a 20% increase in mixing length, a 52% decrease in penetration growth rate, and an 8% increase in total pressure loss. The final configuration,  $d_j = 0.040$  cm, corresponding to the highest frequency shock, showed a 10% increase in decay rate, an accompanying 17% decrease in mixing length, a 59% decrease in penetration rate, and an 8% increase in total pressure loss.

If total pressure loss were the only consideration, then the two smaller water injectors would be equally attractive. When changes in decay rate and mixing length are considered as well, the best combination is the helium injection configuration with the 0.040 cm diameter water injector.

## 5. CONCLUSIONS AND RECOMMENDATIONS

These experiments have investigated the effect of oscillating shock impingement on the mixing of a  $15^\circ$  downstream-angled, underexpanded, sonic, helium jet injected into a supersonic flow. Initial tests of shock impingement location and  $\bar{q}$  found the most significant changes to occur when the oscillating shock from  $\bar{q} = 6$  water injection impinged on the injection flow field downstream of the helium injector just as the plume emerged from the wall boundary layer. The remaining experiments were conducted to determine the effect of shock oscillation frequency on the mixing performance. The impingement location and  $\bar{q}$  were held constant, while the water injector diameter was varied to change the shock oscillation frequency. Water injectors of 0.159, 0.079, and 0.040 cm were used for the experiments. Nanoshadowgraphs were used for visual studies of the flow field. Shock frequency was documented as was the relationship between the oscillating shock and changes in the flow field. Surveys of helium concentration, Pitot pressure, total temperature, and cone-static pressure were conducted at three axial locations for each of the four injection configurations. Performance parameters such as total pressure loss, concentration decay rate, mixing distance and core penetration rate, were calculated and used to compare the four injection configurations.

Studies of the nanoshadowgraphs found that, in all four injection configurations, the helium jet had penetrated the boundary layer by the  $x/d = 20$  axial station. By the final measurement station,  $x/d = 90$ , the helium jet was nearly indistinguishable from the

freestream. It was also clear from the shadowgraphs that the angle of the shock caused by the water injection decreased with decreasing injector diameter from  $32^\circ$  for  $d_j = 0.159$  cm to  $25^\circ$  for  $d_j = 0.040$  cm. This is because the smaller diameter  $\bar{q} = 6$  jets do not penetrate as far into the flow field and consequently do not cause as large a flow disturbance as the larger diameter jet. In all four configurations, large eddies were visible in the jet plume which would increase air entrainment and increase the mixing.

Measurements of shock oscillation frequency for the 0.159 cm injector did not reveal a single dominant frequency. Instrumentation problems occurred in the run with the 0.079 cm injector, so that data was discarded. There was a change in the power spectrum, for the 0.159 cm case, over the baseline tunnel power spectrum, but there was no single dominant frequency apparent. This was in direct contrast to the  $d_j = 0.040$  cm injector. Here, a clear frequency peak was present at approximately 140 kHz.

The major result of this study was that impingement of an oscillating shock on a high-speed shear layer can be used to control the rate of mixing. Depending on the shock oscillation frequency, mixing enhancement or inhibition can be produced.

Concentration decay rates were determined for all four configurations. It was found that in two of the water injection cases,  $d_j = 0.159$  cm and 0.079 cm, the decay rates decreased by 36% and 3% respectively. In the  $d_j = 0.040$  cm case, the highest frequency shock oscillation, the decay rate increased by 10%. Similar results were found for mixing length with the only mixing length decrease, 16%, occurring for the highest frequency case.

The core penetration rate was found to increase, by 40%, for the lowest shock oscillation frequency case. The opposite was true for both of the water injectors with the higher frequencies, with penetration rates decreasing by 52% for  $d_j = 0.079$  cm and by 59% for the  $d_j = 0.040$  cm injector.

Air entrainment rates were also determined for each of the configurations. Significant initial entrainment is critical for combustion systems. In these tests the configuration with the highest oscillating shock frequency showed the best entrainment rate, 0.246 kg/s, compared to 0.166 kg/s for the baseline injection case. This represents a 48% increase in air entrainment with the addition of the high frequency oscillating shock.

The total pressure loss was also studied for the four configurations. As was expected, the addition of the oscillating shock to the flow field caused an increase in total pressure loss over the baseline helium-only configuration in all three cases. The weakest shock and, hence, lowest additional total pressure loss came in the configuration with the  $d_j = 0.040$  cm water injector.

Of the three oscillating shock configurations considered here, the best mixing configuration is the 15° helium injector combined with the highest frequency oscillating shock ( $d_j = 0.040$  cm). The shock oscillated at a frequency near the "natural" frequency of the large eddies in the mixing flow field. This augmented the strength of the eddies and caused significant increases in the amount of air entrained by the eddies.

An effort was also made to better understand the interaction between the oscillating shock and the turbulence structure in the mixing region. Measurements were

taken from a wall pressure transducer sensing the oscillating shock and a hot-wire in the helium plume. A high and statistically significant coherence was found at approximately 139 kHz (for  $d_j = 0.040$  cm) suggesting effective driving of the large eddies in this frequency range.

There are many opportunities for further study related to the flow fields considered here. Further studies of the shock oscillation frequency, whether by non-intrusive measurements or high frequency response Pitot probes, are important to develop a better understanding of the change in oscillation frequency with changes in water injector conditions. Further study of the driving frequency for the large eddies in this type of mixing flow is also warranted. It is necessary to determine whether the driving frequency for a given configuration is a "point" frequency or if there is a band of frequencies which would produce similar results. Shock impingement location is another important consideration. The location selected produced changes in the mixing performance but it may be possible to "tune" the impingement location and further enhance the mixing performance. Finally, these studies have been restricted to a single freestream Mach number, 3. In order to determine the applicability of these mixing methods to high Mach number airbreathing propulsion, study at a higher freestream velocity and temperature, such as in the Mach 6 High Reynolds Number Tunnel at NASA Langley, should be considered.

## BIBLIOGRAPHY

1. Hallion, R.P., "The Hypersonic Revolution, From Scramjet to the National Aero-Space Plane, Volume II, 1964 - 1986," Special Staff Office, Aeronautical Systems Division, Wright-Patterson Air Force Base, Ohio, 1987.
2. Curran, E., and Stull, F., "The Potential Performance of the Supersonic Combustion Ramjet Engine," ASD-TDR-63-336, May, 1963.
3. Ferri, A., "Supersonic Combustion Progress," *Astronautics and Aeronautics*, August, 1964.
4. Kumar, A., Bushnell, D.M., and Hussaini, M.Y., "A Mixing Augmentation Technique for Hypervelocity Scramjets," AIAA Paper 87-1882.
5. Ferri, A., "Review of Problems in Application of Supersonic Combustion," *Journal of The Royal Aeronautical Society*, Volume 68, Number 645, September, 1964, pp. 575-595.
6. Swithenbank, J., "Hypersonic Air-Breathing Propulsion," *Progress in Aeronautical Sciences*, Volume 8, 1967, pp. 229-294.
7. Thomas, R.H., Schetz, J.A., and Billig, F., "Gaseous Injection in High Speed Flow," presented at Ninth International Symposium on Air Breathing Engines, Athens, Greece, September, 1989.
8. Schetz, J.A., and Billig, F., "Penetration of Gaseous Jets Injected into a Supersonic Stream," *Journal of Spacecraft and Rockets*, Volume 3, Number 11, November, 1966, pp. 1658-1664.



9. Cohen, L.S., Coulter, L.J., and Egan, W.J., "Measurements of the Penetration and Mixing of Gases Injected into Subsonic and Supersonic Air Streams," AIAA Paper 70-714.
10. Kwok, F.T., Andrew, P.L., Ng, W.F., and Schetz, J.A., "Experimental Investigation of a Supersonic Shear Layer with Slot Injection of Helium," AIAA Paper 90-0093.
11. Mays, R.B., "Experimental Investigation of Sonic Helium Injection at a Low Downstream Angle into Supersonic Flow," M.S. Thesis, Virginia Polytechnic Institute and State University, June, 1990.
12. Marble, F.E., Zukoski, E.E., Jacobs, J.W., Hendricks, G.J., and Waitz, I.A., "Shock Enhancement and Control of Hypersonic Mixing and Combustion," AIAA Paper 90-1981.
13. Menon, S., "Shock-Wave-Induced Mixing Enhancement in Scramjet Combustors," AIAA Paper 89-0104.
14. Shau, Y.R., and Dolling, D.S., "Experimental Study of Spreading Rate Enhancement of High Mach Number Turbulent Shear Layers," AIAA Paper 89-2458.
15. Muck, K.D., and Smits, A.J., "Behavior of a Turbulent Boundary Layer Subjected to a Shock-Induced Separation," AIAA Paper 84-0097.
16. Less, D.M., and Schetz, J.A., "Transient Behavior of Liquid Jets Injected Normal to a High-Velocity Gas Stream," AIAA Journal, Volume 24, Number 12, December, 1986, pp. 1979-1986.

17. Wood, C.W., Thomas, R.H., and Schetz, J.A., "Effects of Oscillating Shock Impingement on the Mixing of a Gaseous Jet in a Mach 3 Airstream," AIAA Paper 90-1982.
18. Clark, R.L., Jr., "A Study of the Large-Scale Structure in a Supersonic Slot Injected Flow Field," M.S. Thesis, Virginia Polytechnic Institute and State University, June, 1988.
19. Ng, W.F., Kwok, F.T., and Ninnemann, T.A., "A Concentration Probe for the Study of Mixing in Supersonic Shear Flows," AIAA Paper 89-2459.
20. Winkler, E.M., "Design and Calibration of Stagnation Temperature Probes for Use at High Supersonic Speeds and Elevated Temperatures," Journal of Applied Physics, Volume 25, Number 2, February, 1954.
21. Trans-Tek, Inc., "Displacement Transducer DC-DC Series 240, Bulletin S012-0030-KHD, May 1989.
22. Bendat, J.S., and Piersol, A.G., Random Data, Analysis and Measurement Procedures, John Wiley and Sons, Inc., New York, 1986.
23. Fuller, E.J., Personal Communication, March, 1991.
24. Kline, S.J., and McClintock, F.A., "Describing Uncertainties in Single-Sample Experiments," Mechanical Engineering, January, 1953.
25. Moffat, R.J., "Contributions to the Theory of Single-Sample Uncertainty Analysis," Journal of Fluids Engineering, Volume 104, June, 1982.

## TABLES

**Table 1. Test Conditions and Parameters**

<b>Injectant</b>	<b><math>\delta/d</math></b>	<b><math>d_j</math> (cm)</b>	<b><math>\delta_v/d_j</math></b>
<b>He only</b>	<b>1.6</b>	<b>-</b>	<b>-</b>
<b>He/H<sub>2</sub>O</b>	<b>1.6</b>	<b>0.159</b>	<b>2.1</b>
<b>He/H<sub>2</sub>O</b>	<b>1.6</b>	<b>0.079</b>	<b>4.3</b>
<b>He/H<sub>2</sub>O</b>	<b>1.6</b>	<b>0.040</b>	<b>8.6</b>

Table 2. Maximum Helium Concentrations ( $\alpha_{\max}$ )

x/d	He only	0.159	0.079	0.040
20	0.173	0.145	0.176	0.163
40	0.074	0.084	0.107	0.071
90	0.037	0.054	0.040	0.030

**Table 3. Locations of Maximum Concentration ( $z/d_{\alpha_{max}}$ )**

<b>x/d</b>	<b>He only</b>	<b>0.159</b>	<b>0.079</b>	<b>0.040</b>
<b>20</b>	<b>2.25</b>	<b>1.73</b>	<b>2.57</b>	<b>2.29</b>
<b>40</b>	<b>3.92</b>	<b>3.71</b>	<b>3.65</b>	<b>2.96</b>
<b>90</b>	<b>4.42</b>	<b>4.75</b>	<b>3.62</b>	<b>3.18</b>

**Table 4. Mixing Distance and Decay Exponent**

Case	Distance	$n_1$
He only	109 d	1.021
0.159	222 d	0.654
0.079	131 d	0.991
0.040	91 d	1.124

Table 5. Penetration Growth Rate Exponents

Case	$n_2$
He only	1.420
0.159	1.988
0.079	0.677
0.040	0.583



Table 6. Total Pressure Loss Parameter

Case	$P_{\phi}$
He only	0.630
0.159	0.543
0.079	0.584
0.040	0.583

**Table 7. Integrated Mass Flow Rates (kg/s)**

Case	$\dot{m}_{int}$
He only	0.0018
0.159	0.0027
0.079	0.0022
0.040	0.0016

**Table 8. Air Entrainment Rates (kg/s)**

Case	$\dot{m}_{ent}$
He only	0.166
0.159	0.210
0.079	0.245
0.040	0.246

**Table 9. Parallel Array Results**

Case	$\theta$	Time Scale (sec)	Length Scale (mm)
He only	86°	9 x 10 <sup>-6</sup>	4.6
0.159	77°	6.6 x 10 <sup>-6</sup>	3.4
0.079	66°	-	-
0.040	60°	-	-

## FIGURES

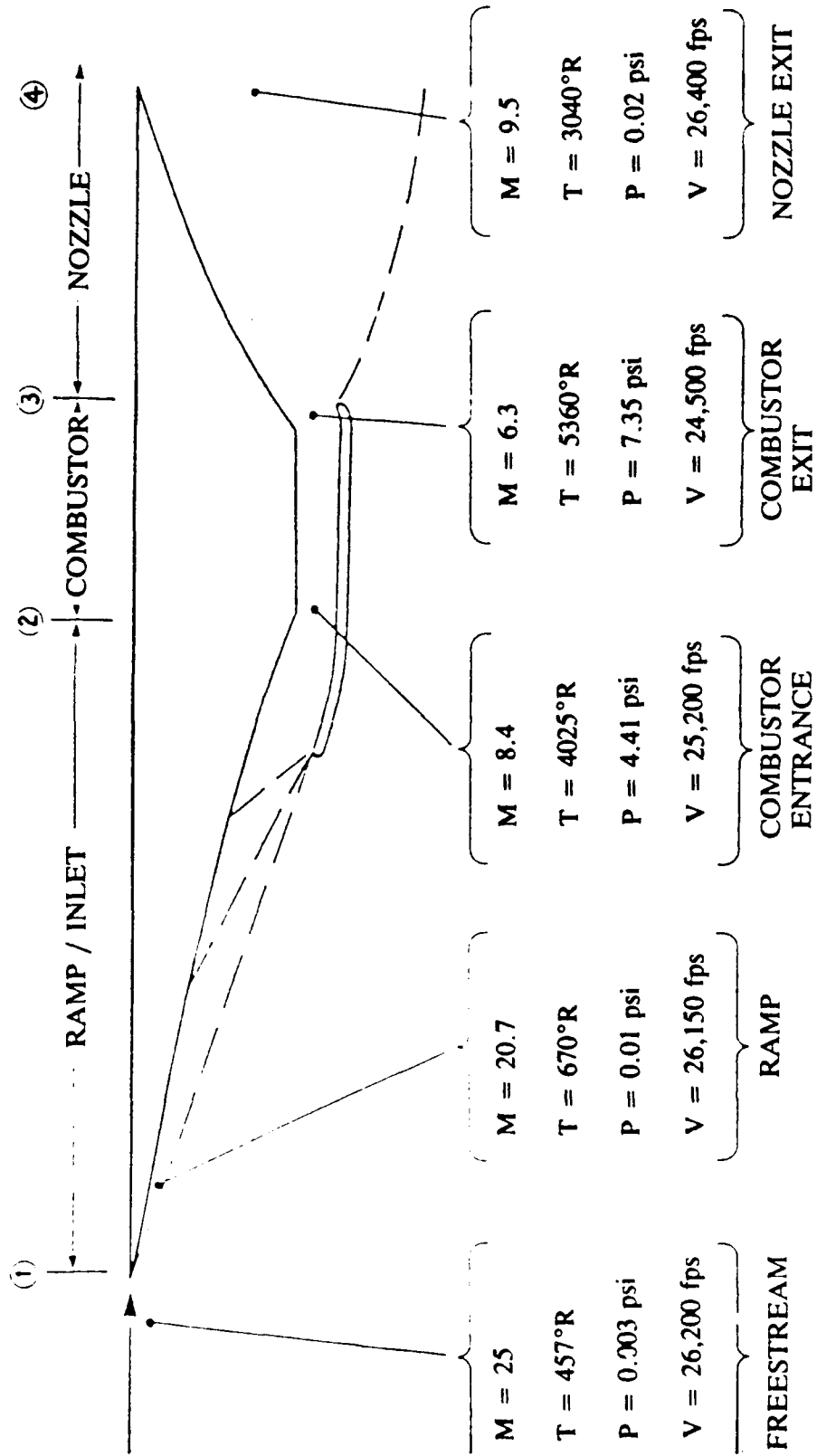
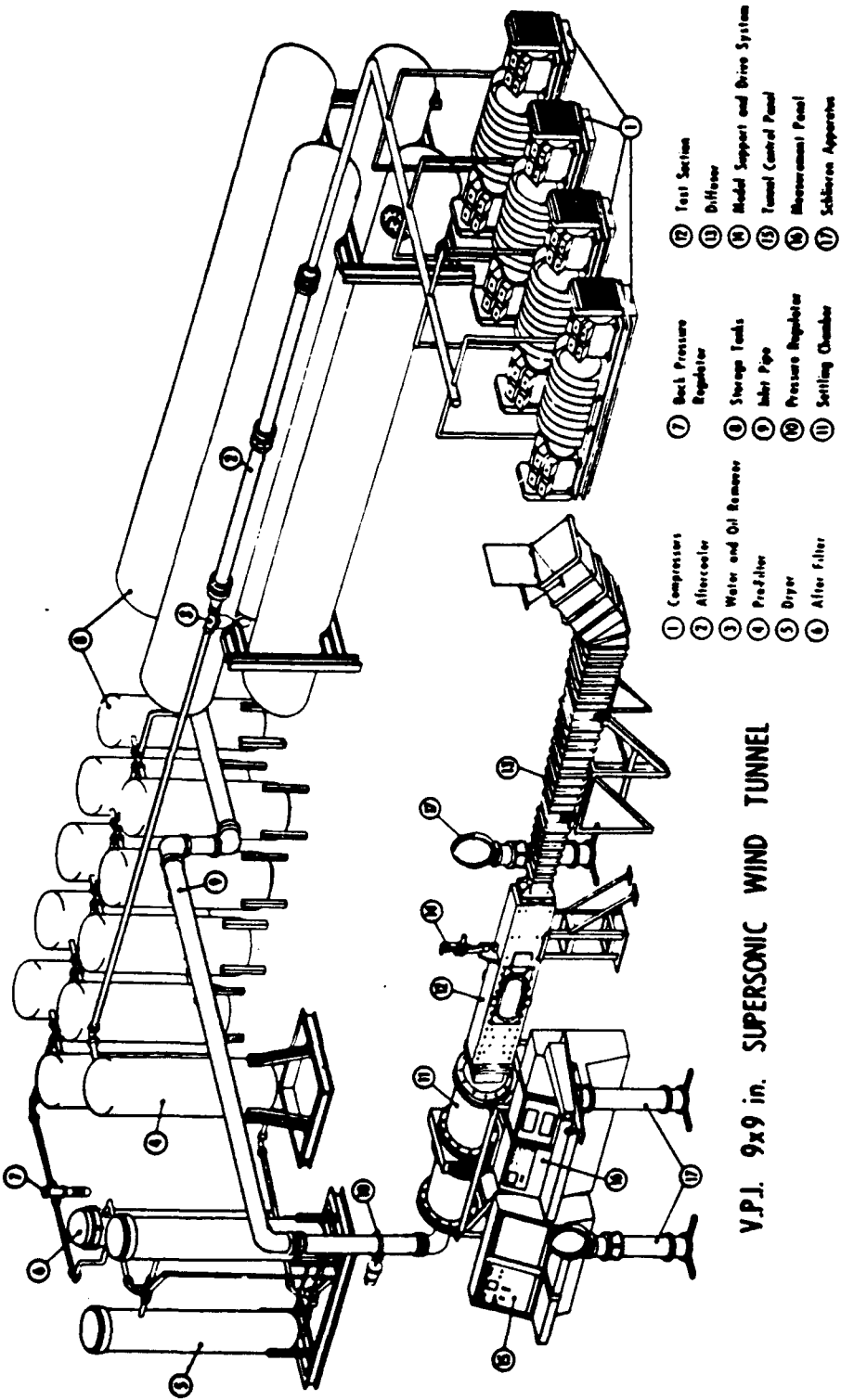


Figure 1. Example Scramjet Operating Conditions



V.P.J. 9x9 in. SUPERSONIC WIND TUNNEL

- ① Compressors
- ② Aftercooler
- ③ Water and Oil Separator
- ④ Pre-filter
- ⑤ Dryer
- ⑥ After filter
- ⑦ Back Pressure Regulator
- ⑧ Storage Tanks
- ⑨ Inlet Pipe
- ⑩ Pressure Regulator
- ⑪ Settling Chamber
- ⑫ Test Section
- ⑬ Diffuser
- ⑭ Model Support and Drive System
- ⑮ Tunnel Control Panel
- ⑯ Measurement Panel
- ⑰ Schlieren Apparatus

Figure 2. Virginia Tech Wind Tunnel

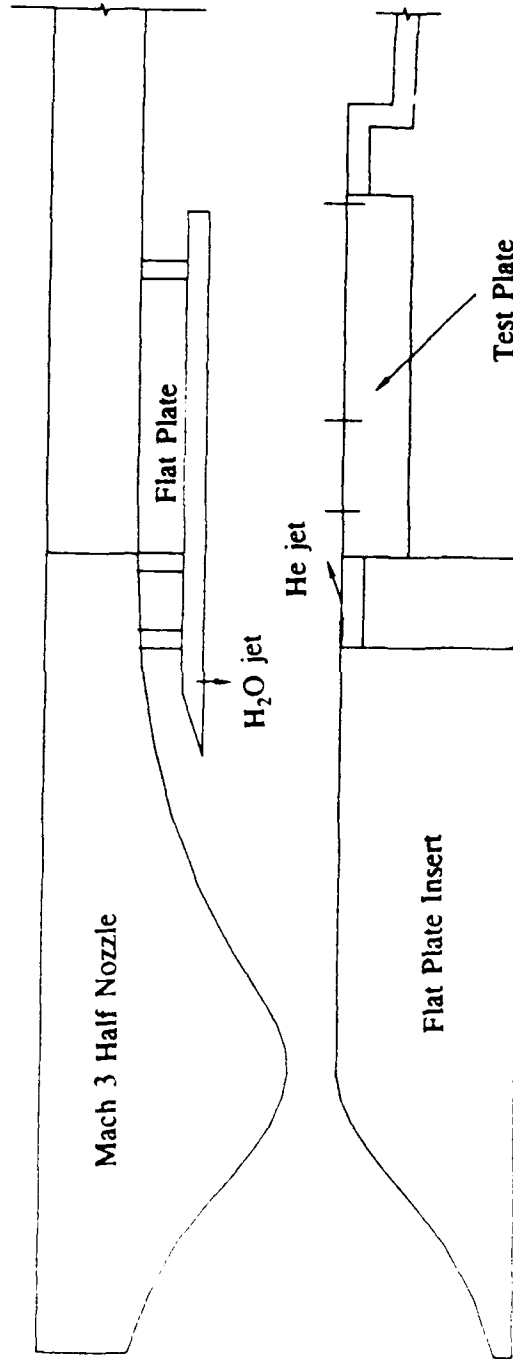


Figure 3. Sketch of Test Setup



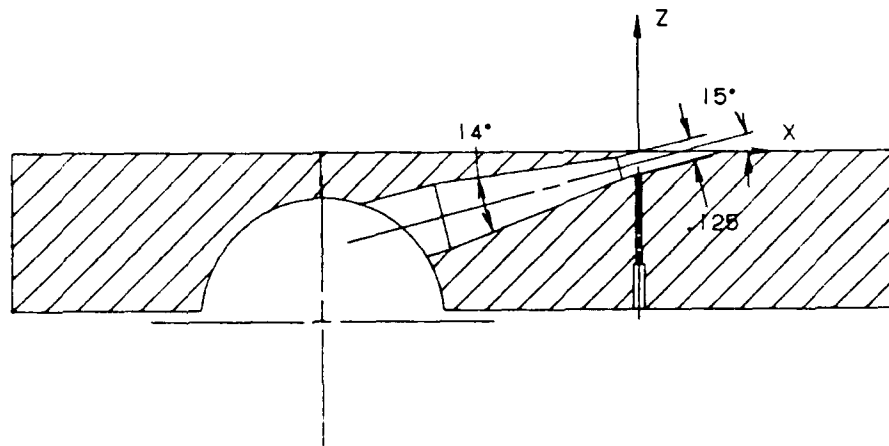
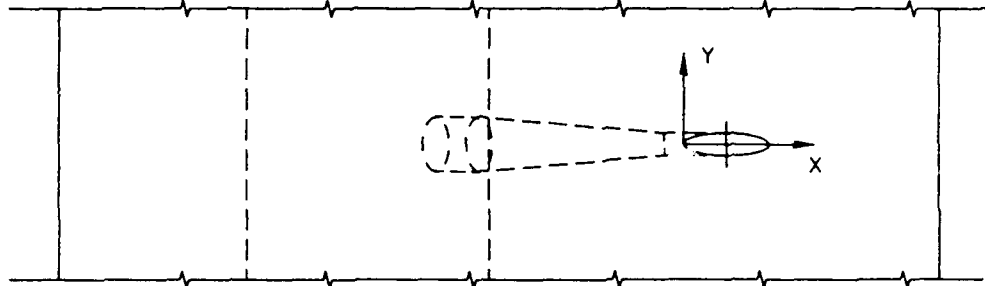


Figure 4. Sketch of Helium Injector

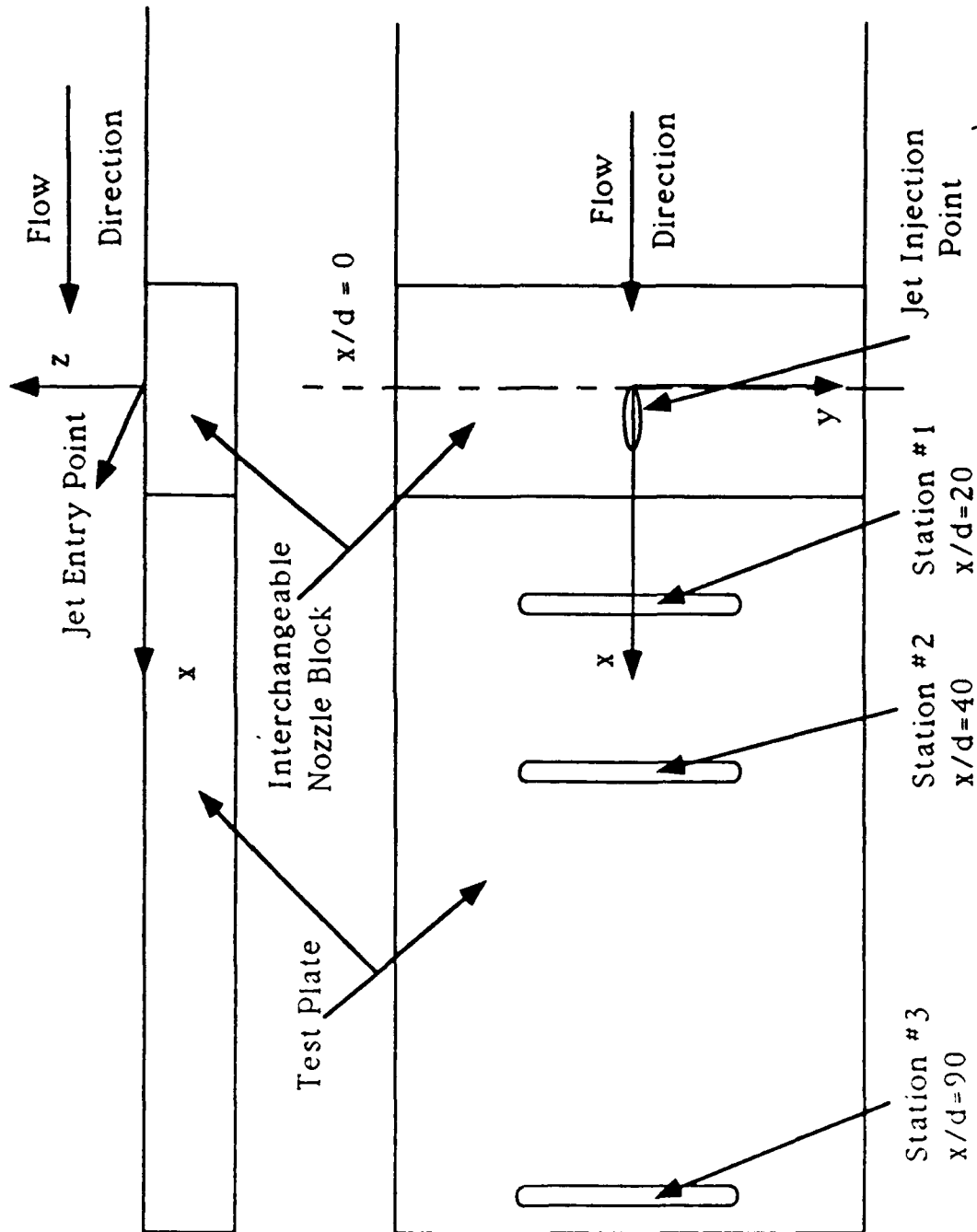


Figure 5. The Test Stations

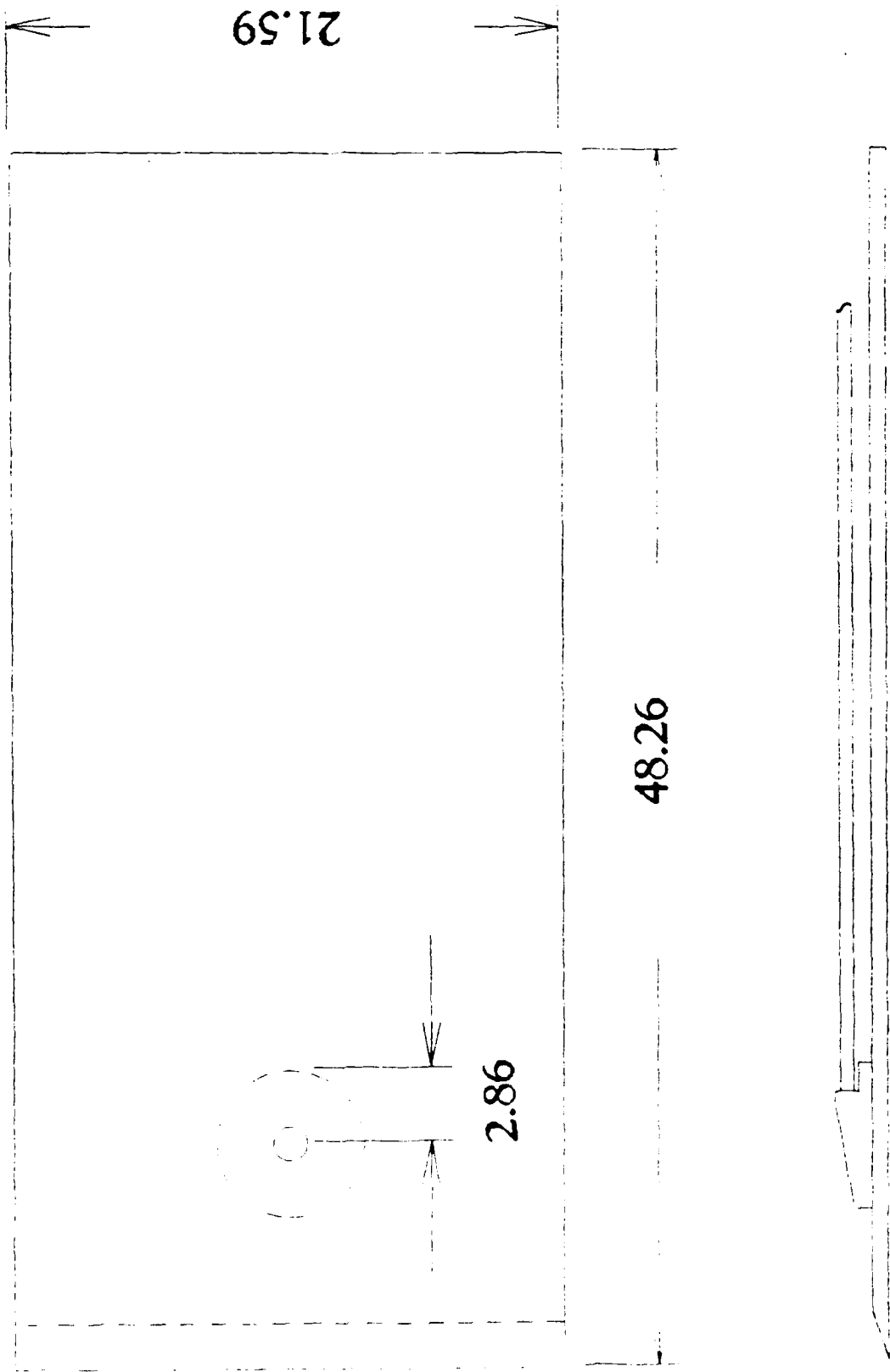


Figure 6. Water Injector Model

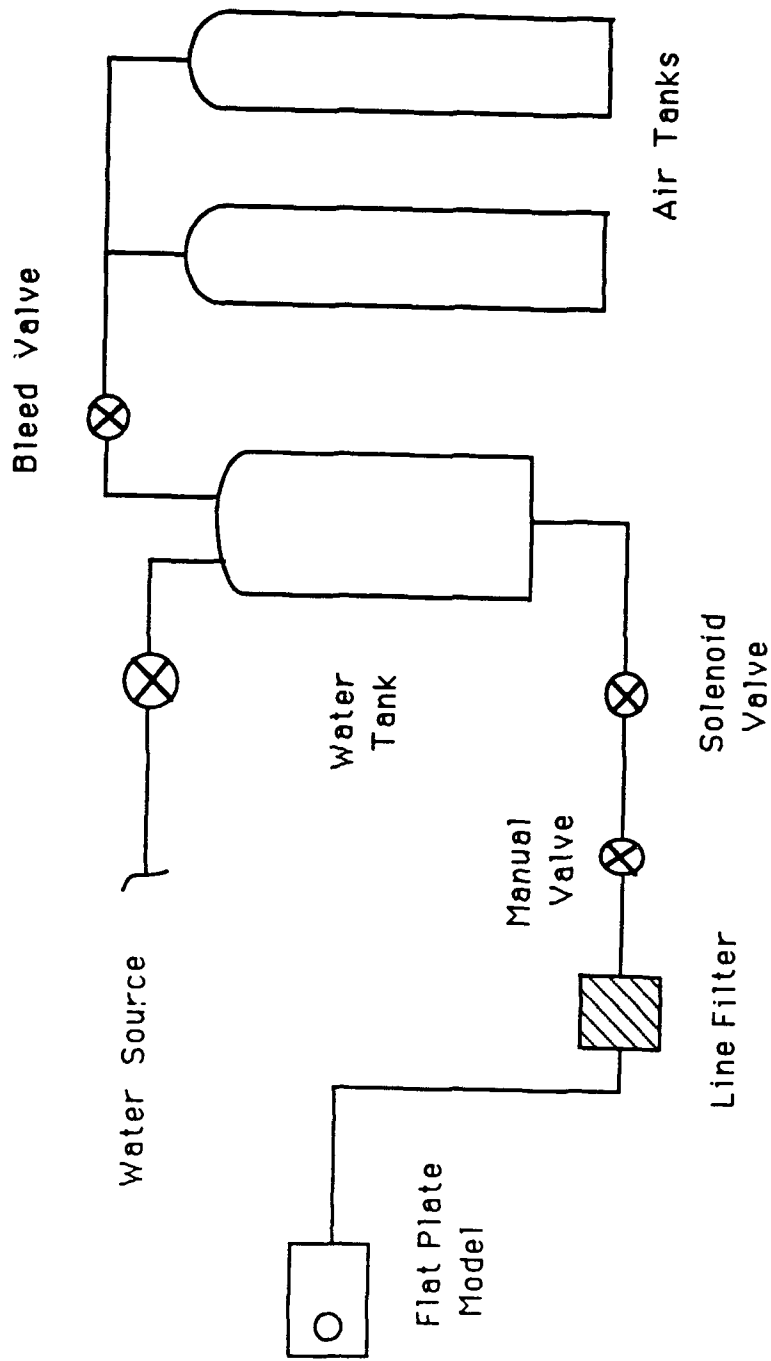


Figure 7. Schematic of Water Injection System

## The Nanoshadowgraph Optical Configuration

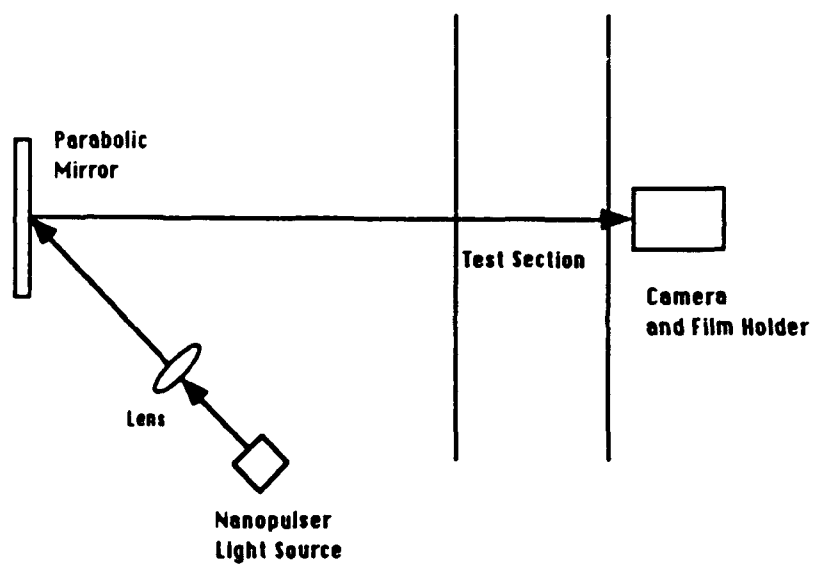


Figure 8. Sketch of the Nanoshadowgraph Optical System

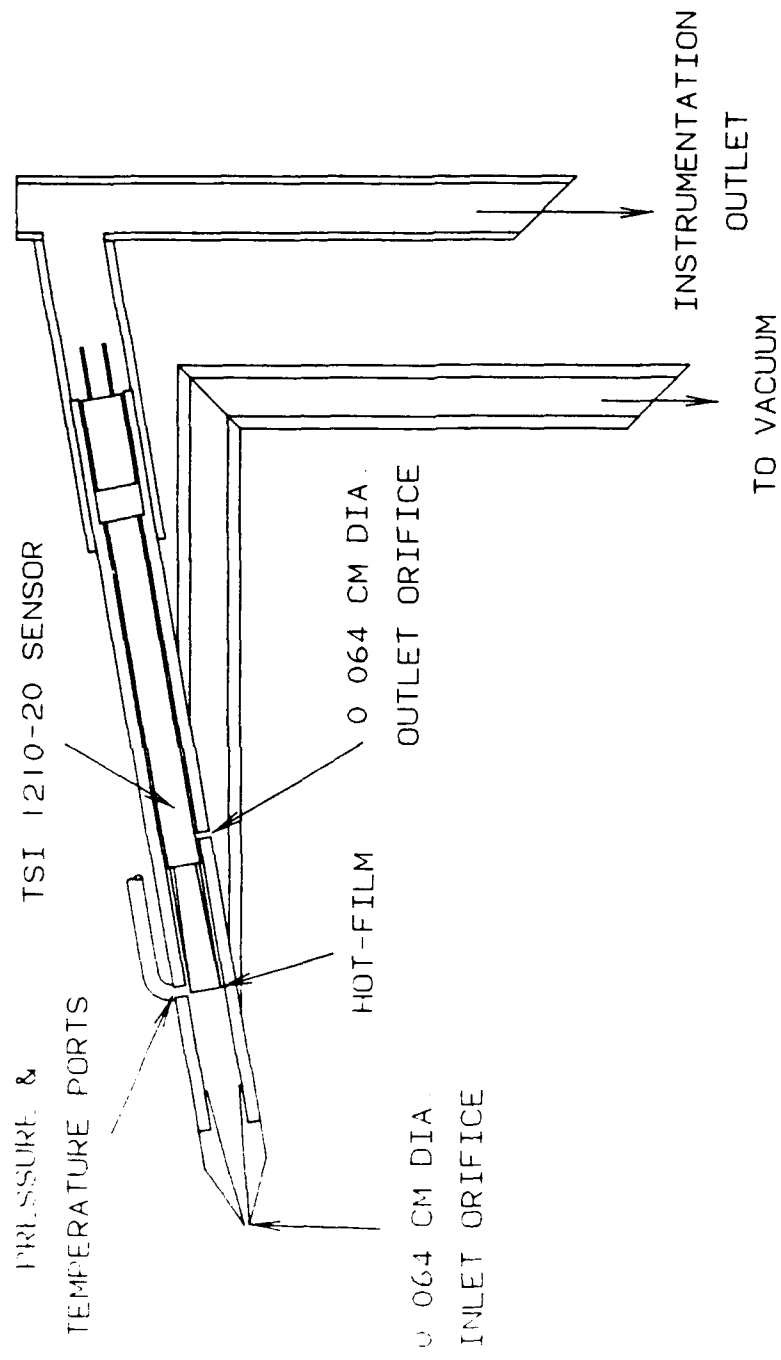


Figure 9. Concentration Probe Schematic

ACTIVE SENSOR LENGTH = 0.1 CM

FILM DIAMETER = 51 MICROMETERS

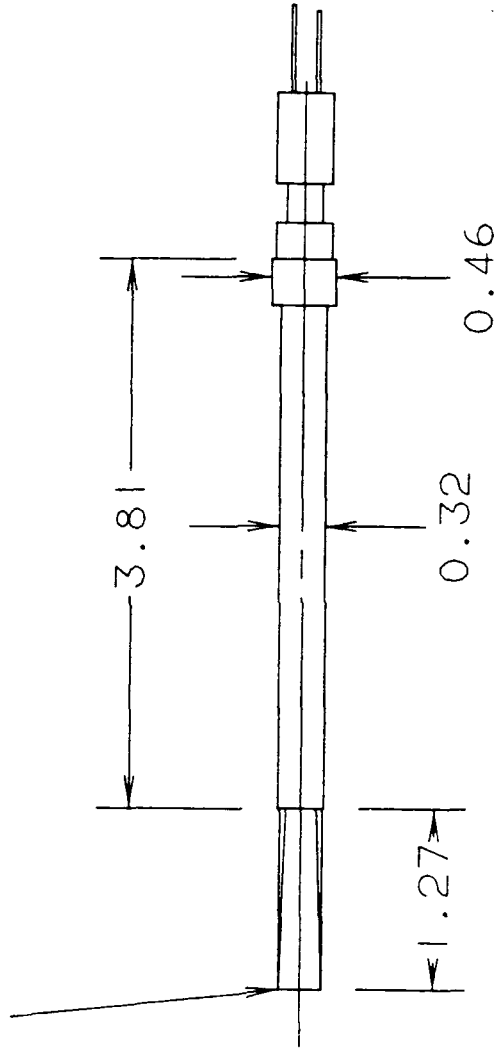


Figure 10. Concentration Probe Hot-Film Sensor

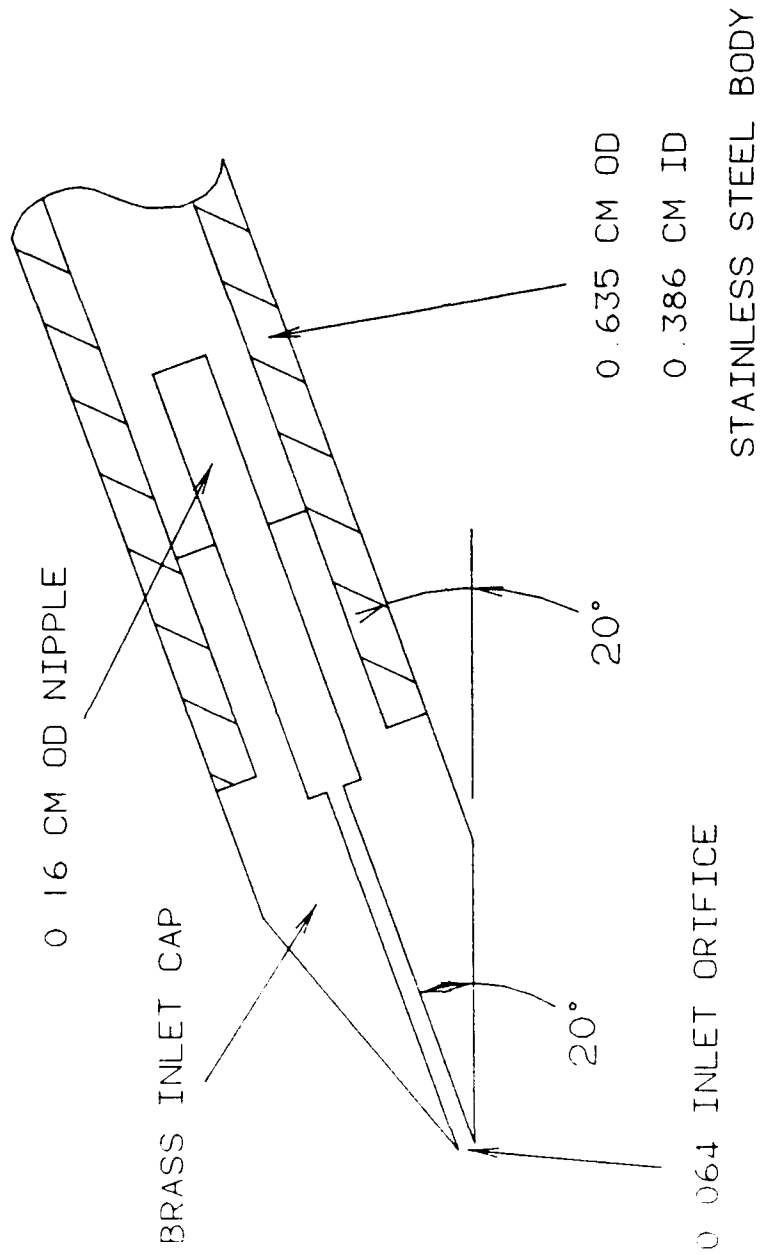


Figure 11. Pitot Pressure Probe



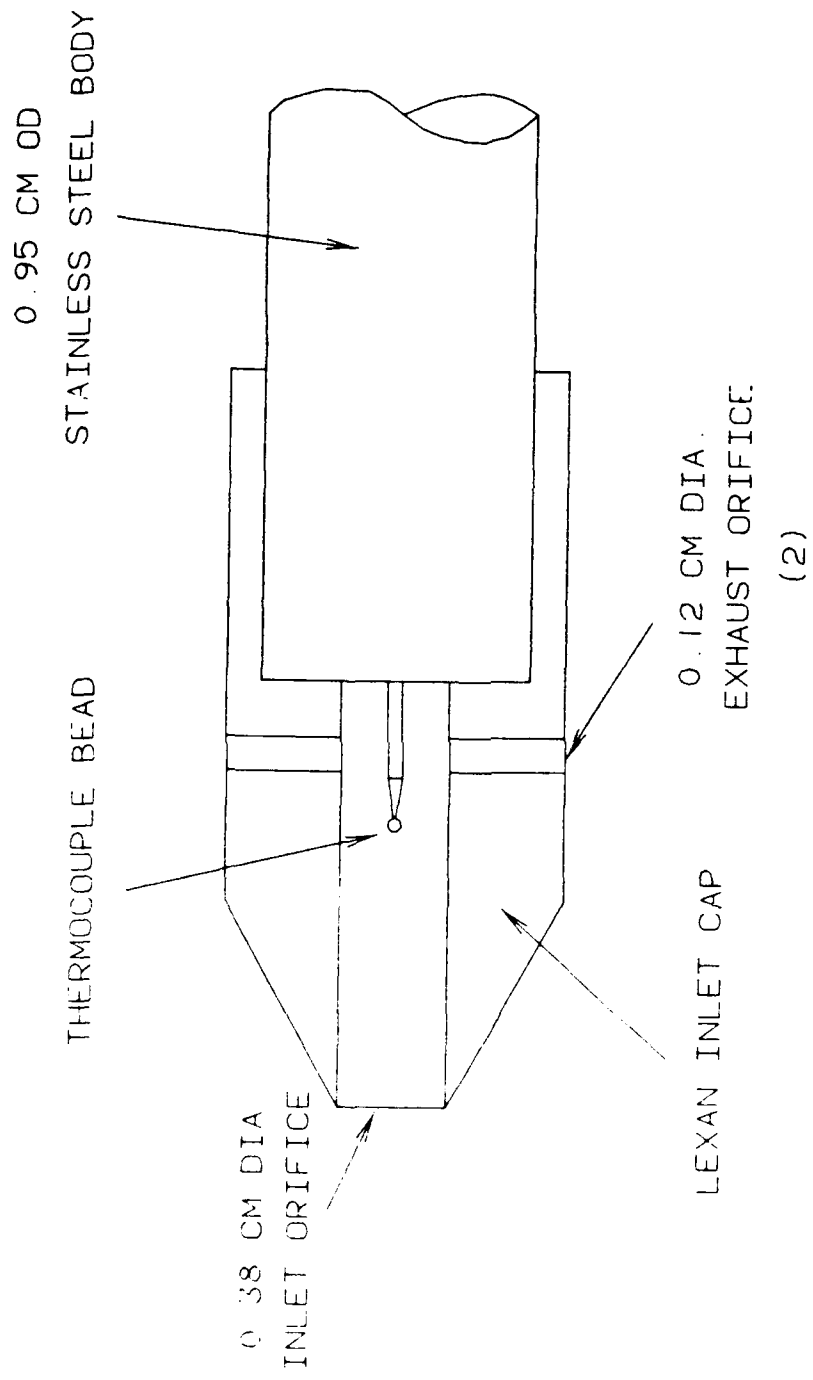


Figure 12. Total Temperature Probe

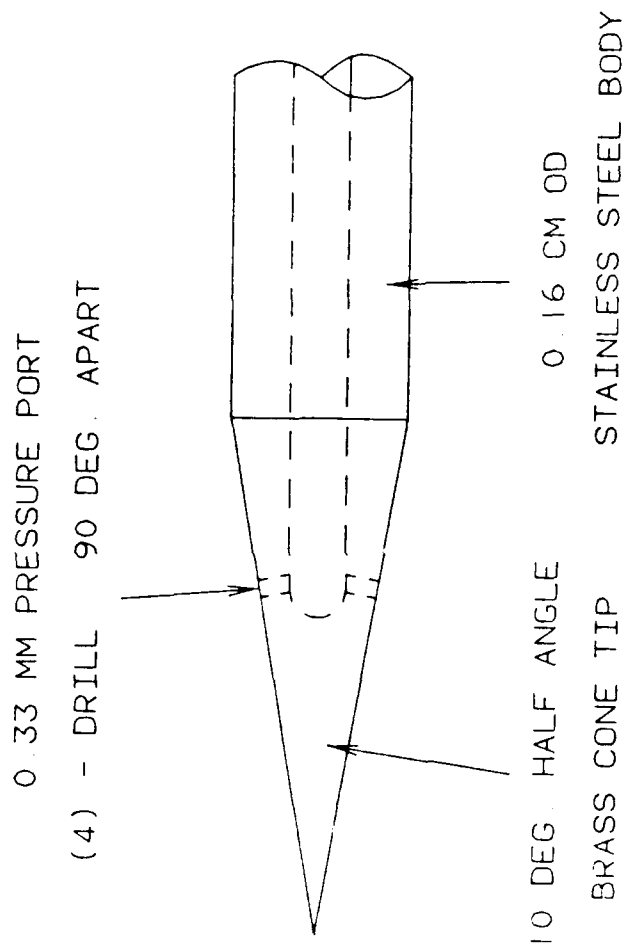


Figure 13. Cone-Static Probe

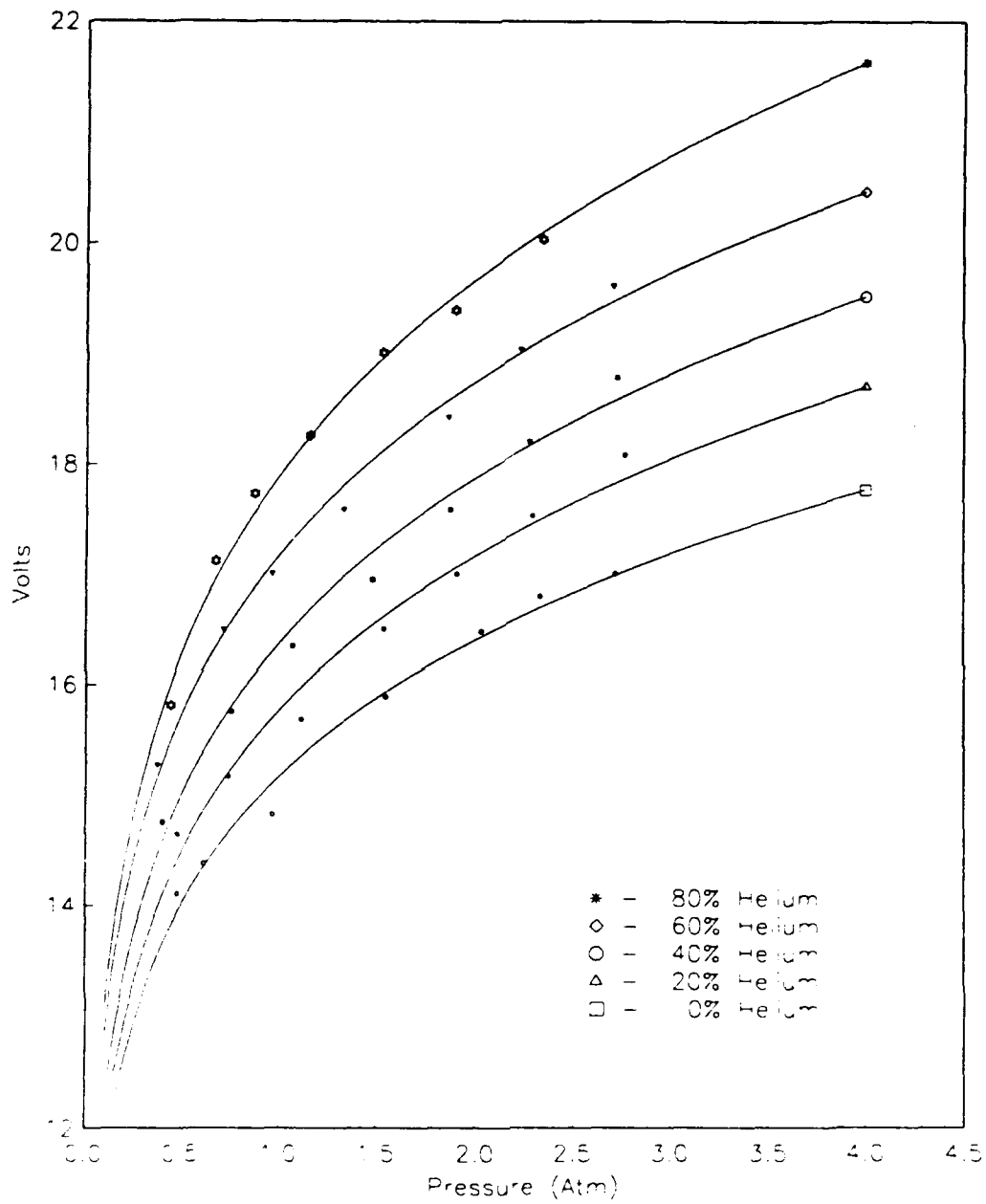


Figure 14. Concentration Probe Calibration Curves

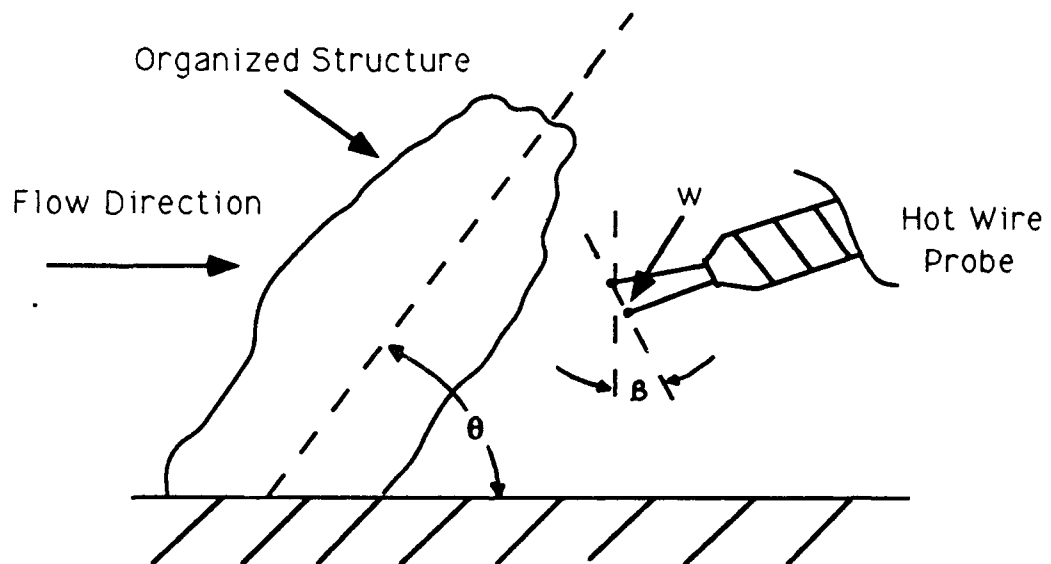


Figure 15. Sketch for Structure Angle Calculation

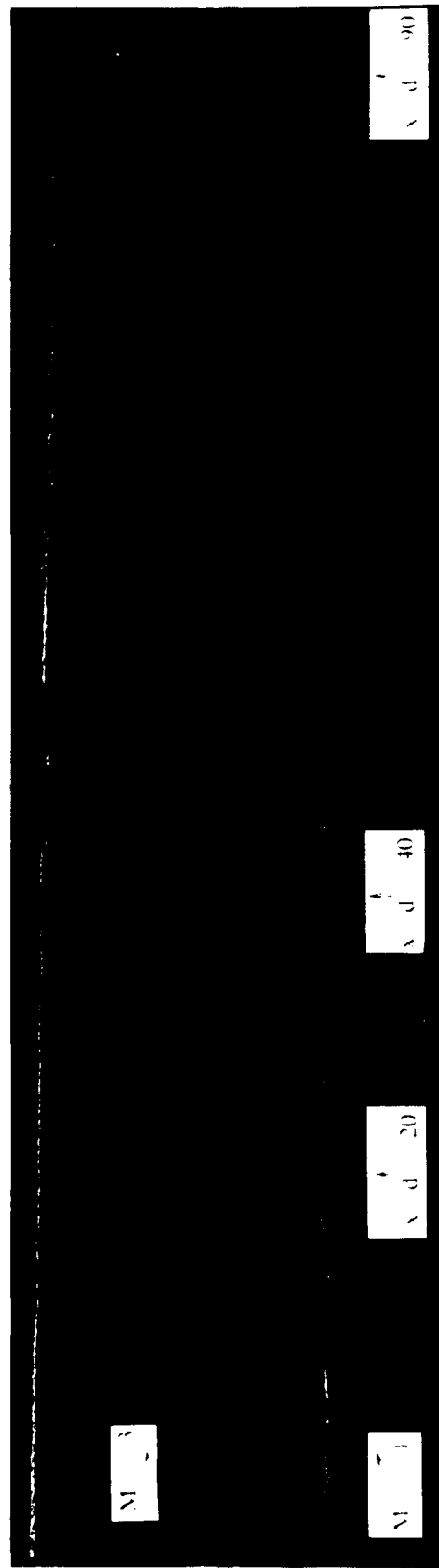


Figure 16. Nanoshadowgraph of Baseline Helium Injection

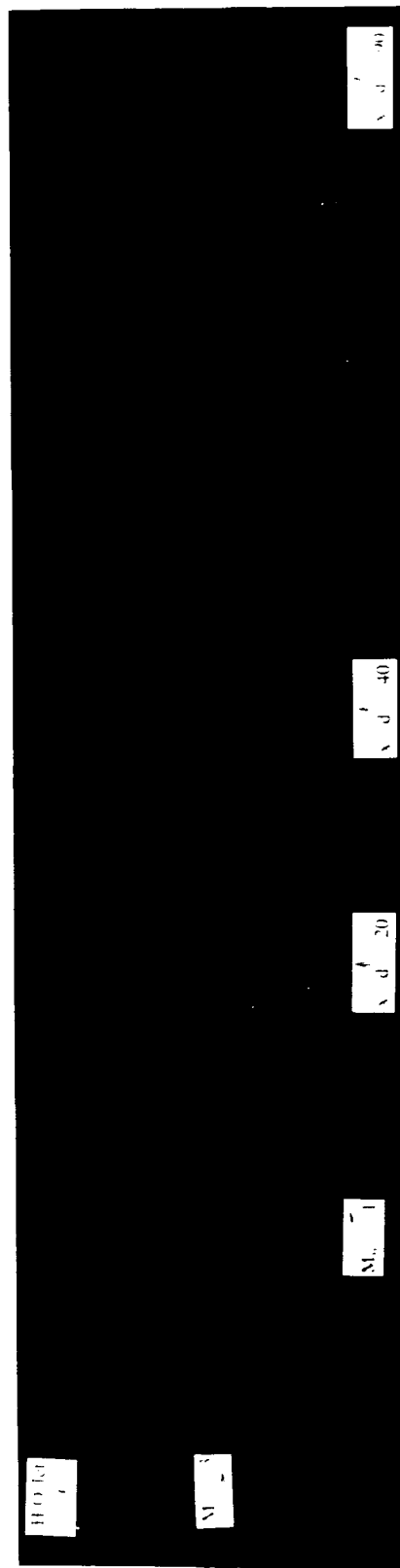


Figure 17. Nanoshadowgraph of Combined Injection ( $d_j = 0.159$  cm)

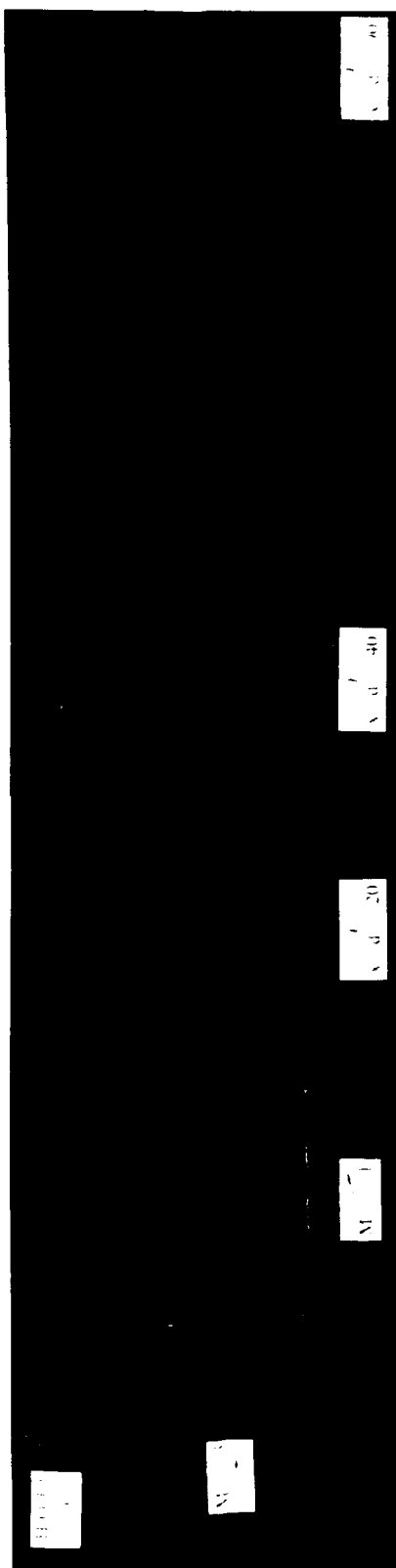


Figure 18. Nanoshadowgraph of Combined Injection ( $d_j = 0.079$  cm)

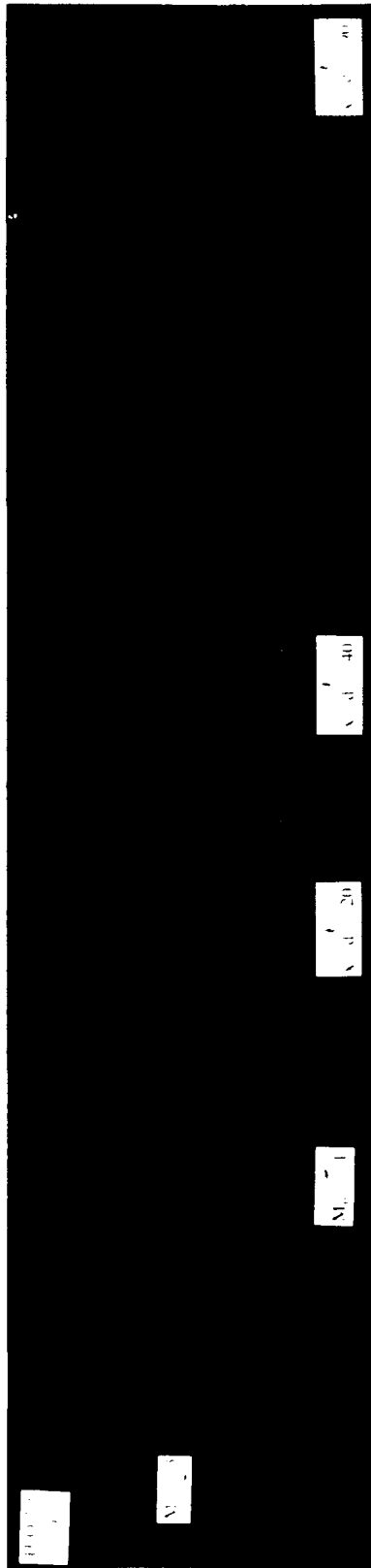


Figure 19. Nanoshadowgraph of Combined Injection ( $d_j = 0.040$  cm)



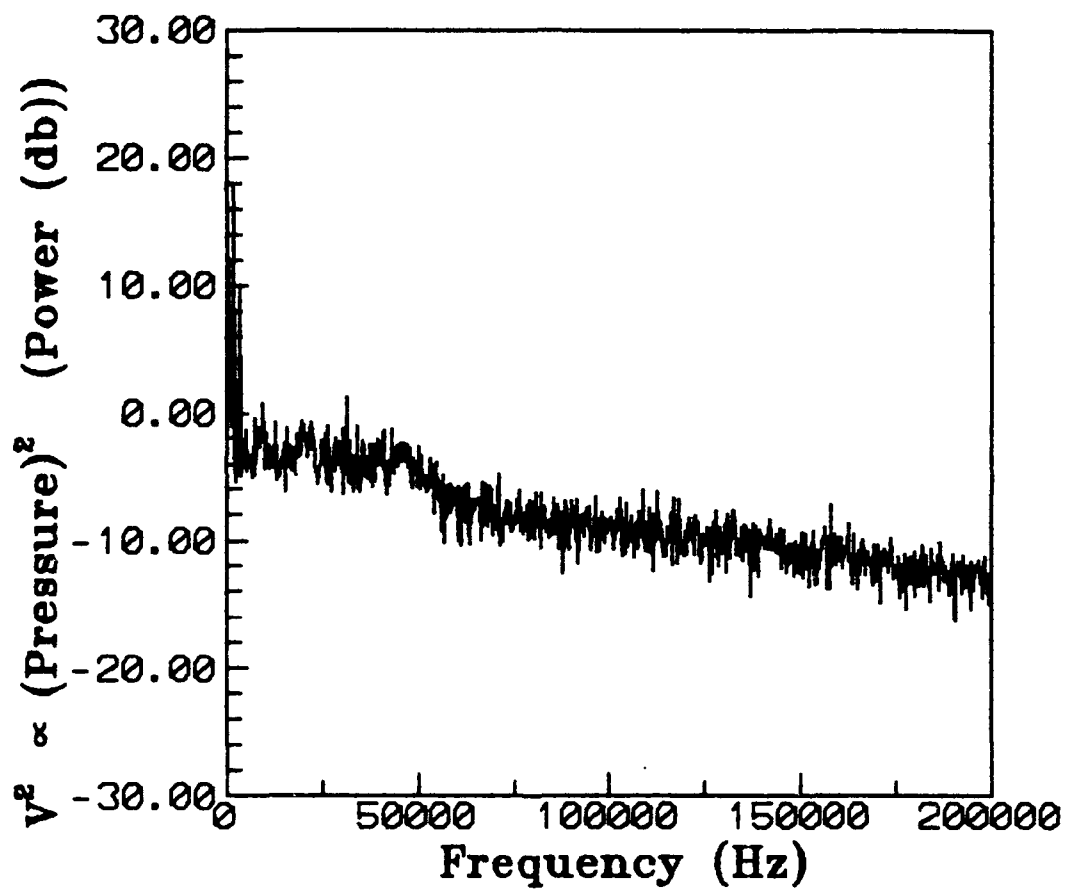


Figure 20. Kulite Power Spectrum, Baseline Injection

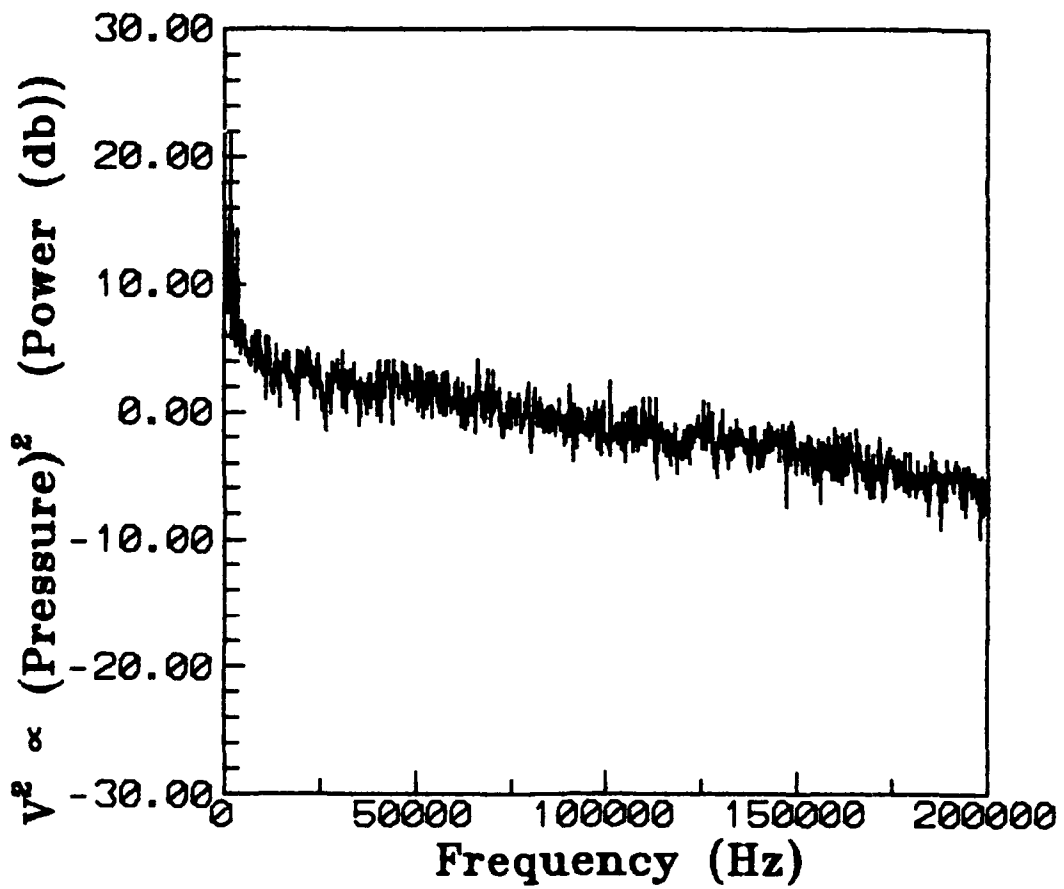


Figure 21. Kulite Power Spectrum, Combined Injection ( $d_i = 0.159$  cm)

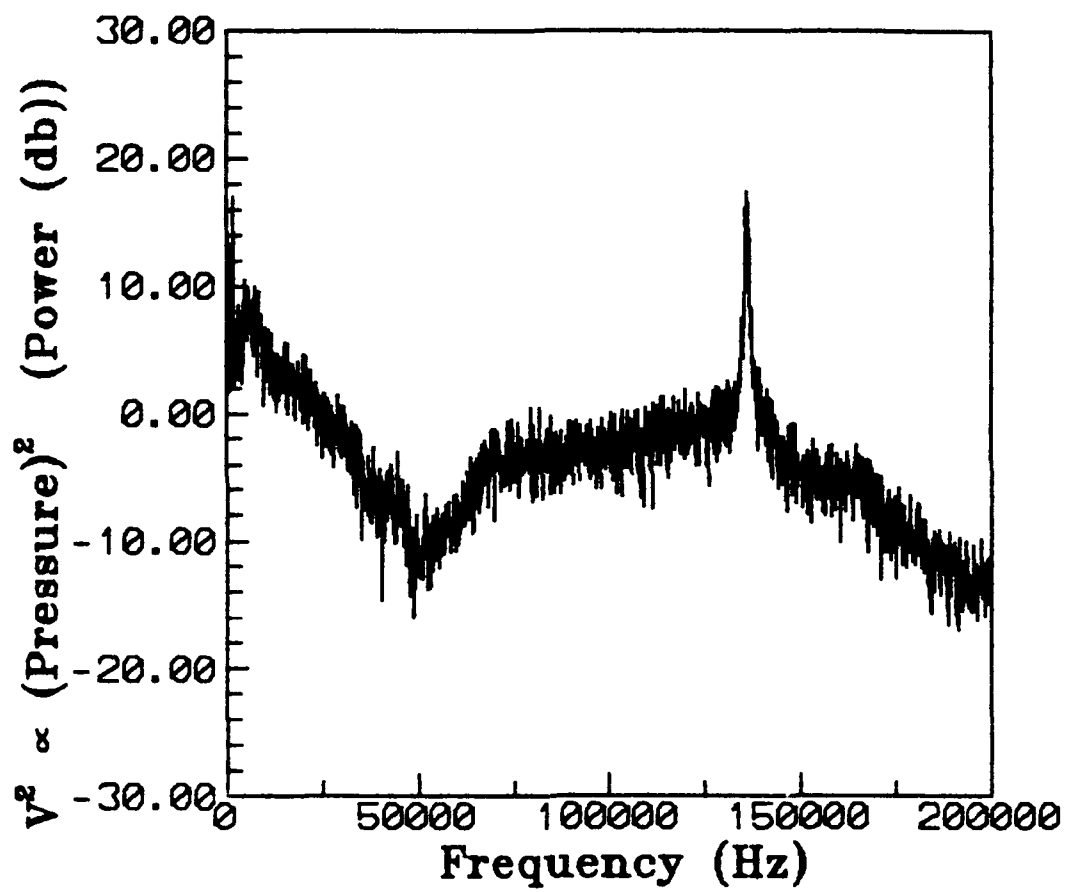


Figure 22. Kulite Power Spectrum, Combined Injection ( $d_i = 0.040$  cm)

$\alpha_{He}$   $x/d = 20$  Baseline

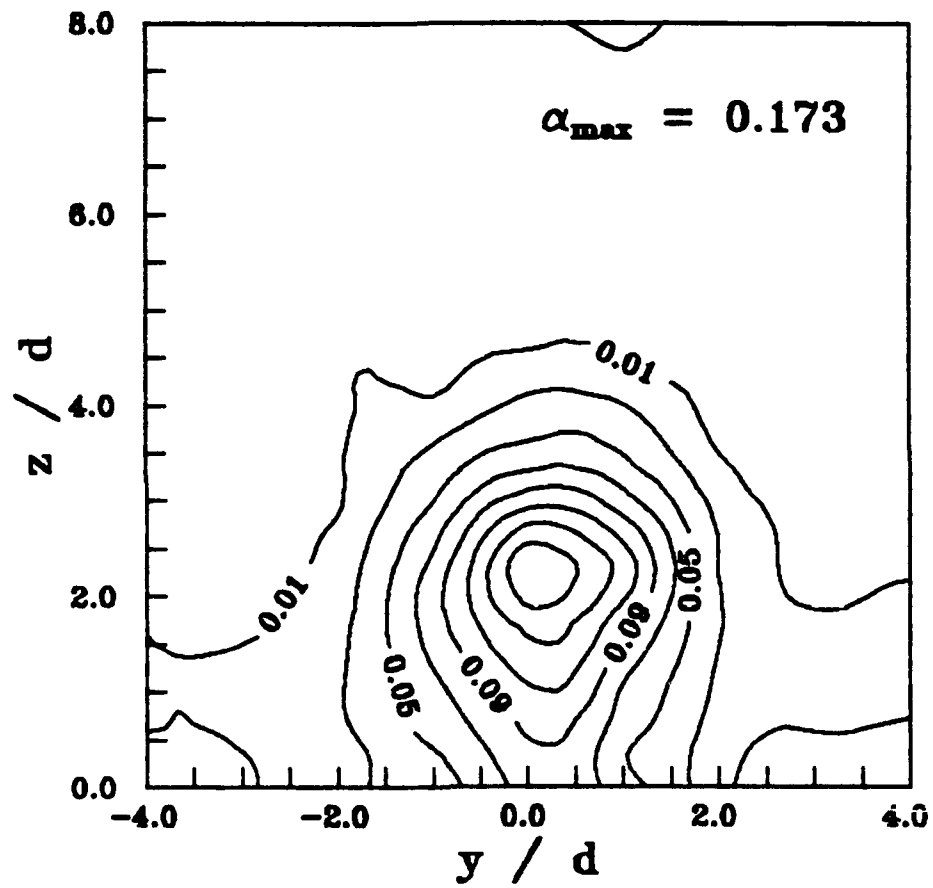


Figure 23. Helium Concentration, Baseline Injection,  $x/d = 20$

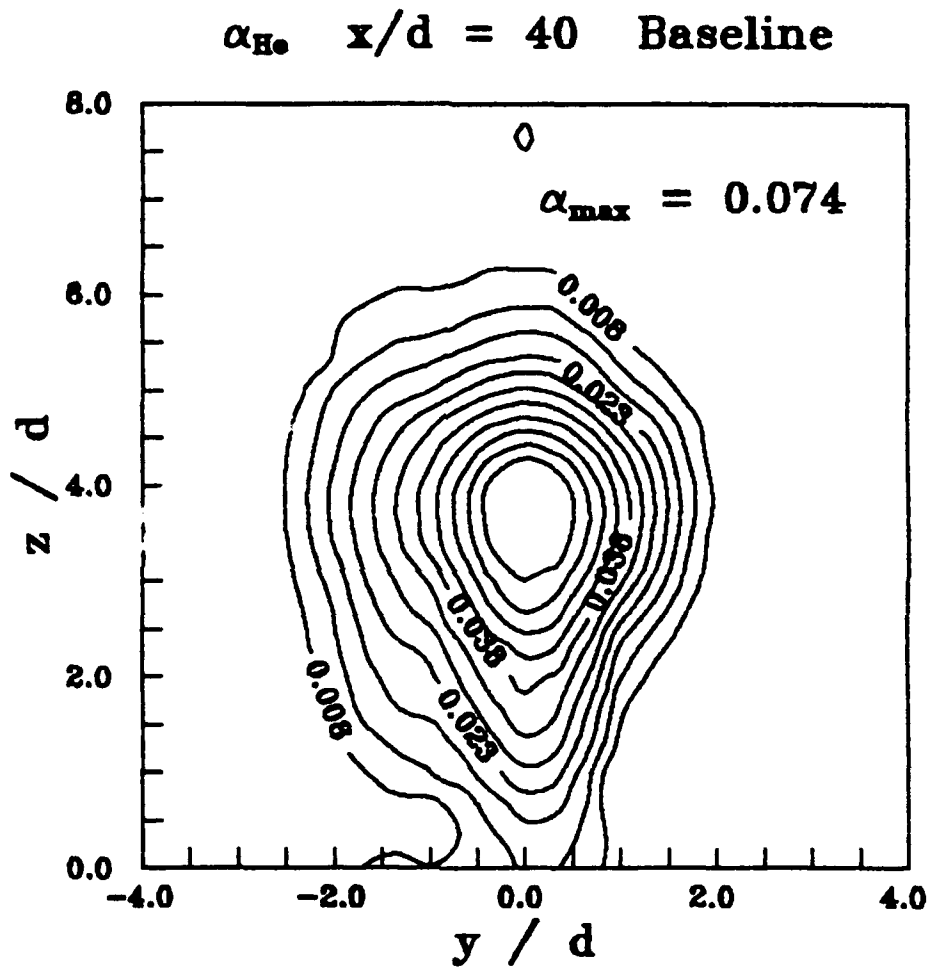


Figure 24. Helium Concentration, Baseline Injection,  $x/d = 40$

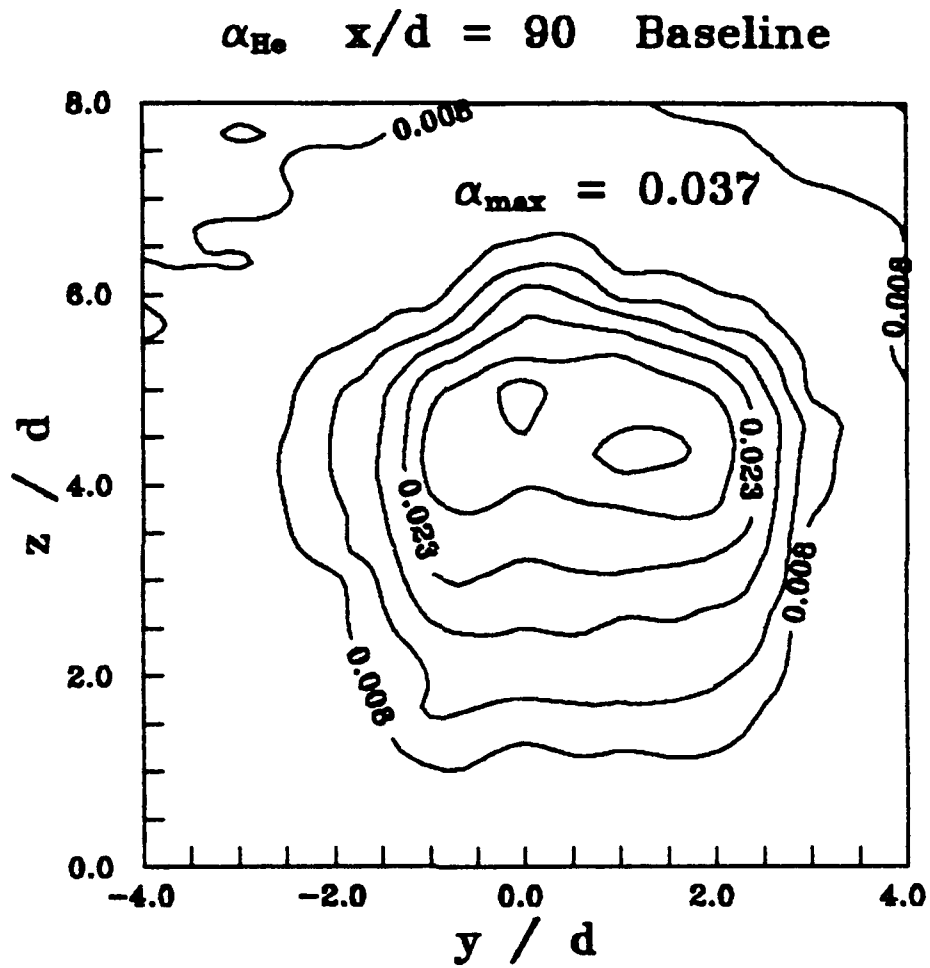


Figure 25. Helium Concentration, Baseline Injection,  $x/d = 90$

$\alpha_{He}$   $x/d = 20$   $d_j = 0.159$  cm.

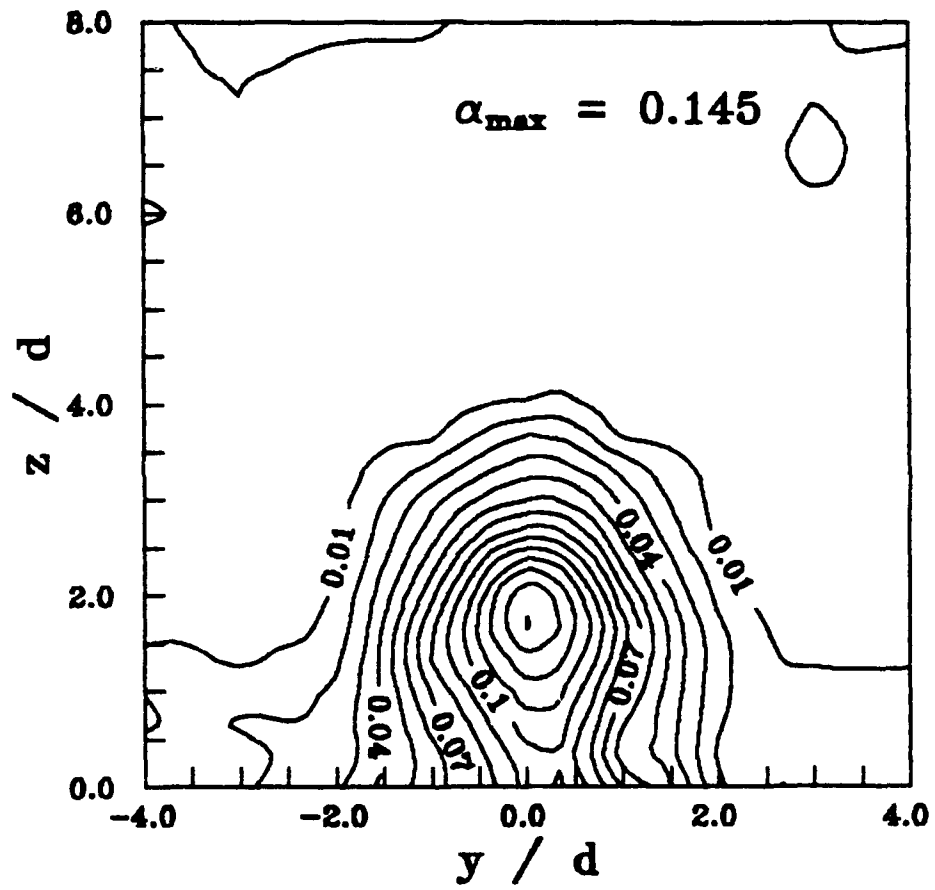


Figure 26. Helium Concentration, Combined Injection,  $x/d = 20$

$\alpha_{\text{He}}$   $x/d = 40$   $d_j = 0.159$  cm.

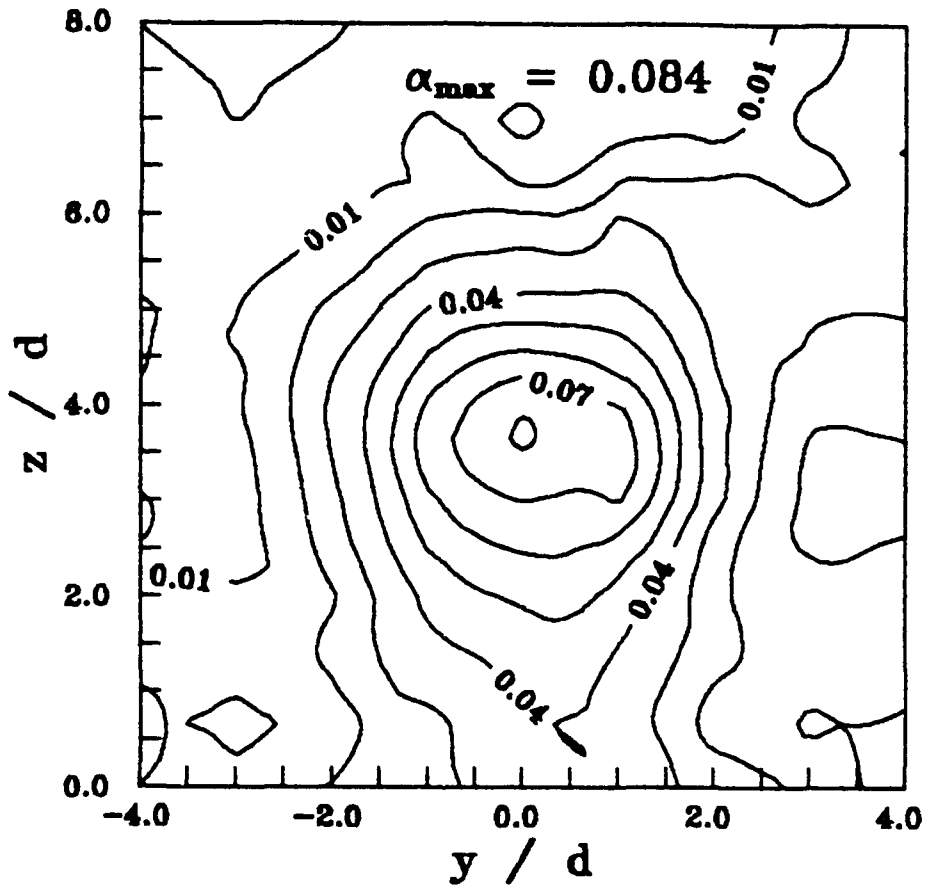


Figure 27. Helium Concentration, Combined Injection,  $x/d = 40$



$\alpha_{\text{He}}$   $x/d = 90$   $d_j = 0.159$  cm.

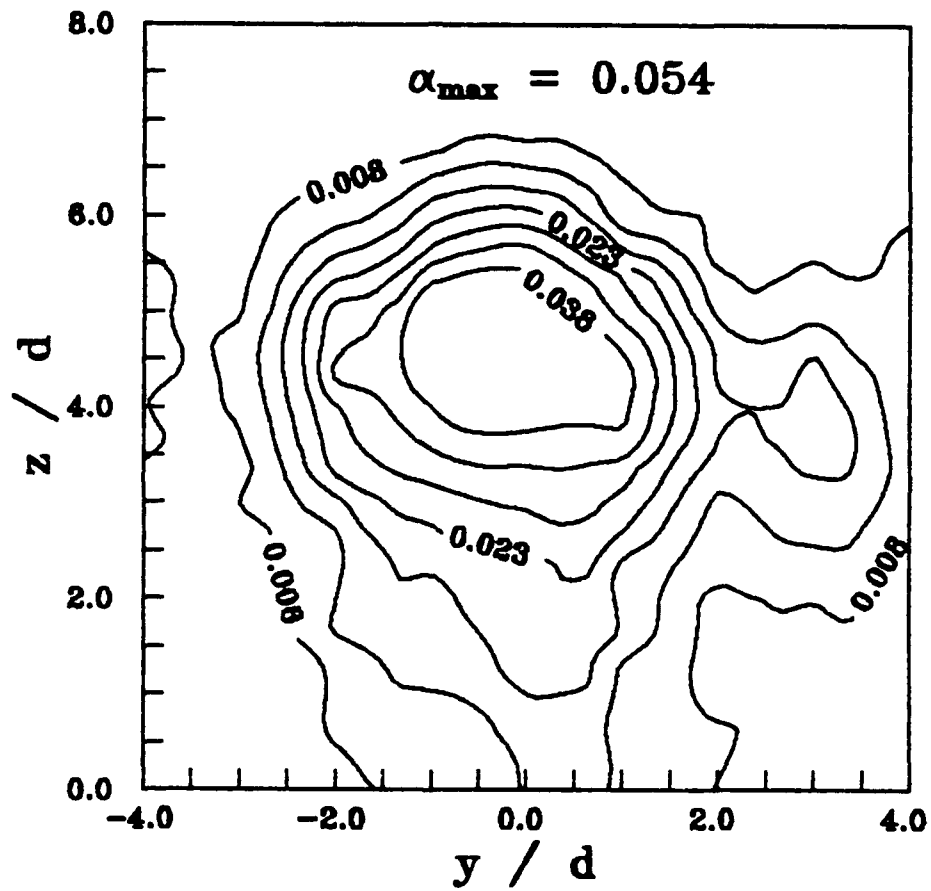


Figure 28. Helium Concentration, Combined Injection,  $x/d = 90$

$\alpha_{\text{He}}$   $x/d = 20$   $d_j = 0.079$  cm.

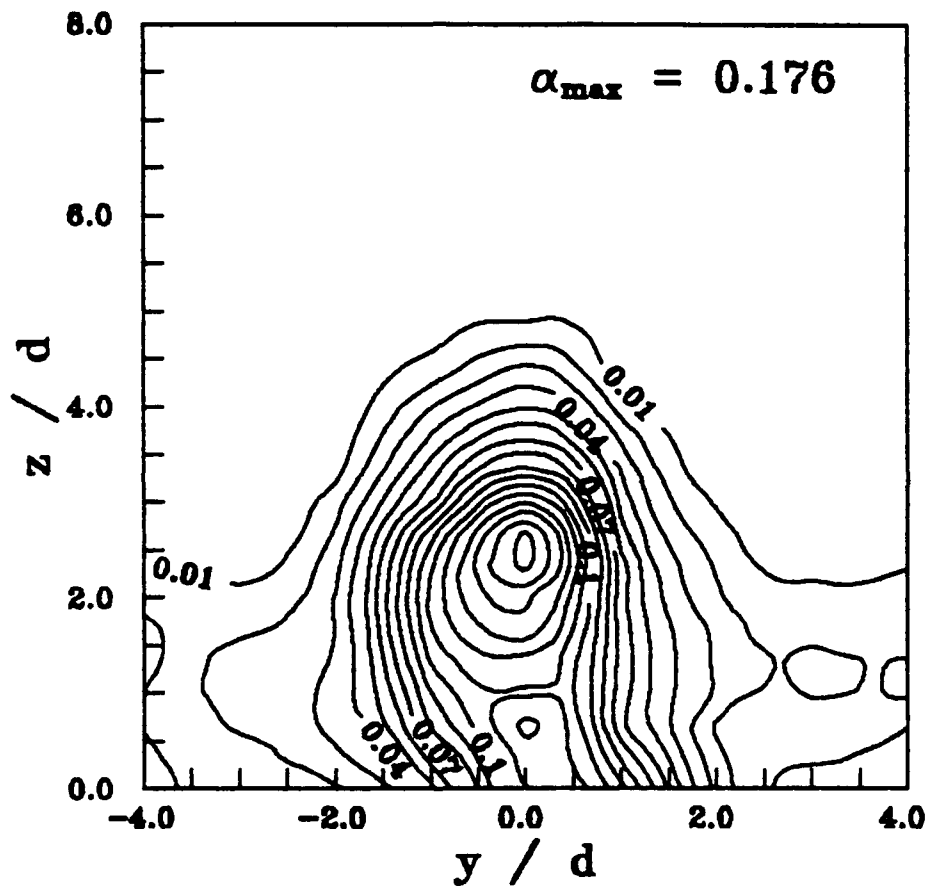


Figure 29. Helium Concentration, Combined Injection,  $x/d = 20$

$\alpha_{\text{He}}$   $x/d = 40$   $d_j = 0.079$  cm.

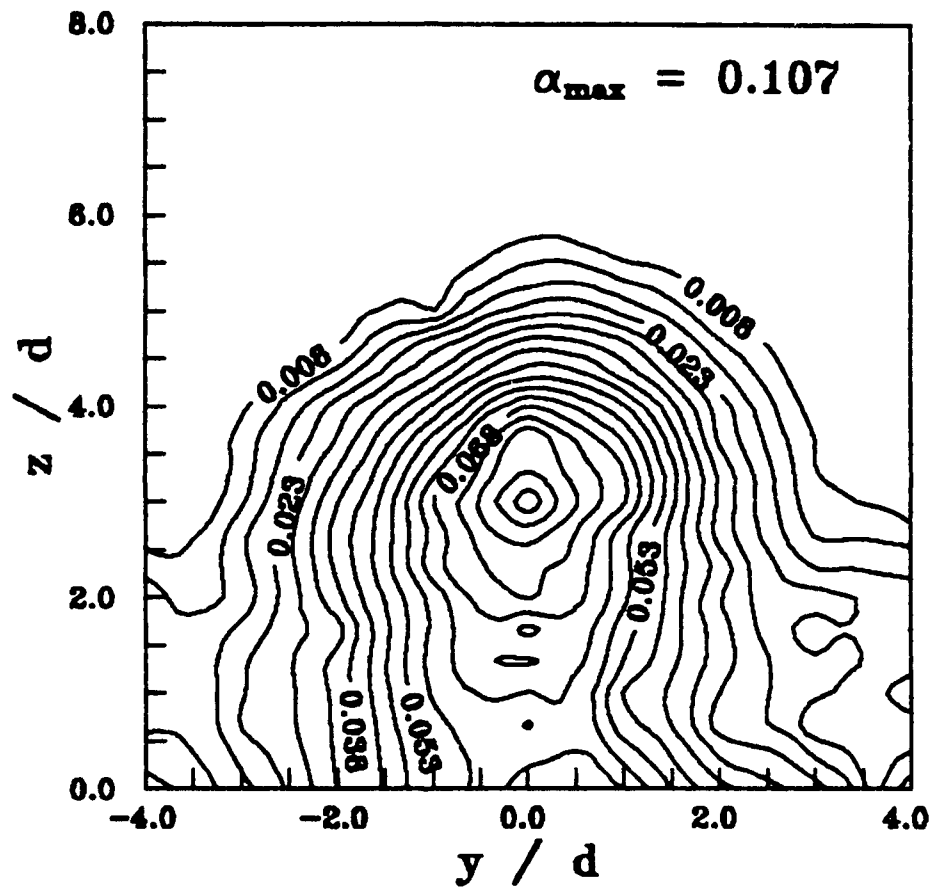


Figure 30. Helium Concentration, Combined Injection,  $x/d = 40$

$\alpha_{\text{He}}$   $x/d = 90$   $d_j = 0.079$  cm.

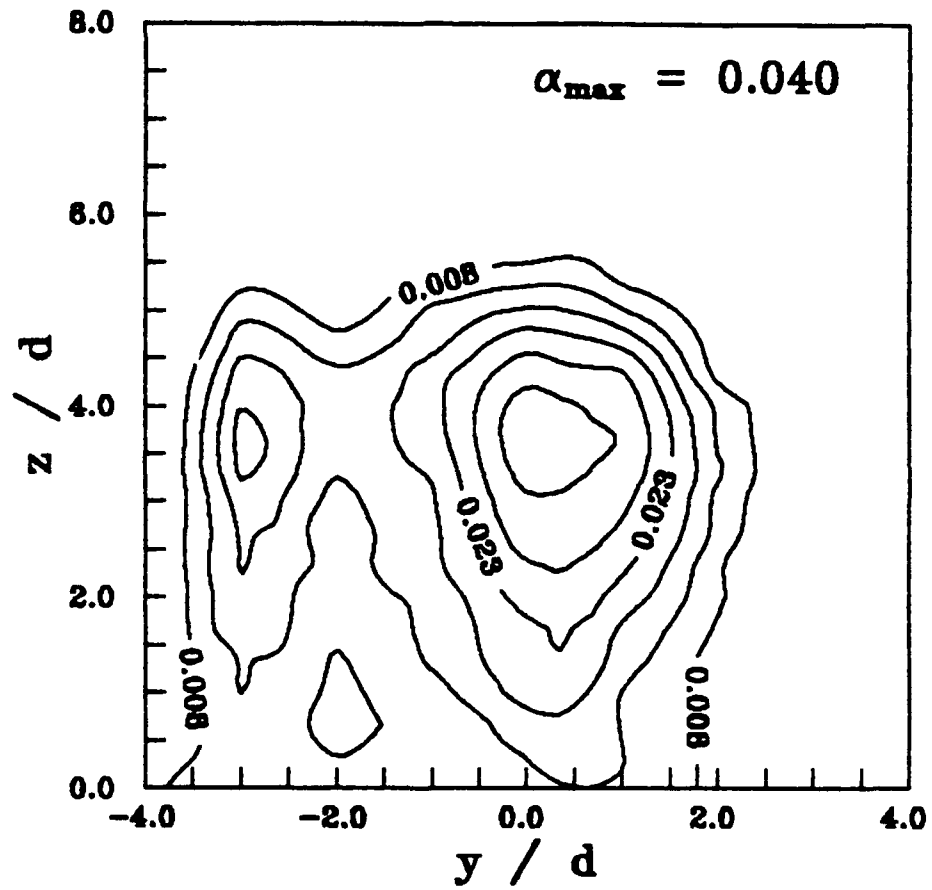


Figure 31. Helium Concentration, Combined Injection,  $x/d = 90$

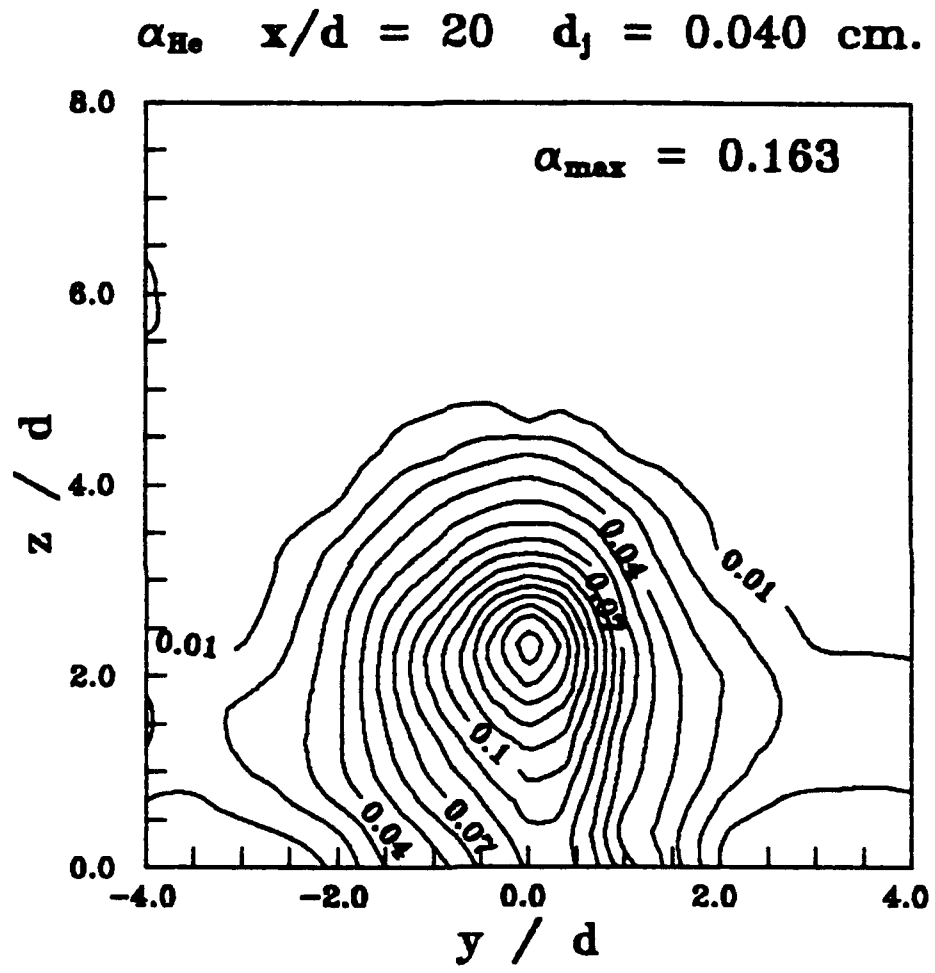


Figure 32. Helium Concentration, Combined Injection,  $x/d = 20$

$\alpha_{\text{He}}$   $x/d = 40$   $d_j = 0.040$  cm.

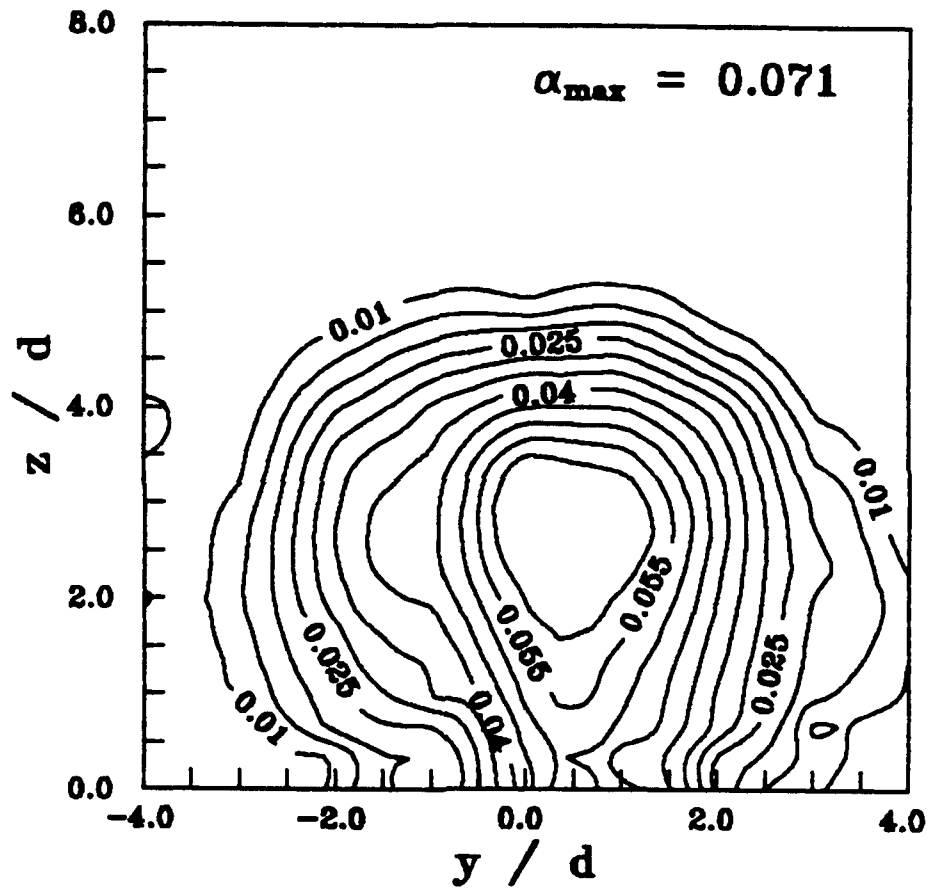


Figure 33. Helium Concentration, Combined Injection,  $x/d = 40$

$\alpha_{\text{He}}$   $x/d = 90$   $d_j = 0.040$  cm.

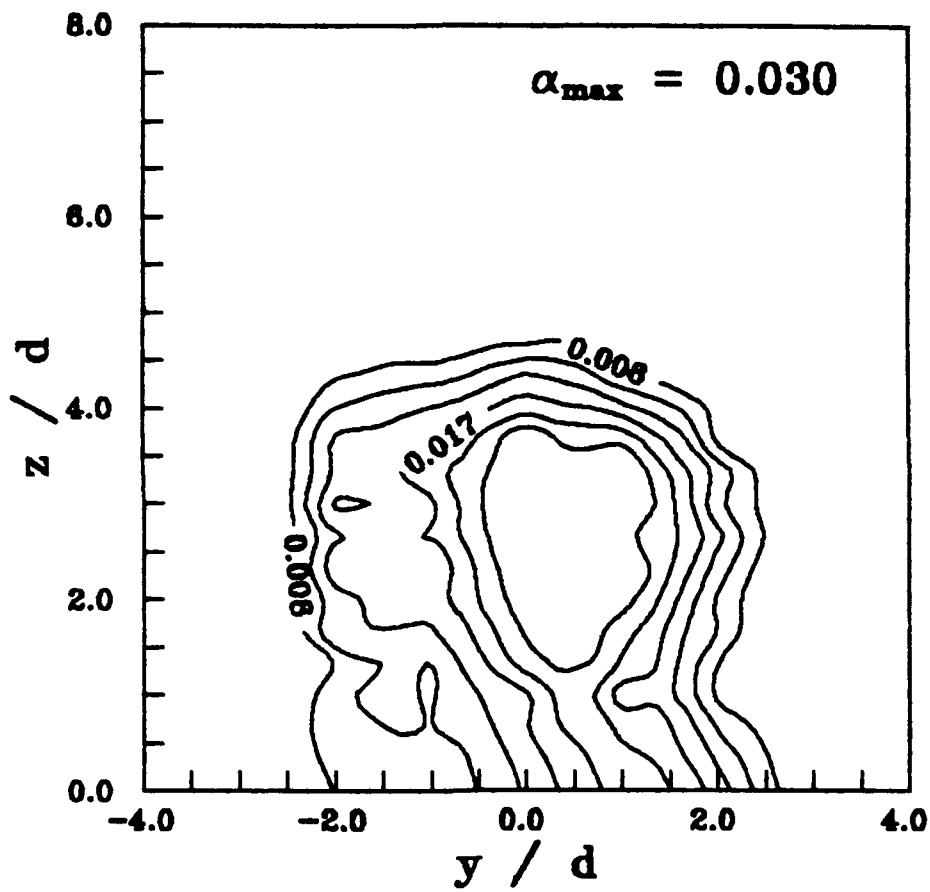
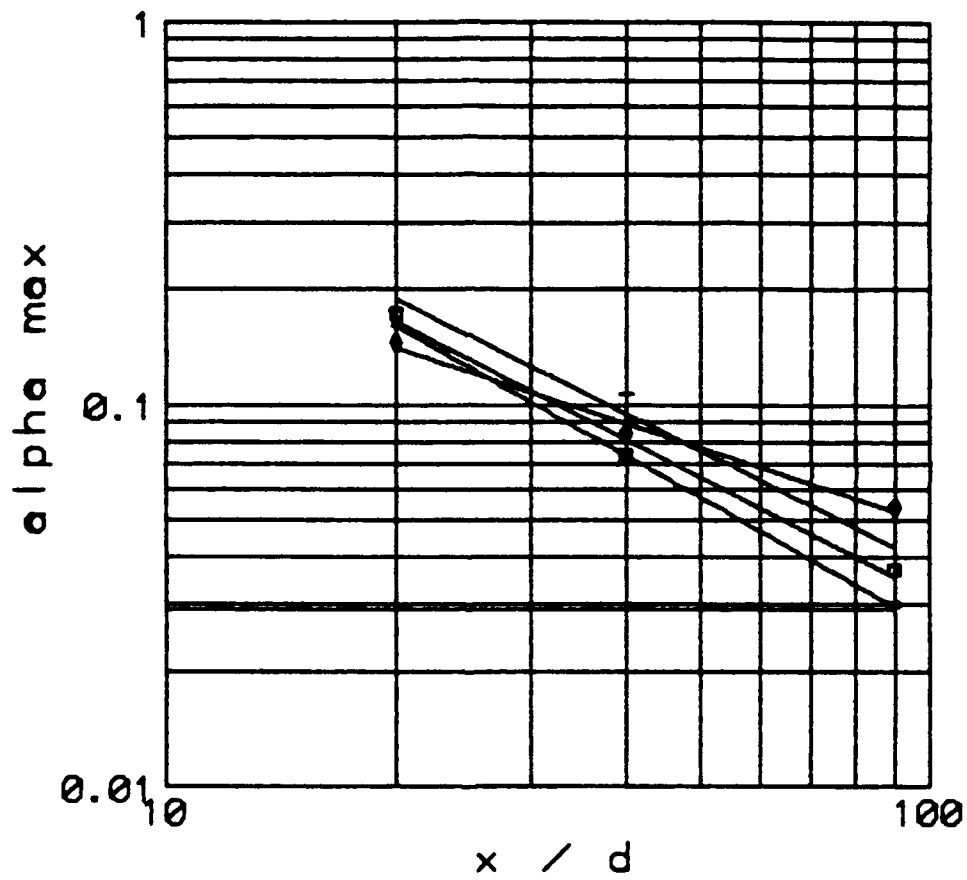


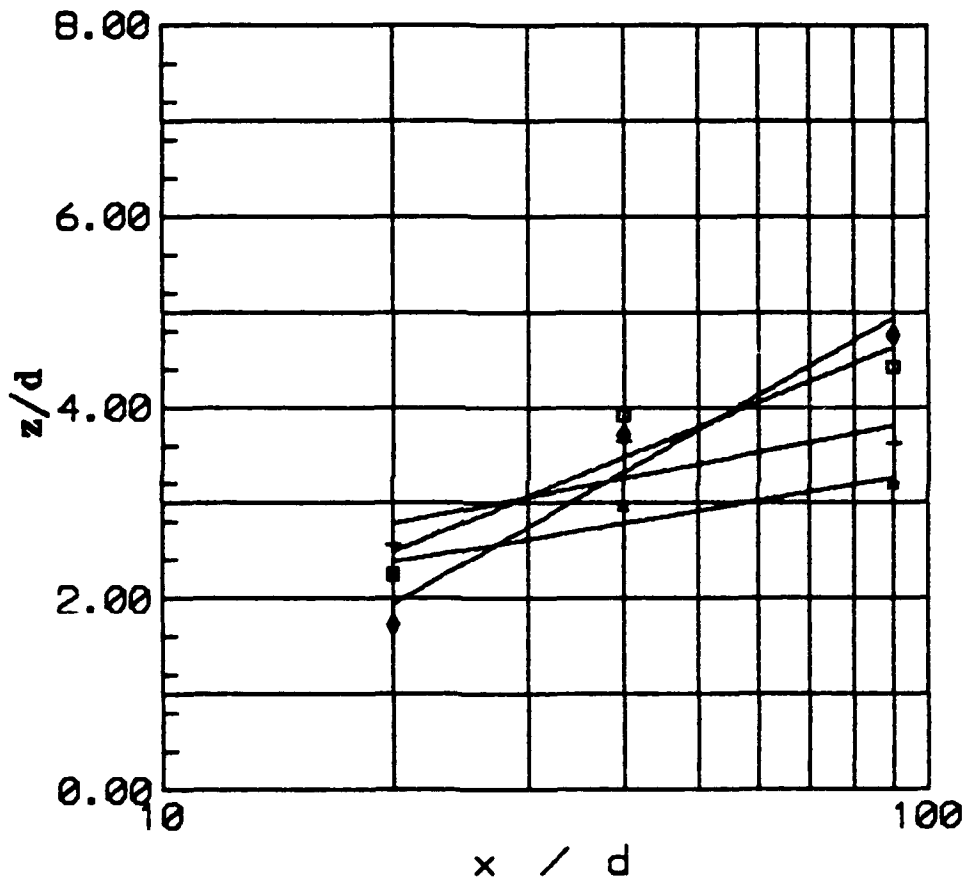
Figure 34. Helium Concentration, Combined Injection,  $x/d = 90$



□□□□ Baseline  
 ○○○○  $d_j = 0.159$  cm  
 +++++  $d_j = 0.079$  cm  
 \*\*\*\*\*  $d_j = 0.040$  cm

Figure 35. Helium Concentration Decay





□□□□□ Baseline  
 ○○○○○ d<sub>j</sub> = 0.159 cm  
 +++++ d<sub>j</sub> = 0.079 cm  
 \*\*\*\*\* d<sub>j</sub> = 0.040 cm

Figure 36. Core Penetration

$P_{t1}/P_{t\infty}$   $x/d = 20$  Baseline

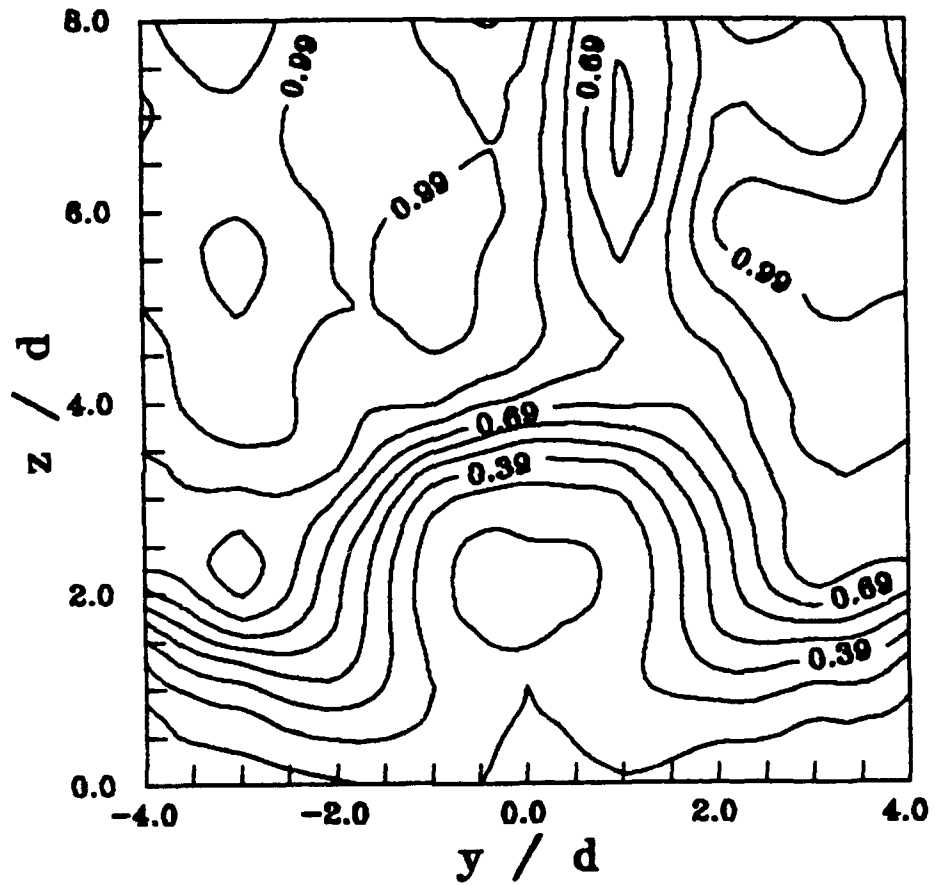


Figure 37. Total Pressure Contours, Baseline Injection,  $x/d = 20$

$P_{t1}/P_{t\infty}$   $x/d = 20$   $d_j = 0.159$  cm.

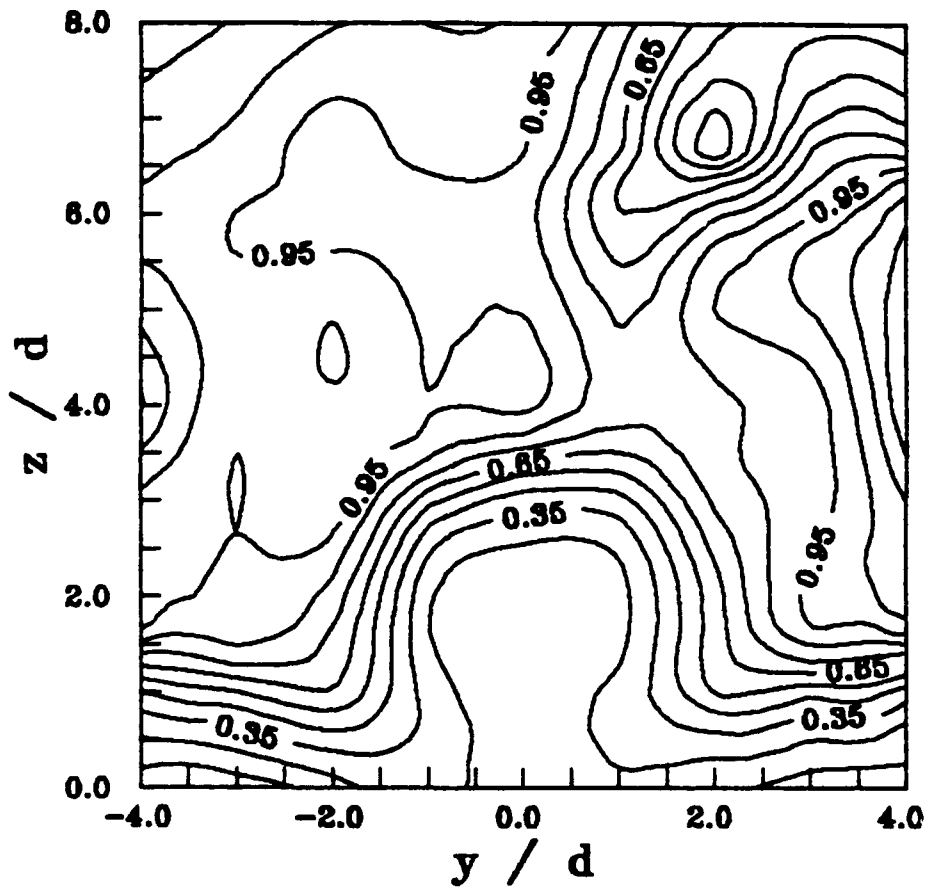


Figure 38. Total Pressure Contours, Combined Injection,  $x/d = 20$

$P_{t1}/P_{t\infty}$   $x/d = 20$   $d_j = 0.079$  cm.

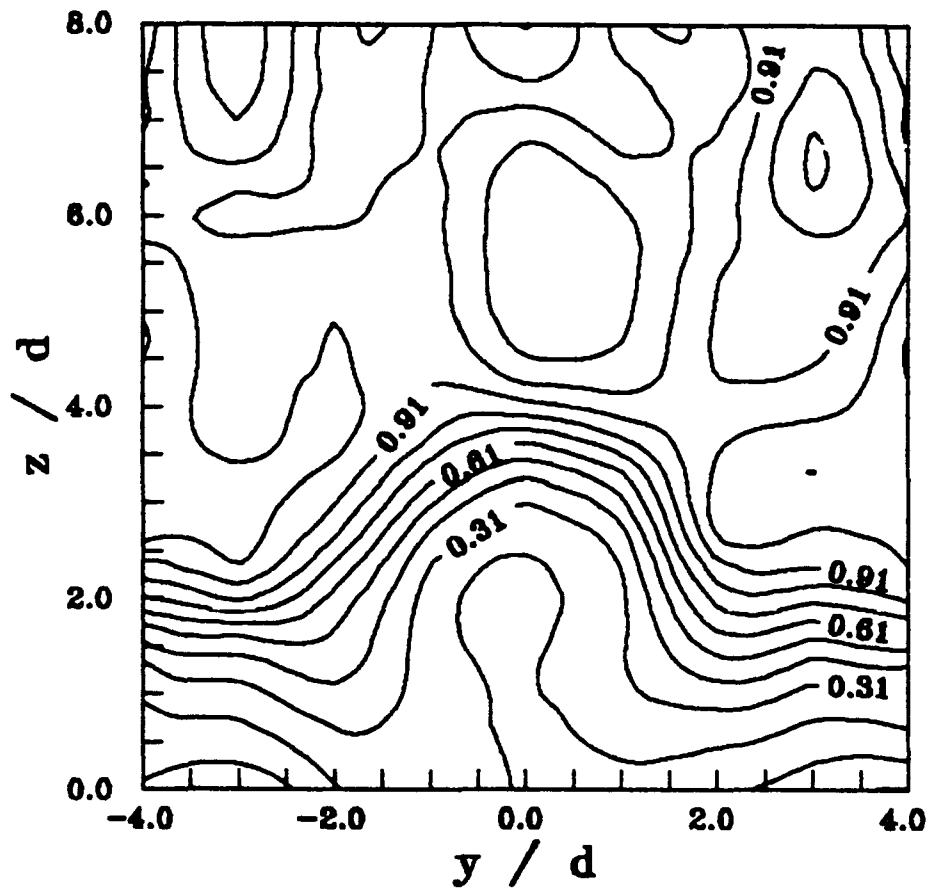


Figure 39. Total Pressure Contours, Combined Injection,  $x/d = 20$

$P_{t1}/P_{t\infty}$   $x/d = 20$   $d_j = 0.040$  cm.

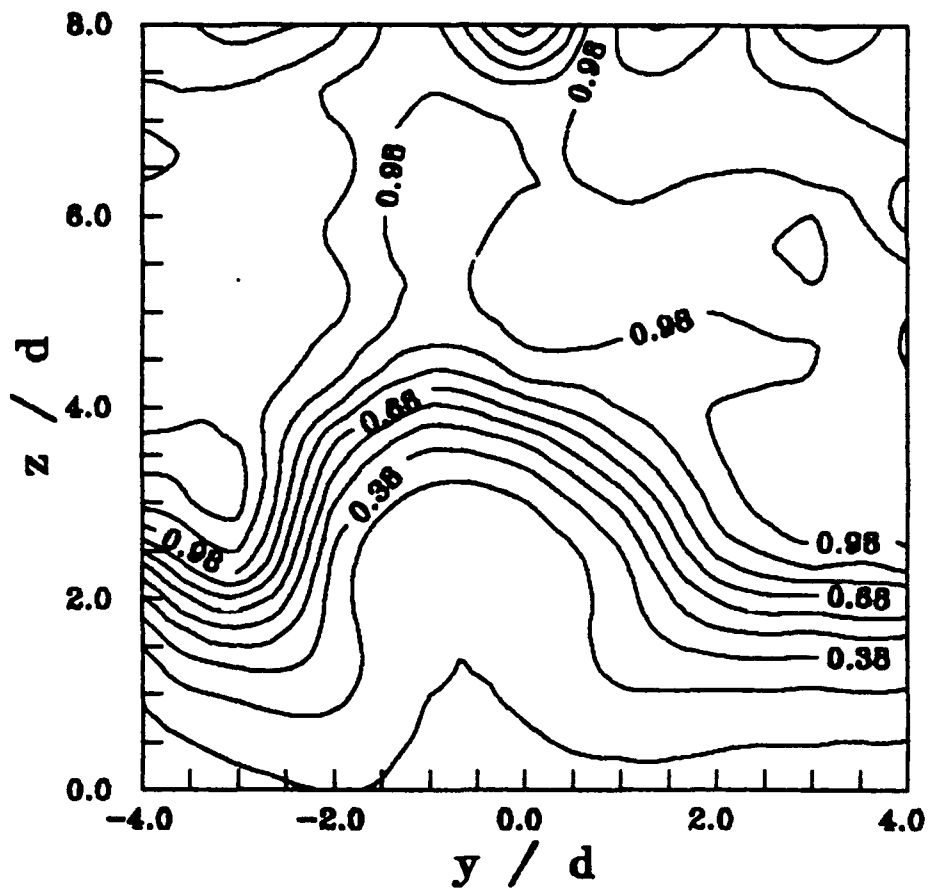


Figure 40. Total Pressure Contours, Combined Injection,  $x/d = 20$

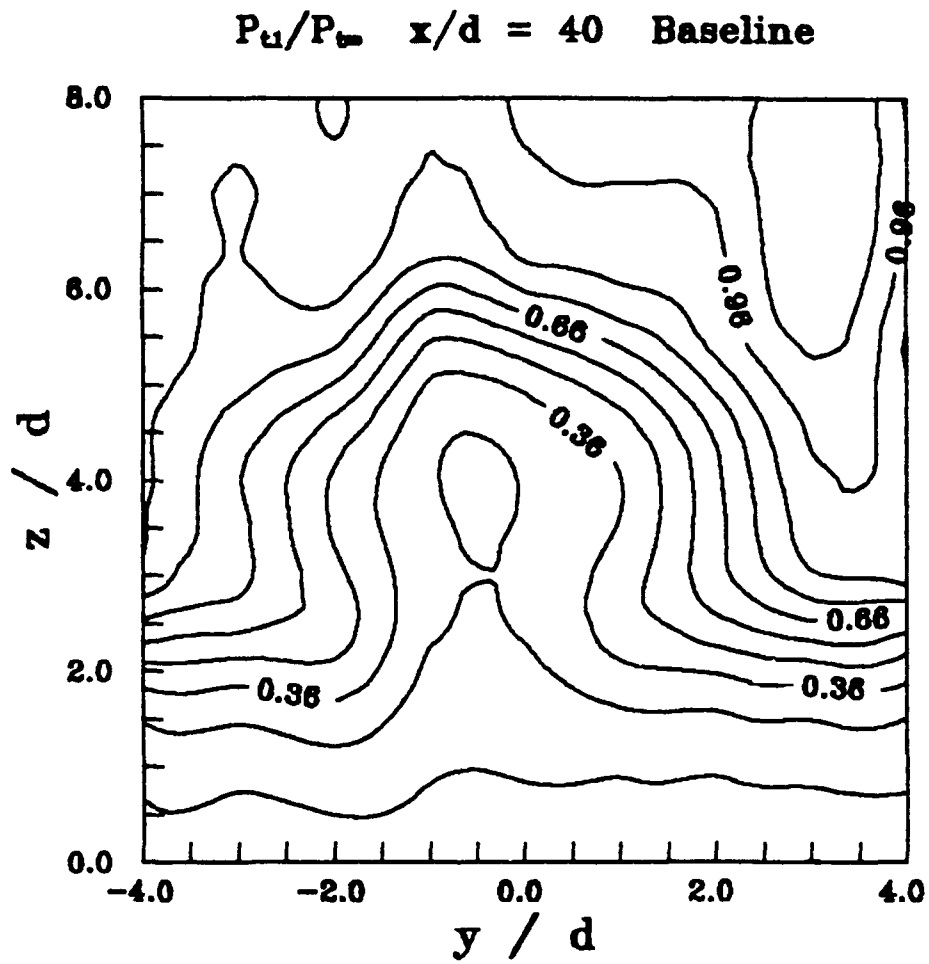


Figure 41. Total Pressure Contours, Baseline Injection,  $x/d = 40$

$P_{t1}/P_{t\infty}$   $x/d = 40$   $d_j = 0.159$  cm.

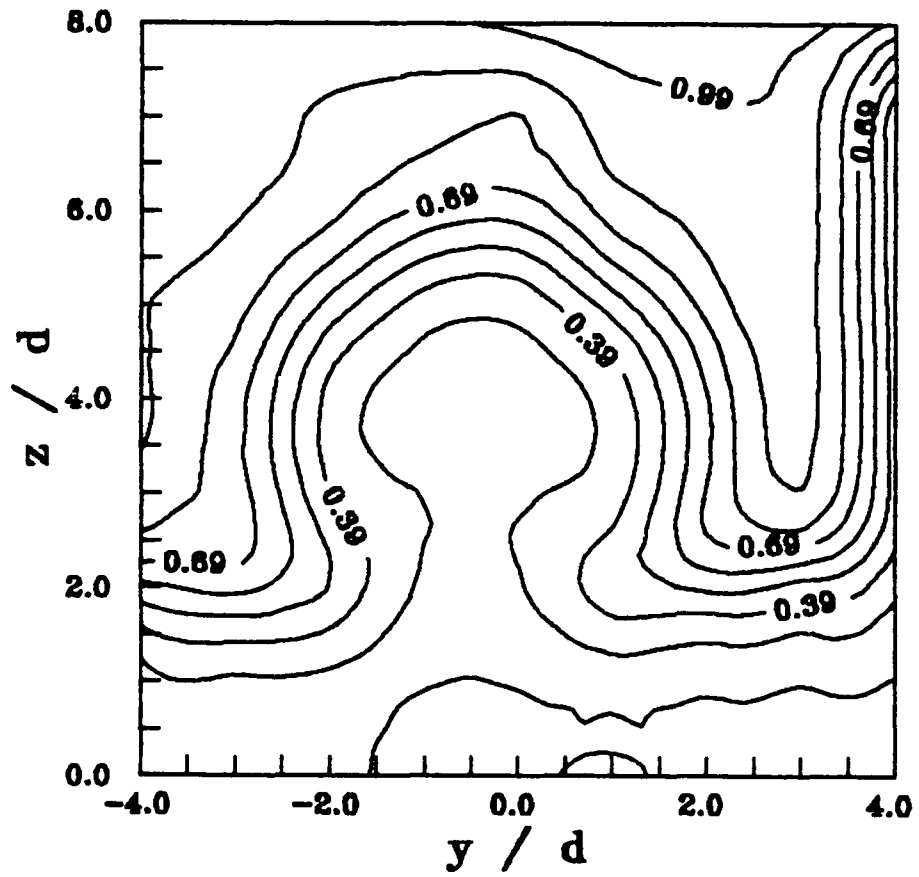


Figure 42. Total Pressure Contours, Combined Injection,  $x/d = 40$

$P_{t1}/P_{t\infty}$   $x/d = 40$   $d_j = 0.079$  cm.

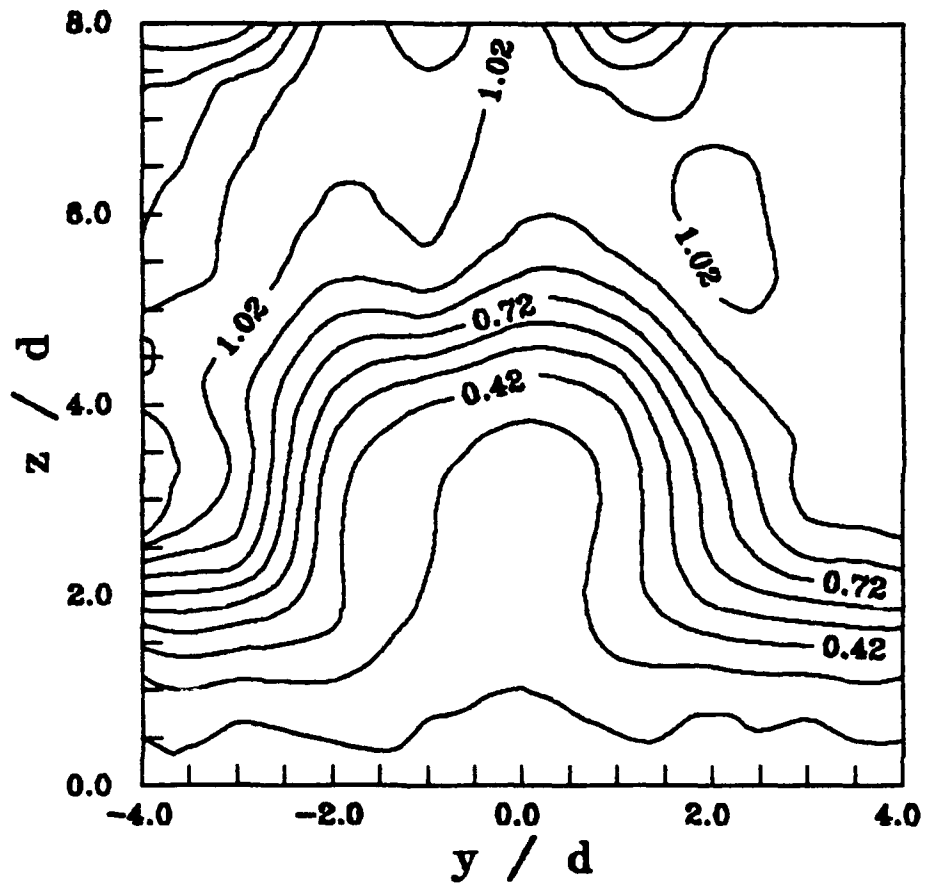


Figure 43. Total Pressure Contours, Combined Injection,  $x/d = 40$



$P_{t1}/P_{t\infty}$   $x/d = 40$   $d_j = 0.040$  cm.

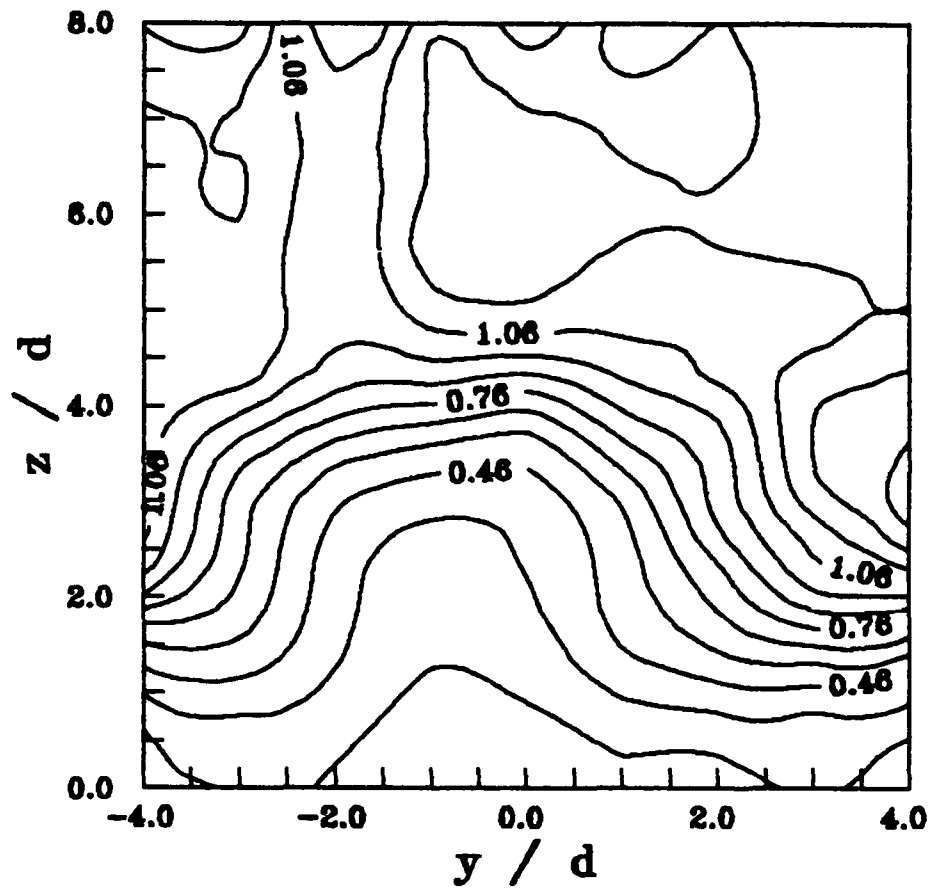


Figure 44. Total Pressure Contours, Combined Injection,  $x/d = 40$

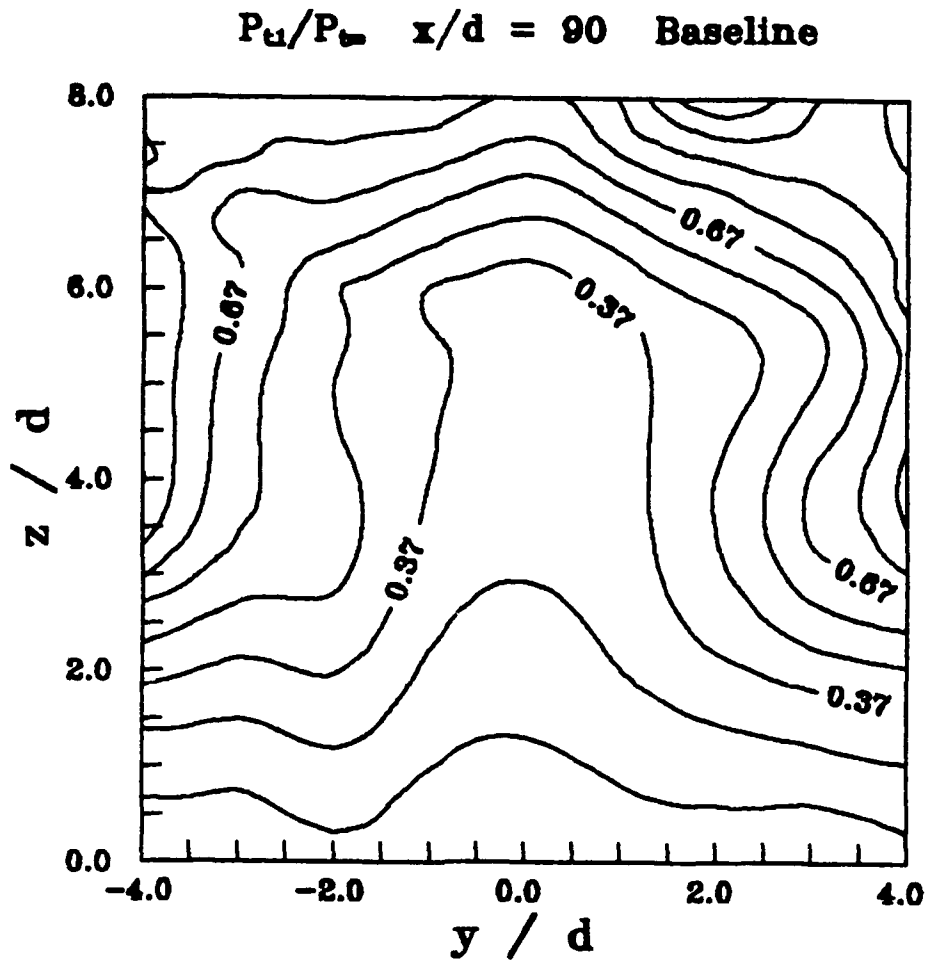


Figure 45. Total Pressure Contours, Baseline Injection,  $x/d = 90$

$P_{t1}/P_{t\infty}$   $x/d = 90$   $d_j = 0.159$  cm.

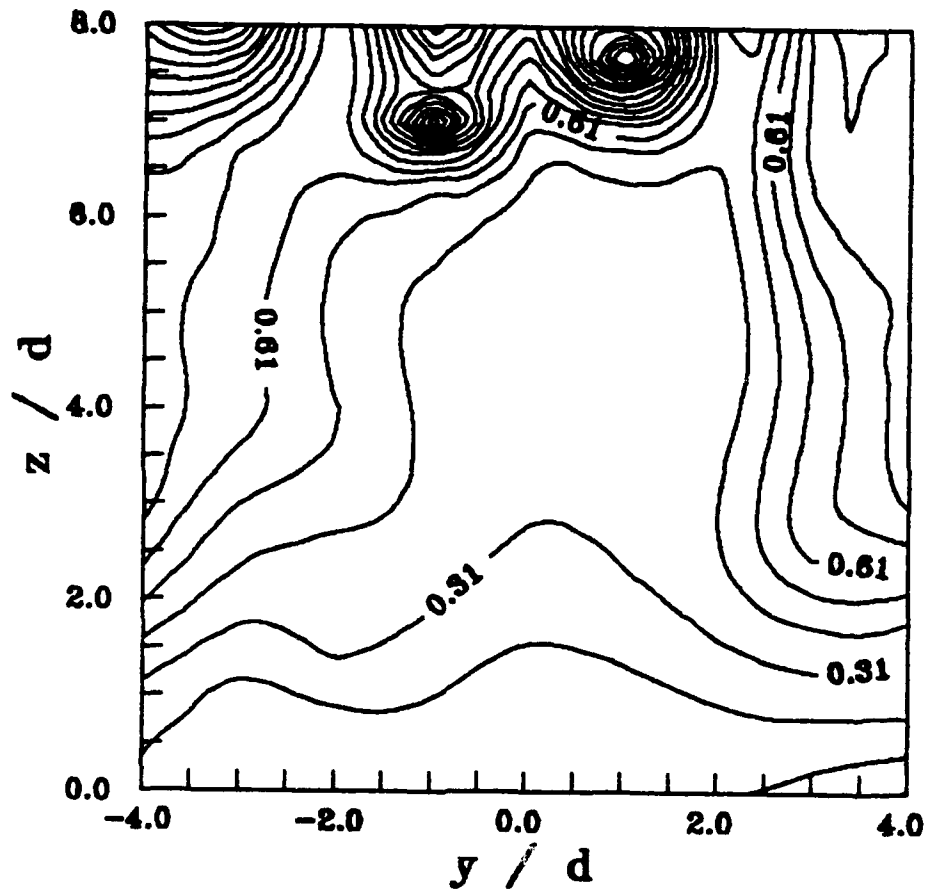


Figure 46. Total Pressure Contours, Combined Injection,  $x/d = 90$

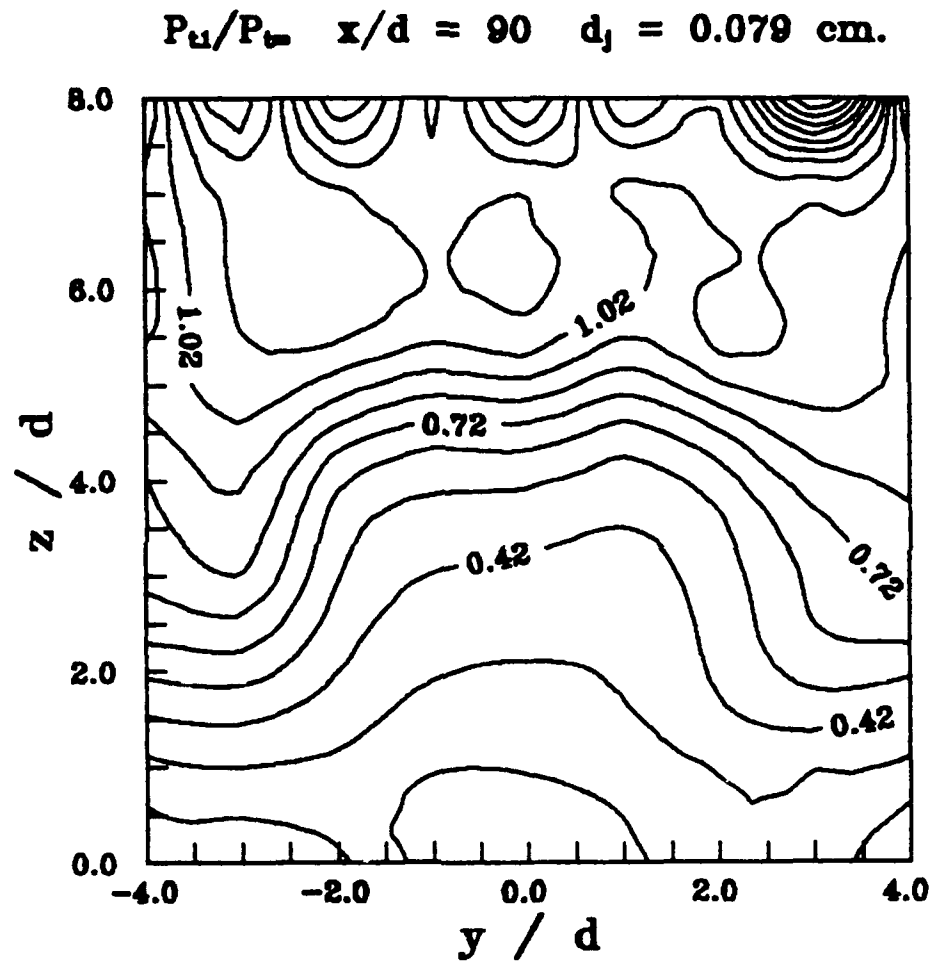


Figure 47. Total Pressure Contours, Combined Injection,  $x/d = 90$

$P_{t1}/P_{t\infty}$   $x/d = 90$   $d_j = 0.040$  cm.

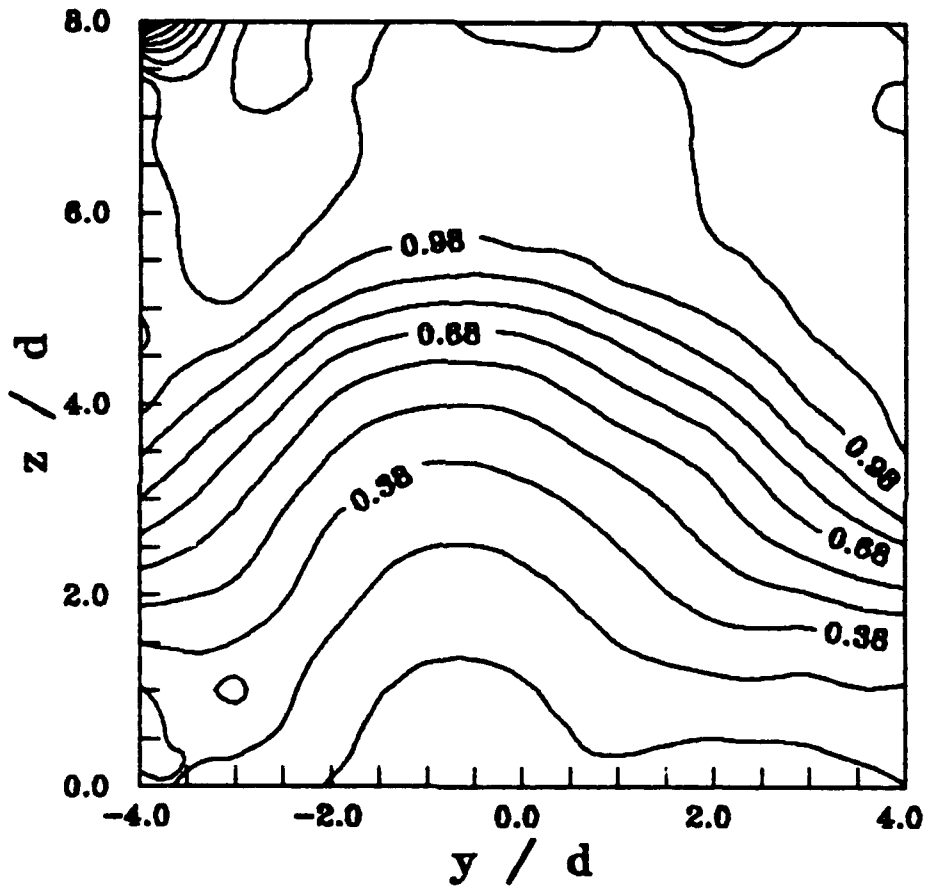


Figure 48. Total Pressure Contours, Combined Injection,  $x/d = 90$

$M_1$   $x/d = 20$  Baseline

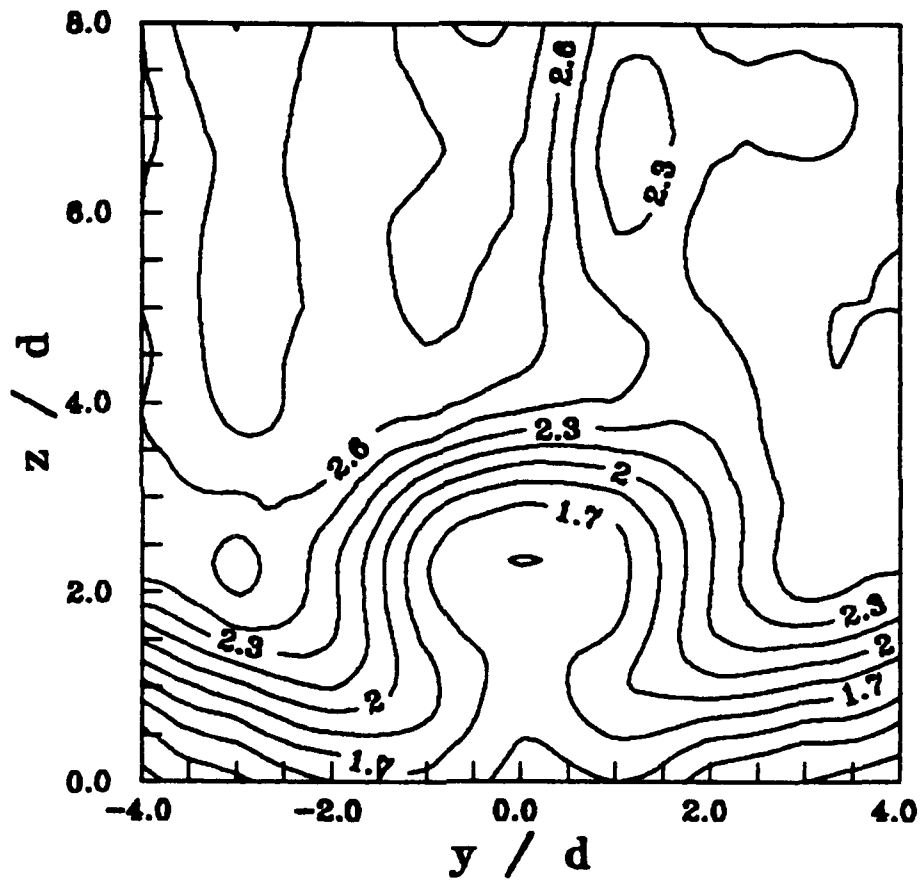


Figure 49. Mach Number Contours, Baseline Injection,  $x/d = 20$

$M_1$   $x/d = 20$   $d_j = 0.159$  cm.

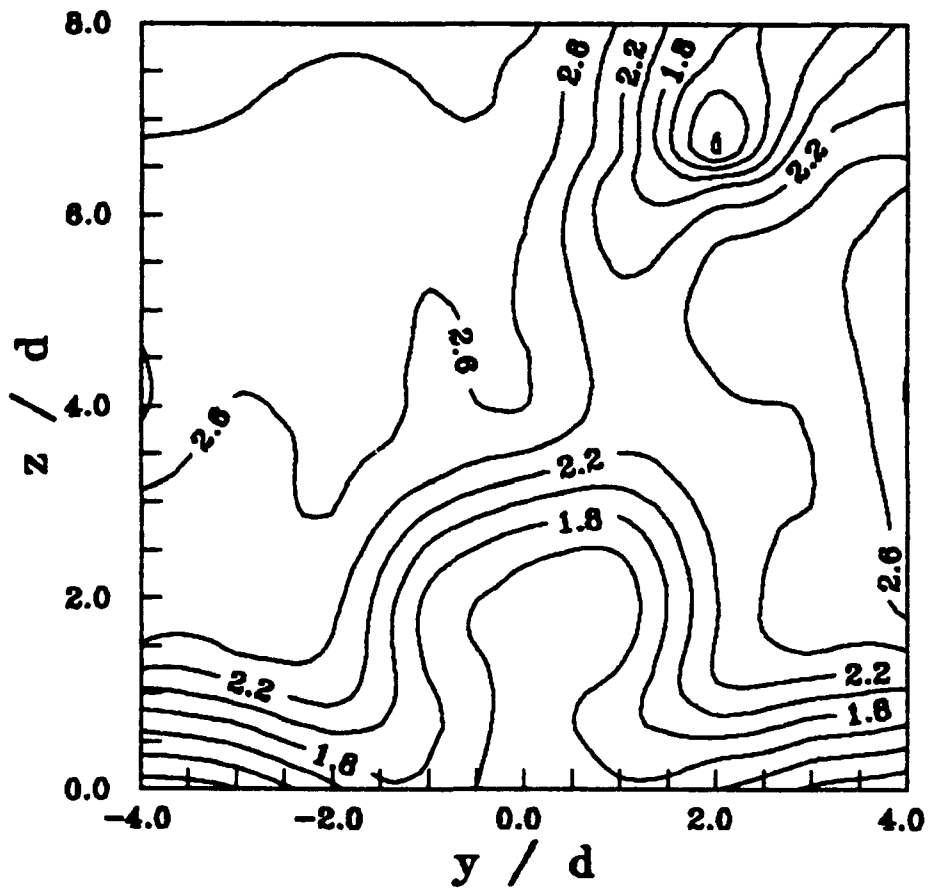


Figure 50. Mach Number Contours, Combined Injection,  $x/d = 20$

$M_1$   $x/d = 20$   $d_j = 0.079$  cm.

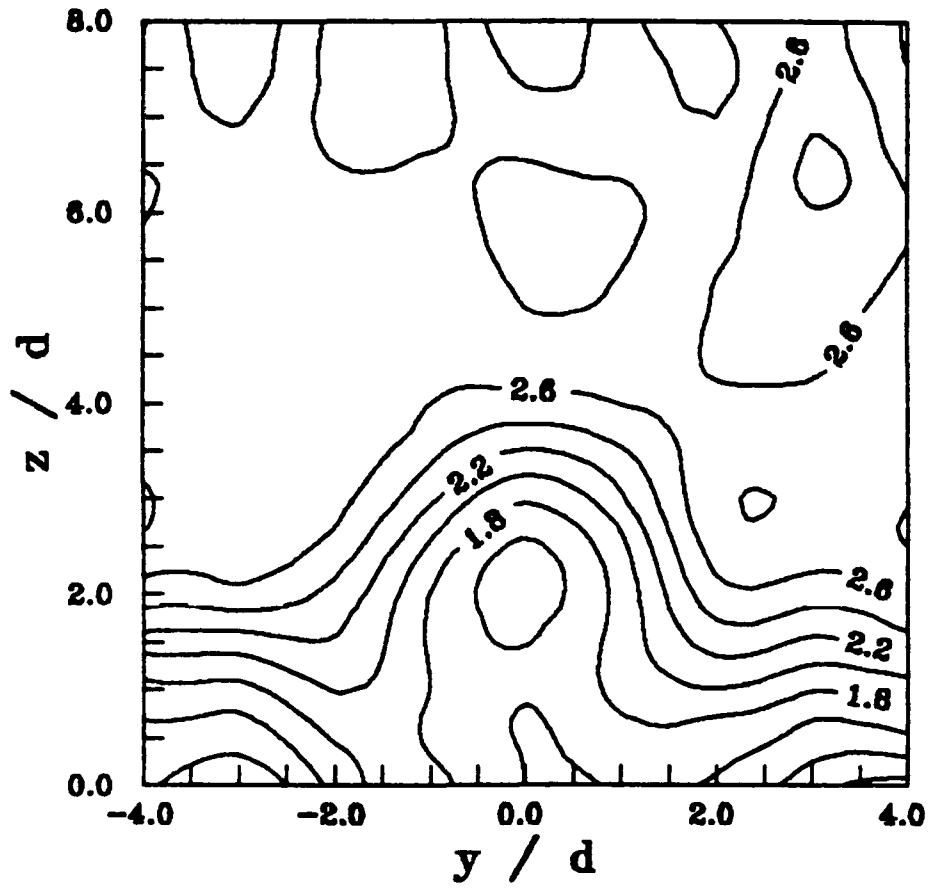


Figure 51. Mach Number Contours, Combined Injection,  $x/d = 20$



$M_1$   $x/d = 20$   $d_j = 0.040$  cm.

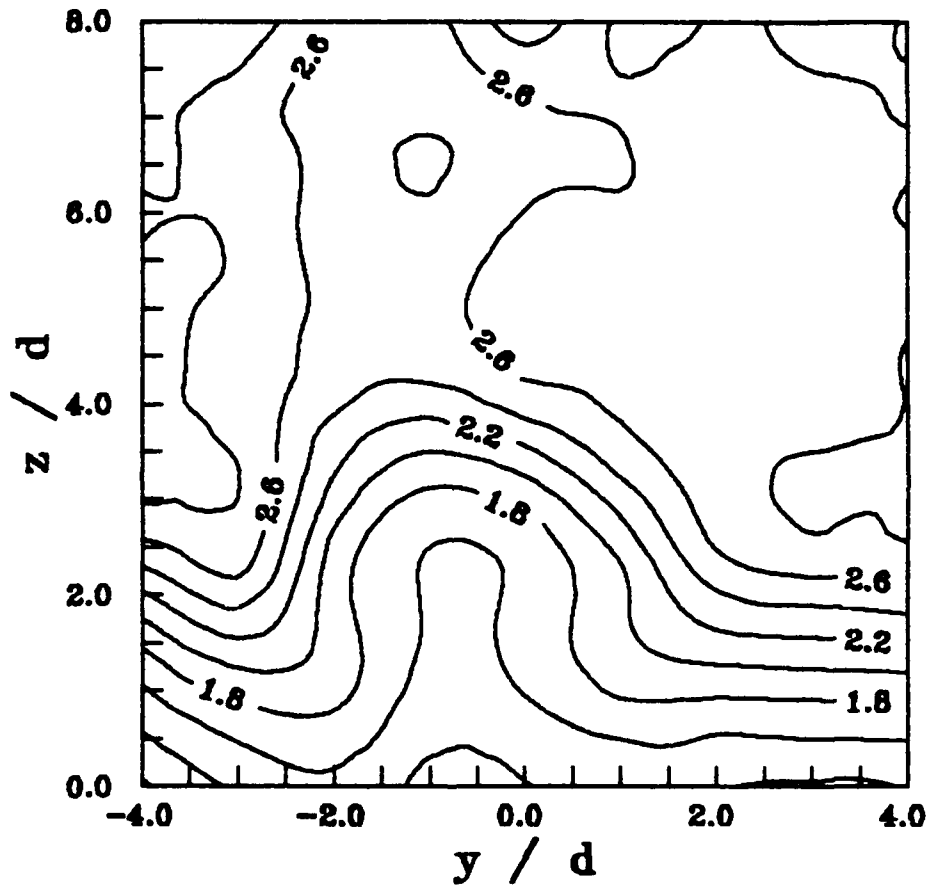


Figure 52. Mach Number Contours, Combined Injection,  $x/d = 20$

$U_1/U_\infty$   $x/d = 20$   $d_j = 0.079$  cm.

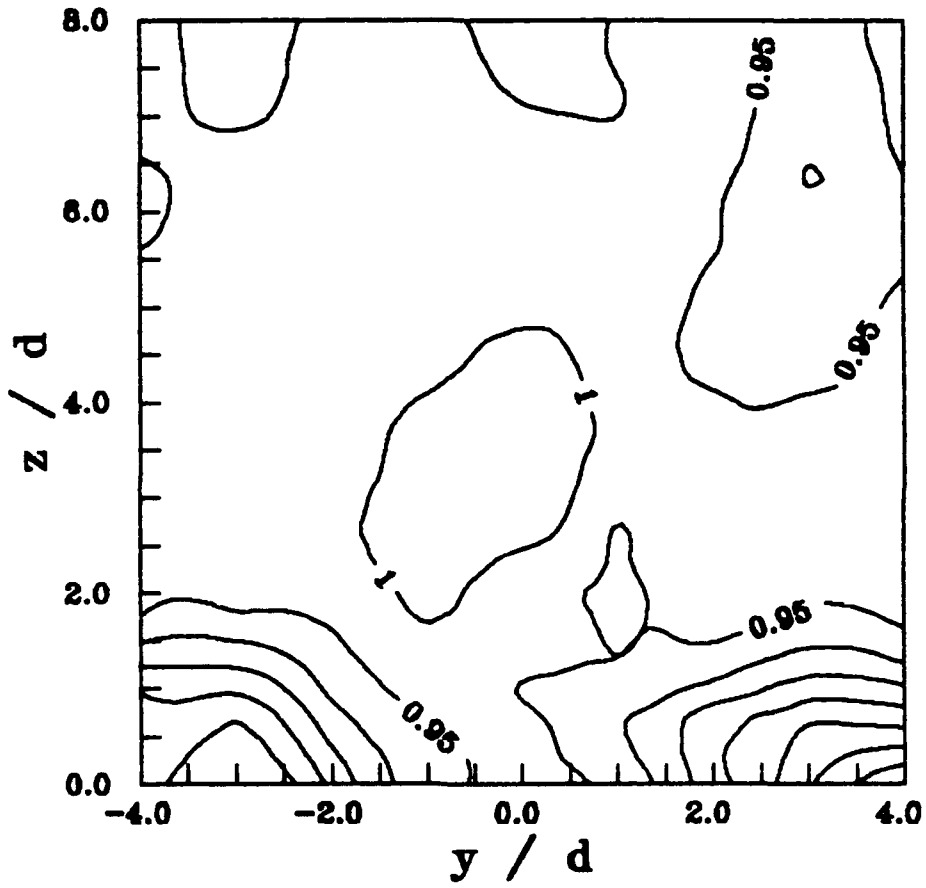


Figure 53. Typical Velocity Contour, Combined Injection,  $x/d = 20$

$M_1$   $x/d = 90$  Baseline

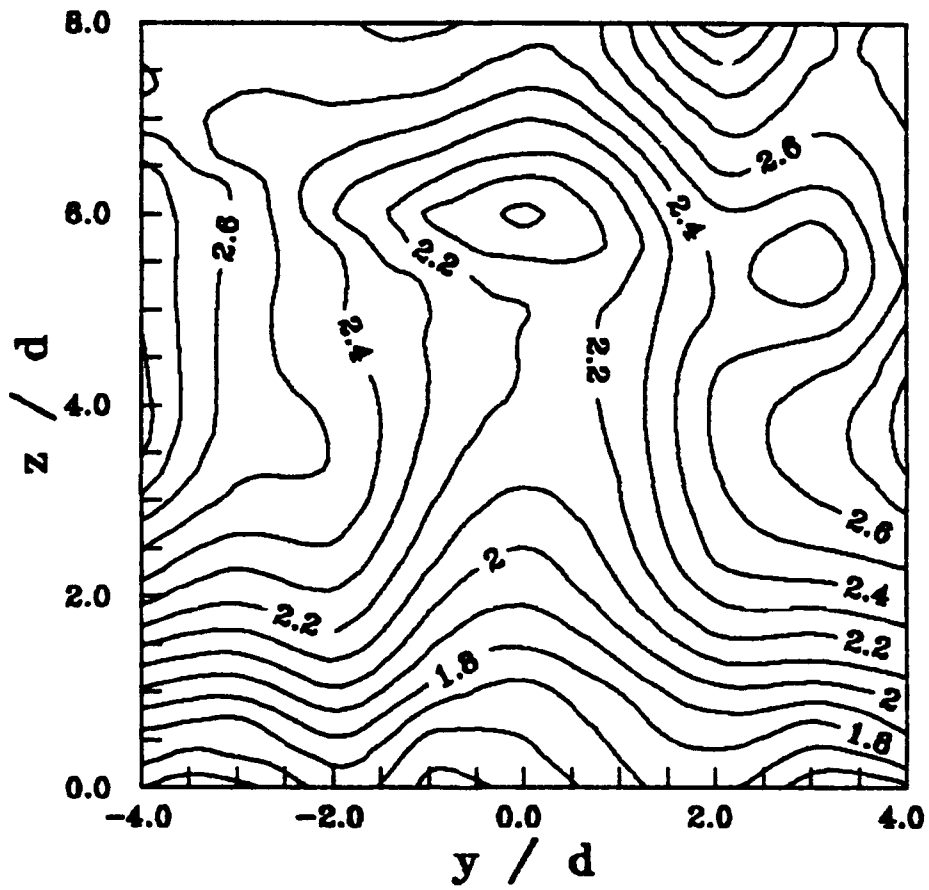


Figure 54. Mach Number Contours, Baseline Injection,  $x/d = 90$

$M_1$   $x/d = 90$   $d_j = 0.159$  cm.

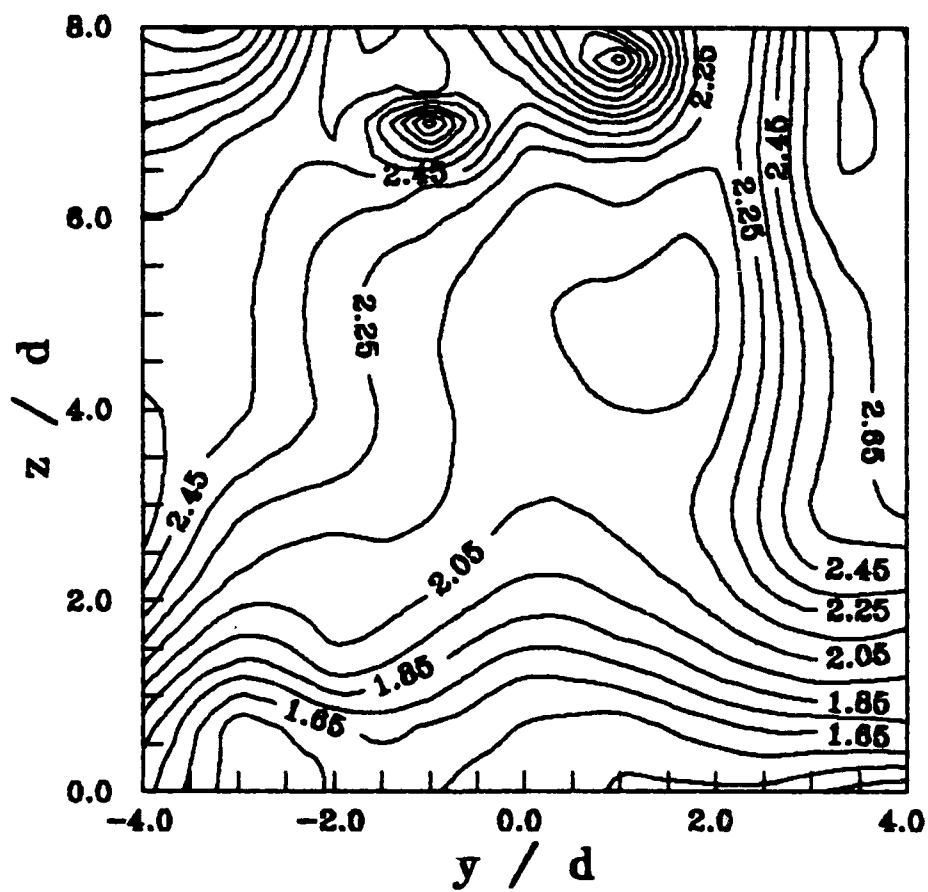


Figure 55. Mach Number Contours, Combined Injection,  $x/d = 90$

$M_1$   $x/d = 90$   $d_j = 0.079$  cm.

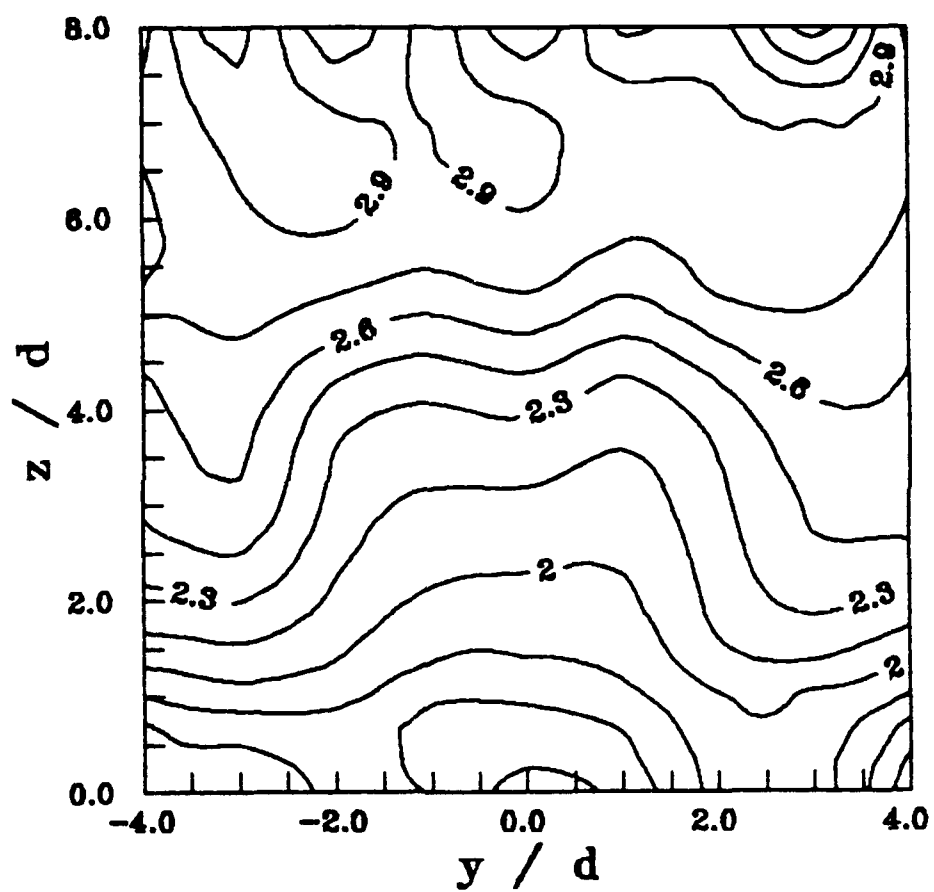


Figure 56. Mach Number Contours, Combined Injection,  $x/d = 90$

$M_1$   $x/d = 90$   $d_j = 0.040$  cm.

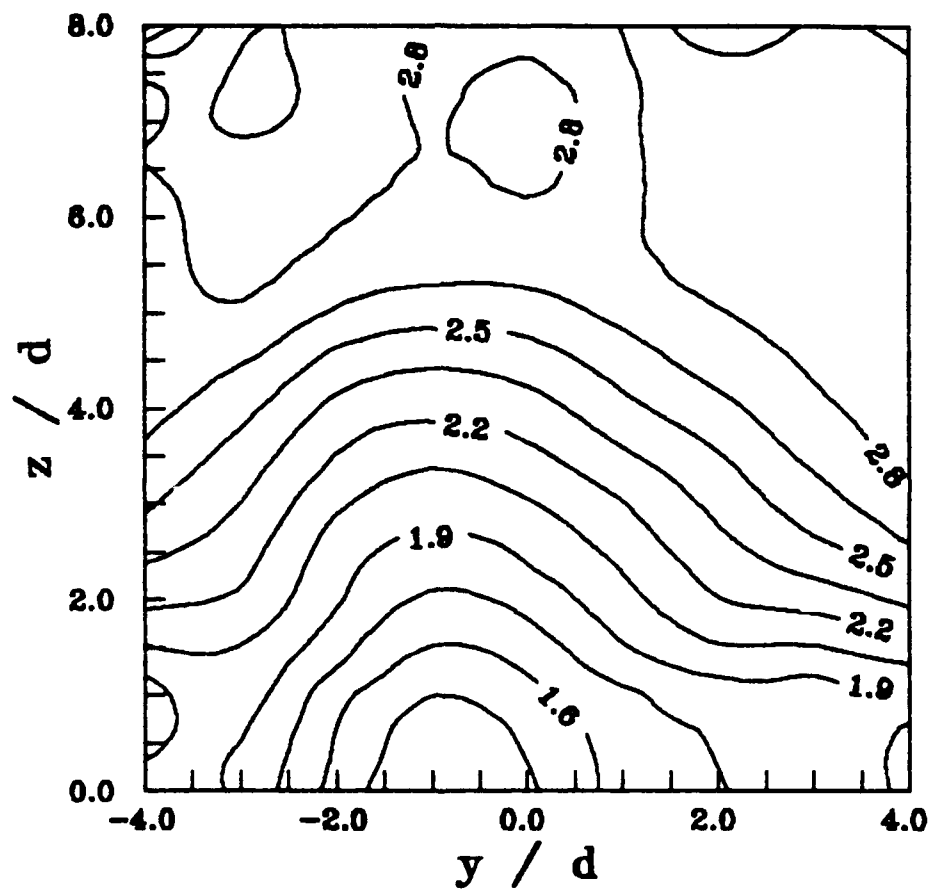


Figure 57. Mach Number Contours, Combined Injection,  $x/d = 90$

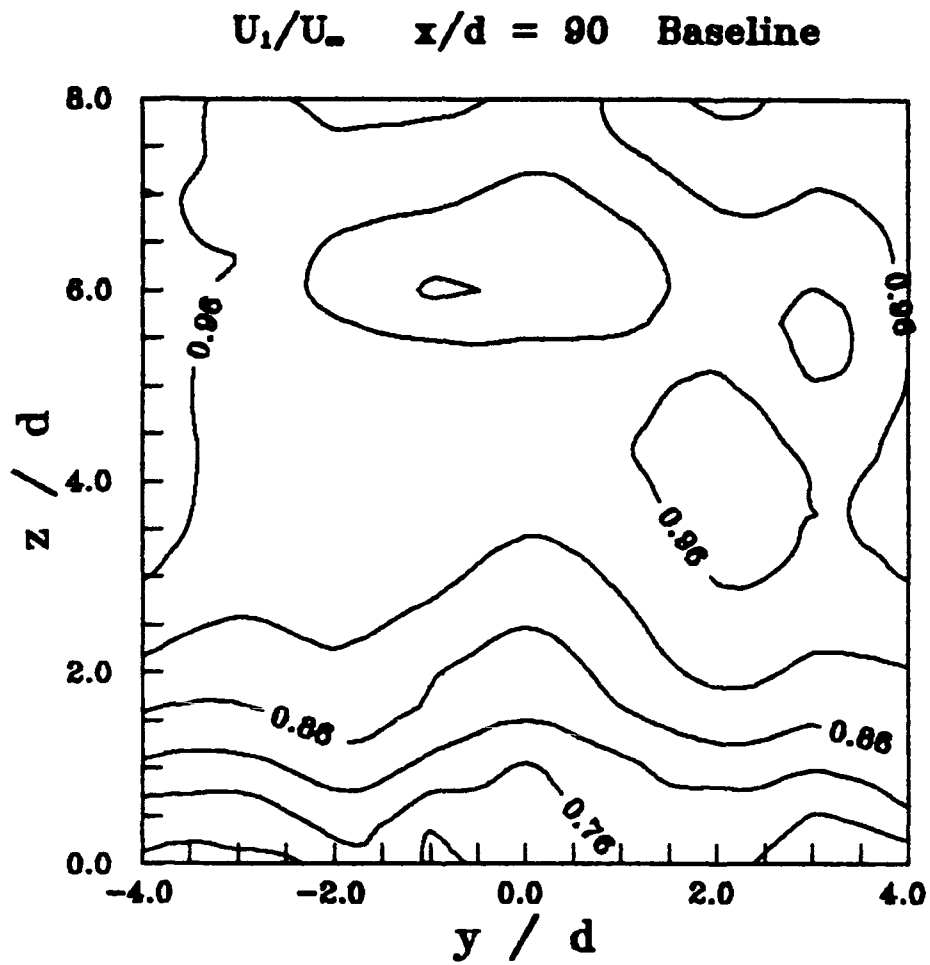


Figure 58. Velocity Contours, Baseline Injection,  $x/d = 90$

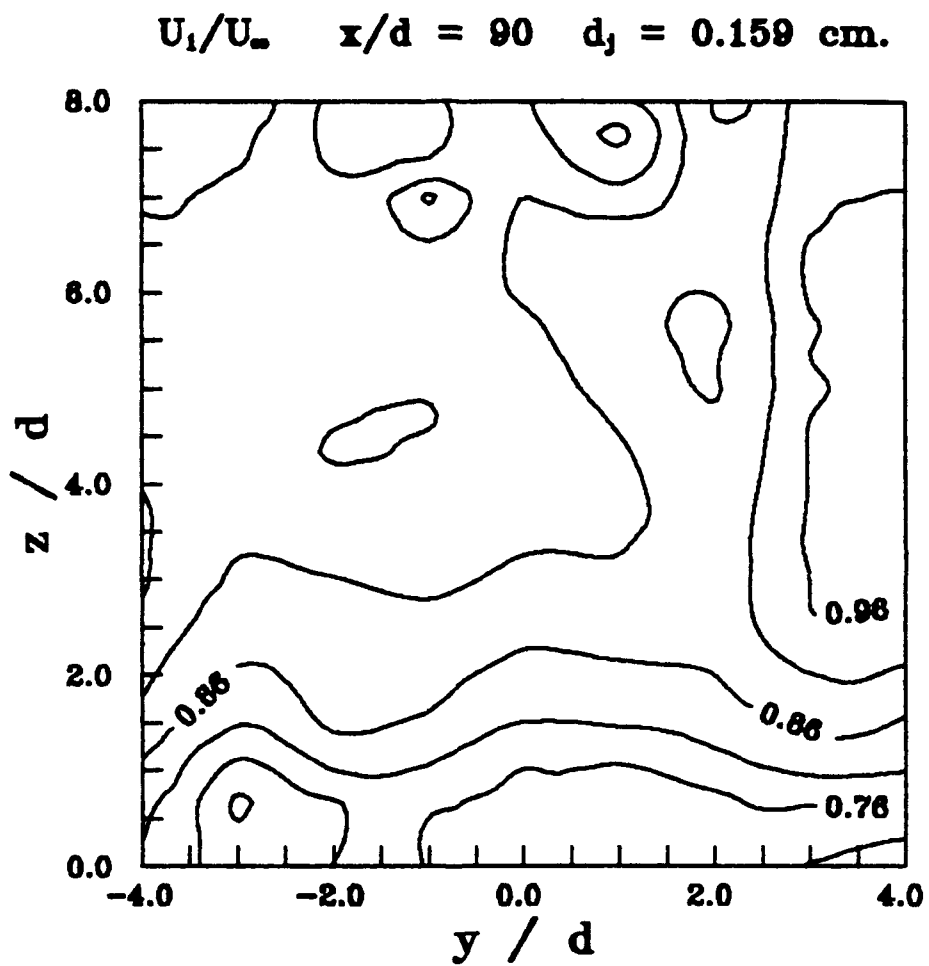


Figure 59. Velocity Contours, Combined Injection,  $x/d = 90$



$U_1/U_\infty$     $x/d = 90$     $d_j = 0.079$  cm.

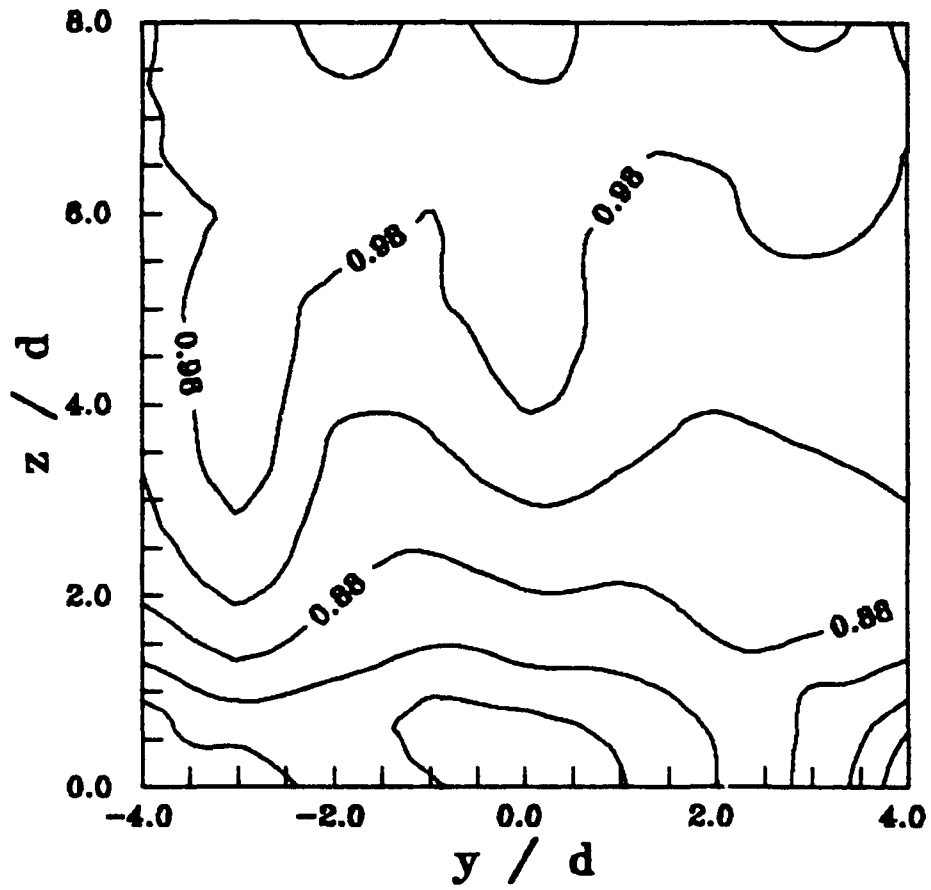


Figure 60. Velocity Contours, Combined Injection,  $x/d = 90$

$U_1/U_\infty$     $x/d = 90$     $d_j = 0.040$  cm.

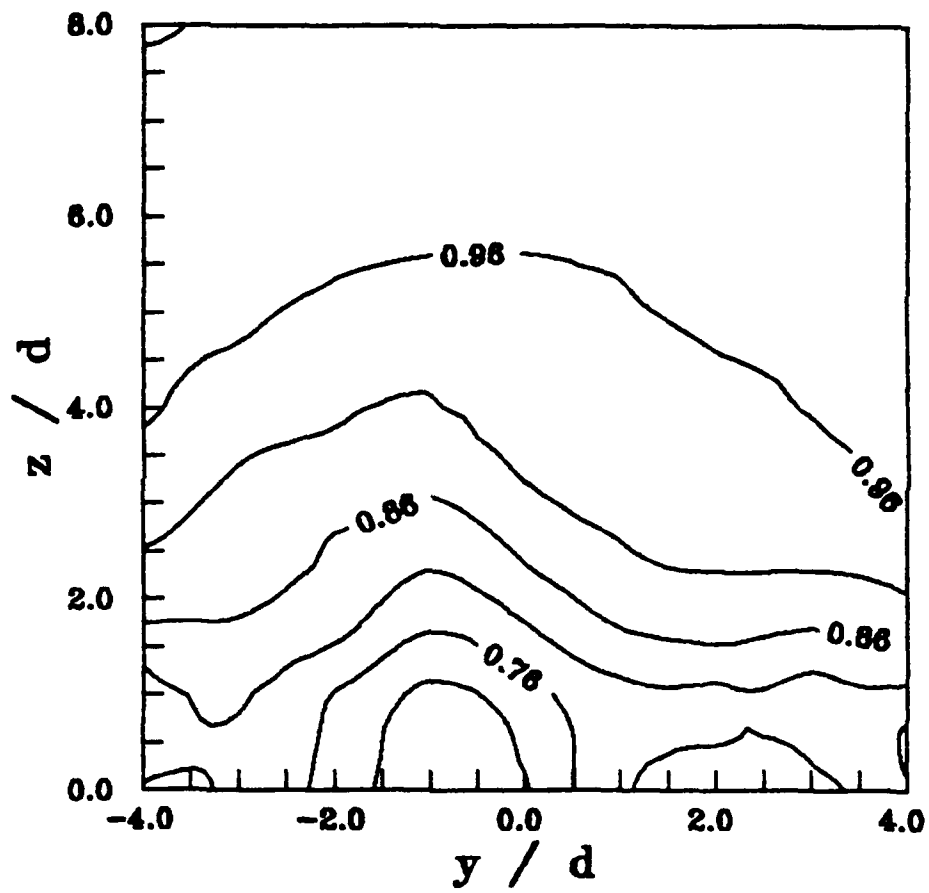


Figure 61. Velocity Contours, Combined Injection,  $x/d = 90$

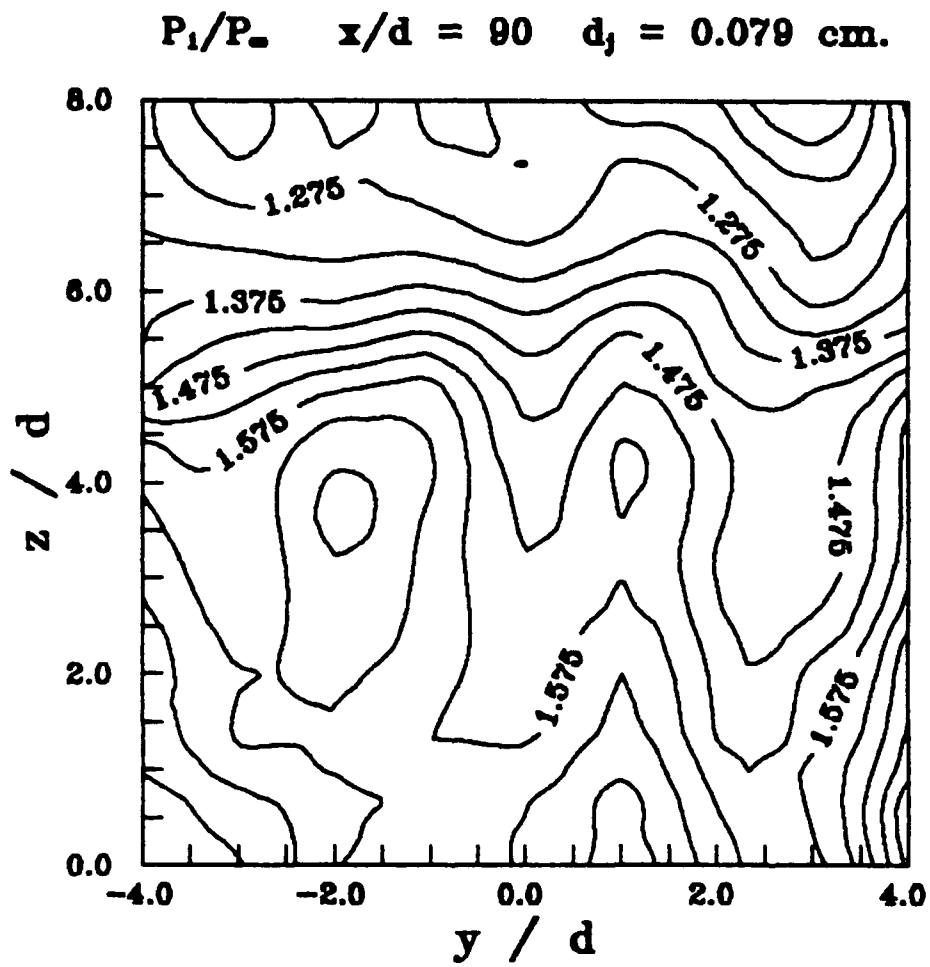


Figure 62. Typical Static Pressure Contours, Combined Injection,  $x/d = 90$

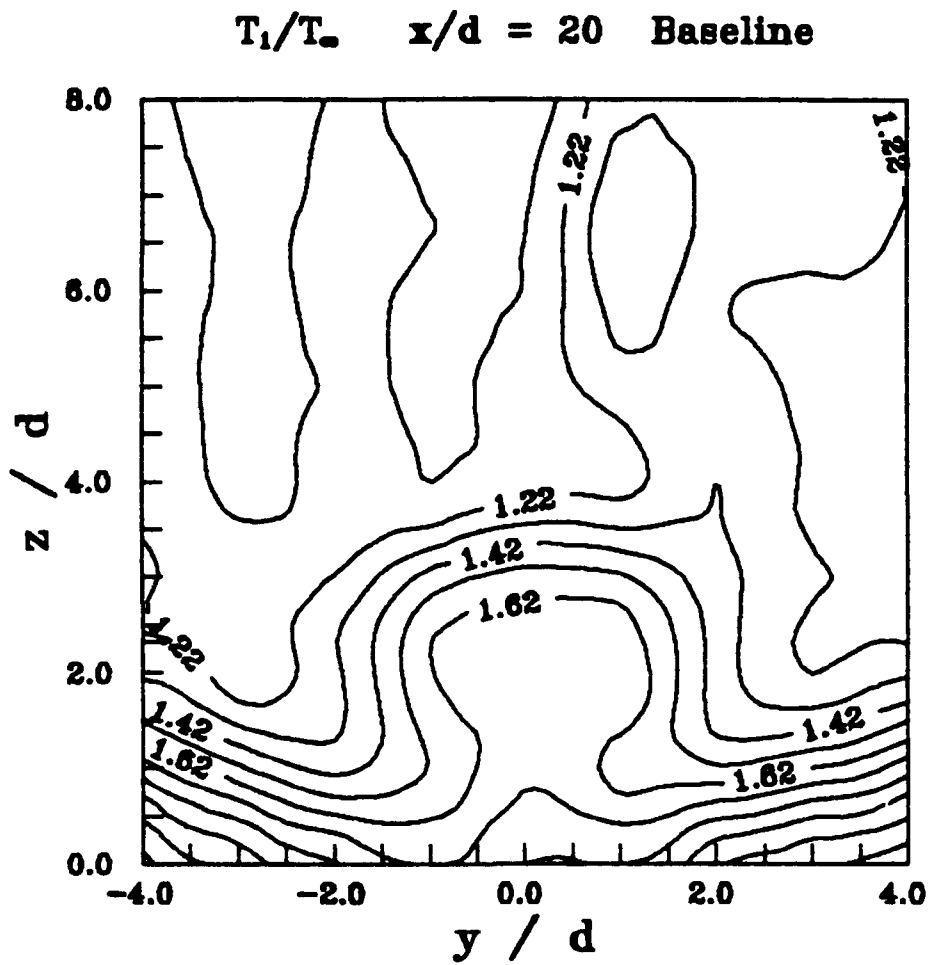


Figure 63. Static Temperature Contours, Baseline Injection,  $x/d = 20$

$T_1/T_\infty$     $x/d = 20$     $d_j = 0.159$  cm.

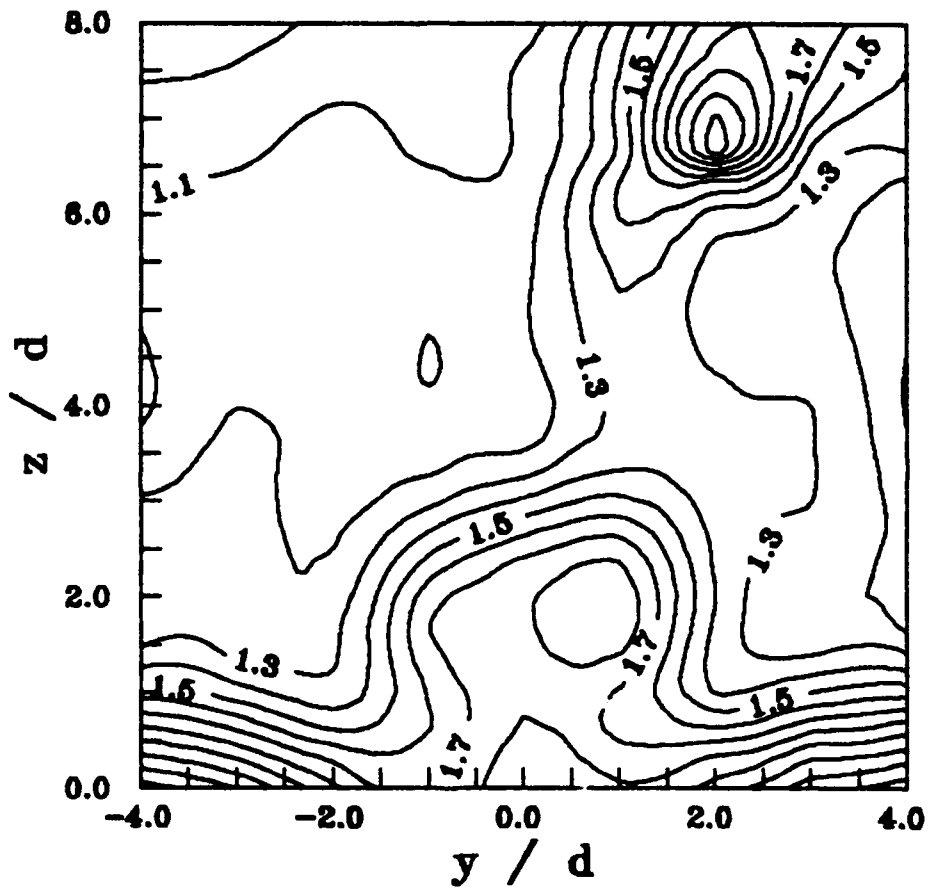


Figure 64. Static Temperature Contours, Combined Injection,  $x/d = 20$

$T_1/T_\infty$     $x/d = 20$     $d_j = 0.079$  cm.

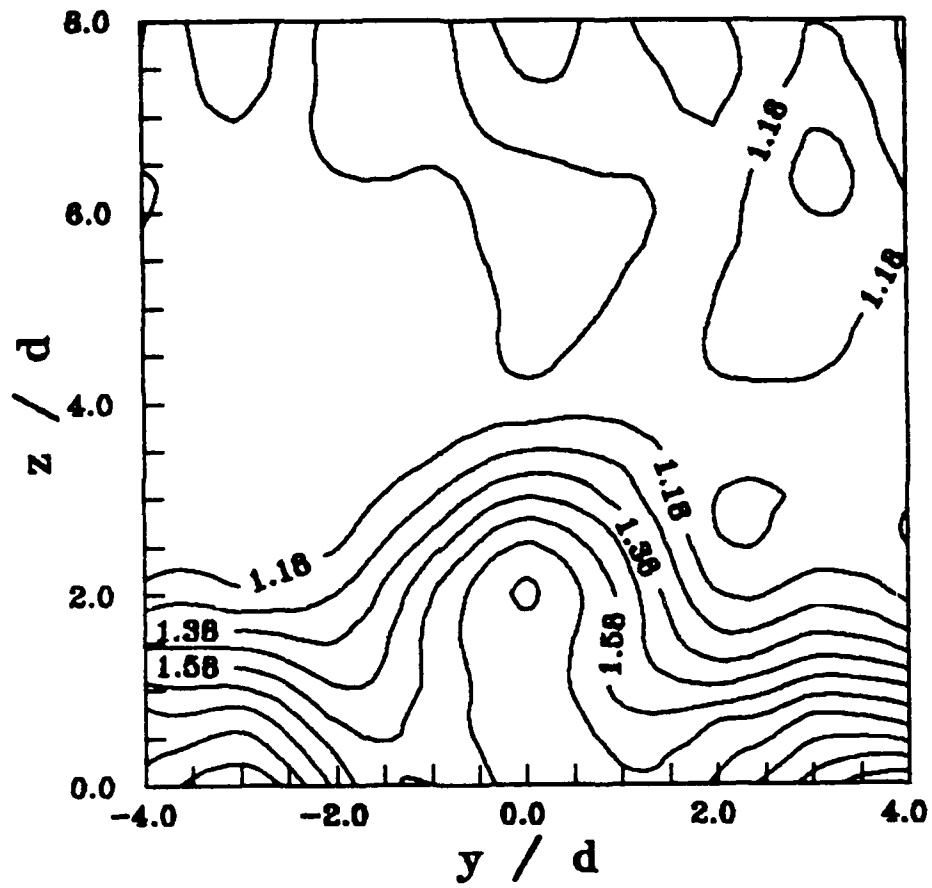


Figure 65. Static Temperature Contours, Combined Injection,  $x/d = 20$

$T_1/T_\infty$     $x/d = 20$     $d_j = 0.040$  cm.

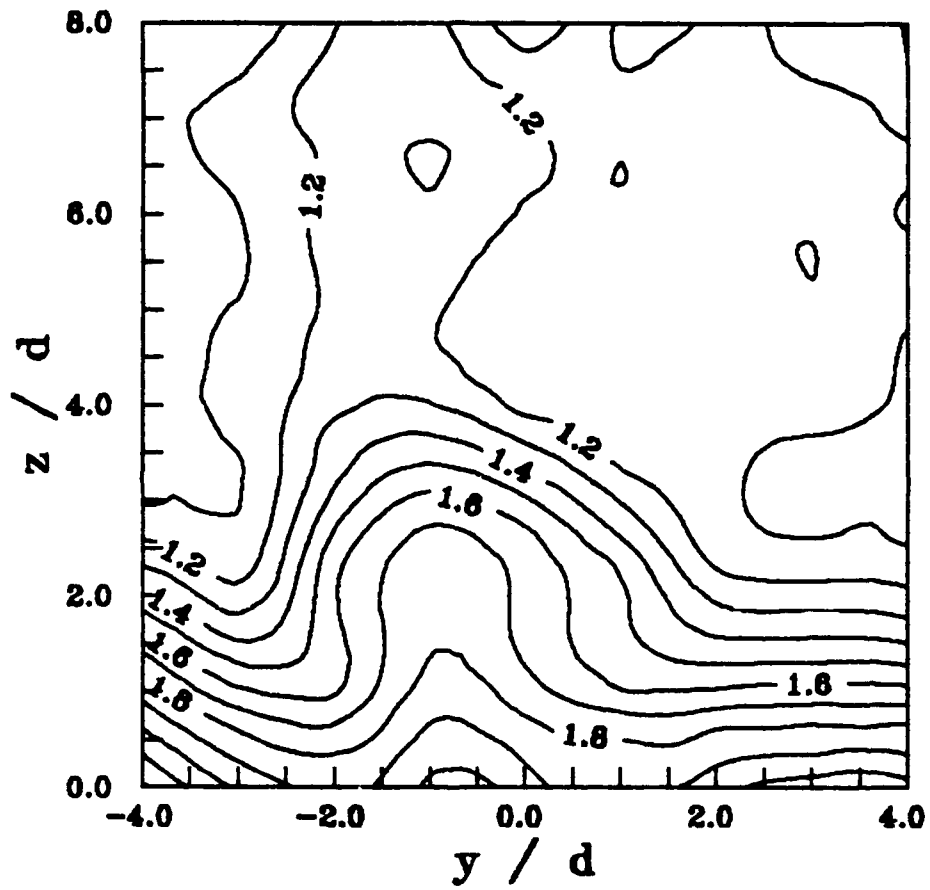


Figure 66. Static Temperature Contours, Combined Injection,  $x/d = 20$

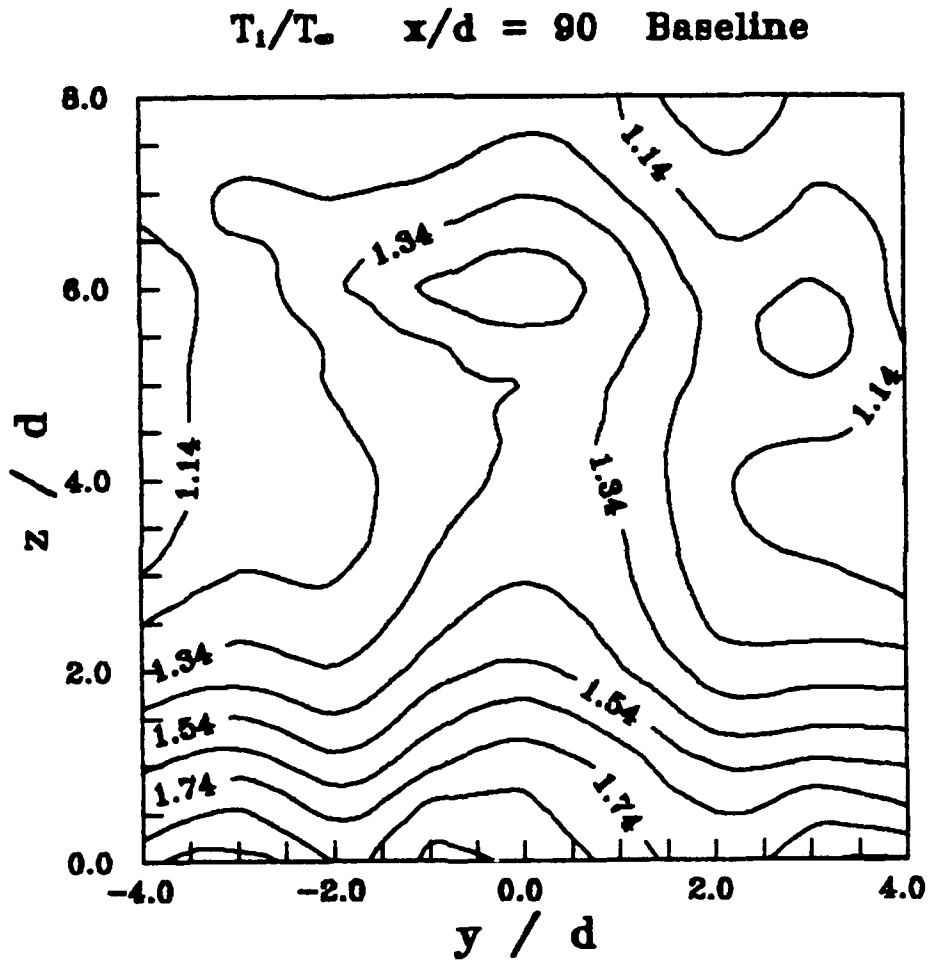


Figure 67. Static Temperature Contours, Baseline Injection,  $x/d = 90$



$T_1/T_\infty$   $x/d = 90$   $d_j = 0.159$  cm.

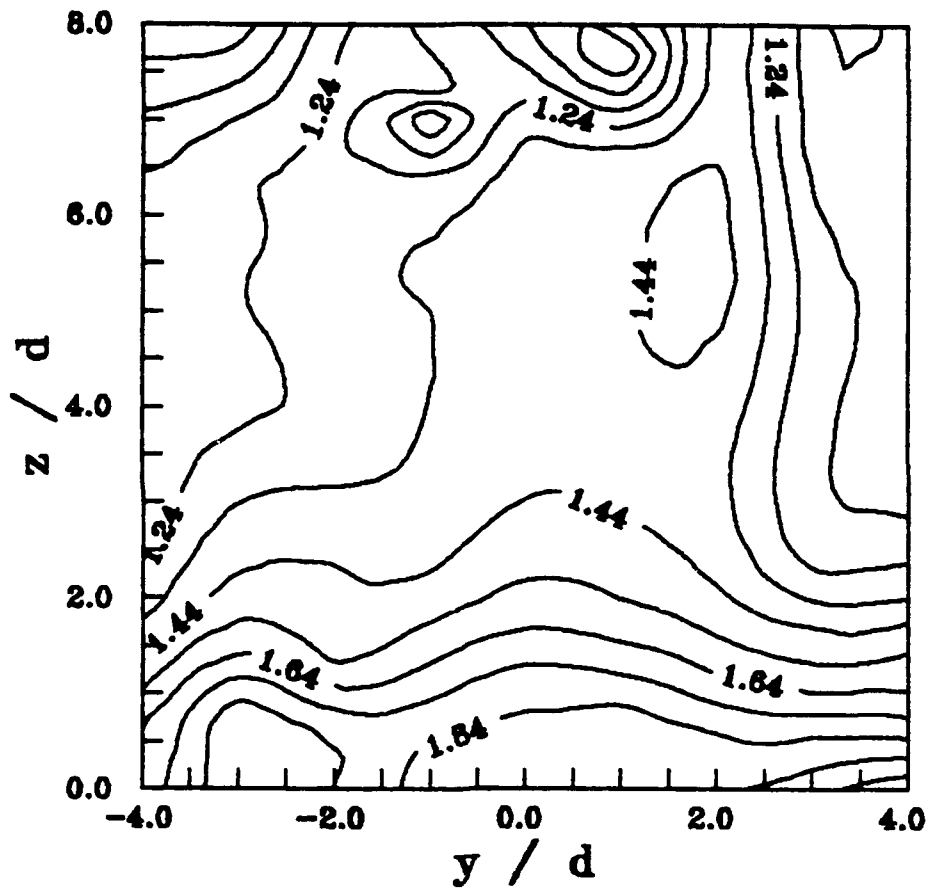


Figure 68. Static Temperature Contours, Combined Injection,  $x/d = 90$

$T_1/T_\infty$      $x/d = 90$      $d_j = 0.079$  cm.

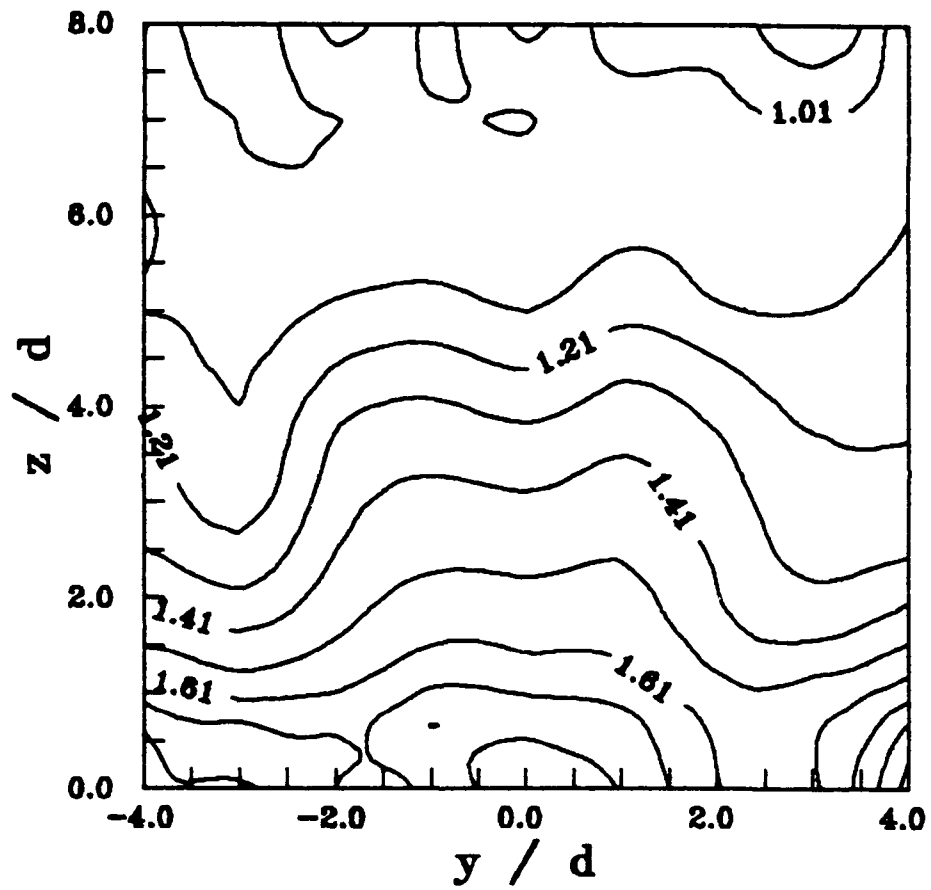


Figure 69. Static Temperature Contours, Combined Injection.  $x/d = 90$

$T_1/T_\infty$     $x/d = 90$     $d_j = 0.040$  cm.

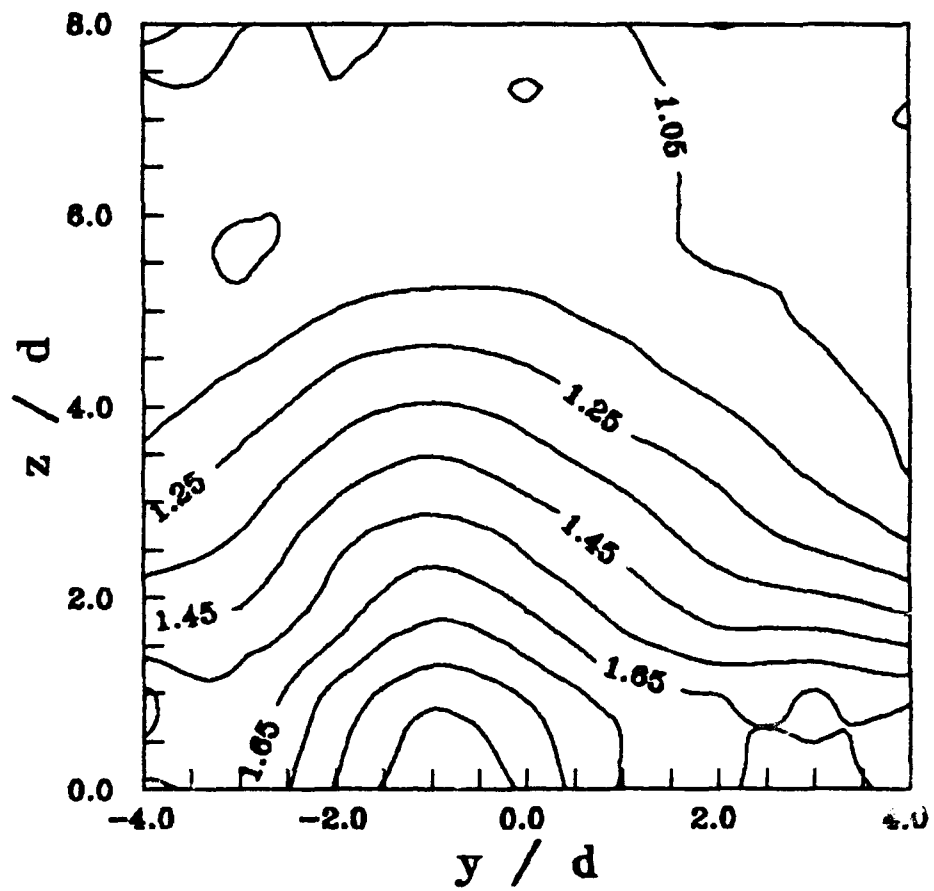


Figure 70. Static Temperature Contours, Combined Injection,  $x/d = 90$

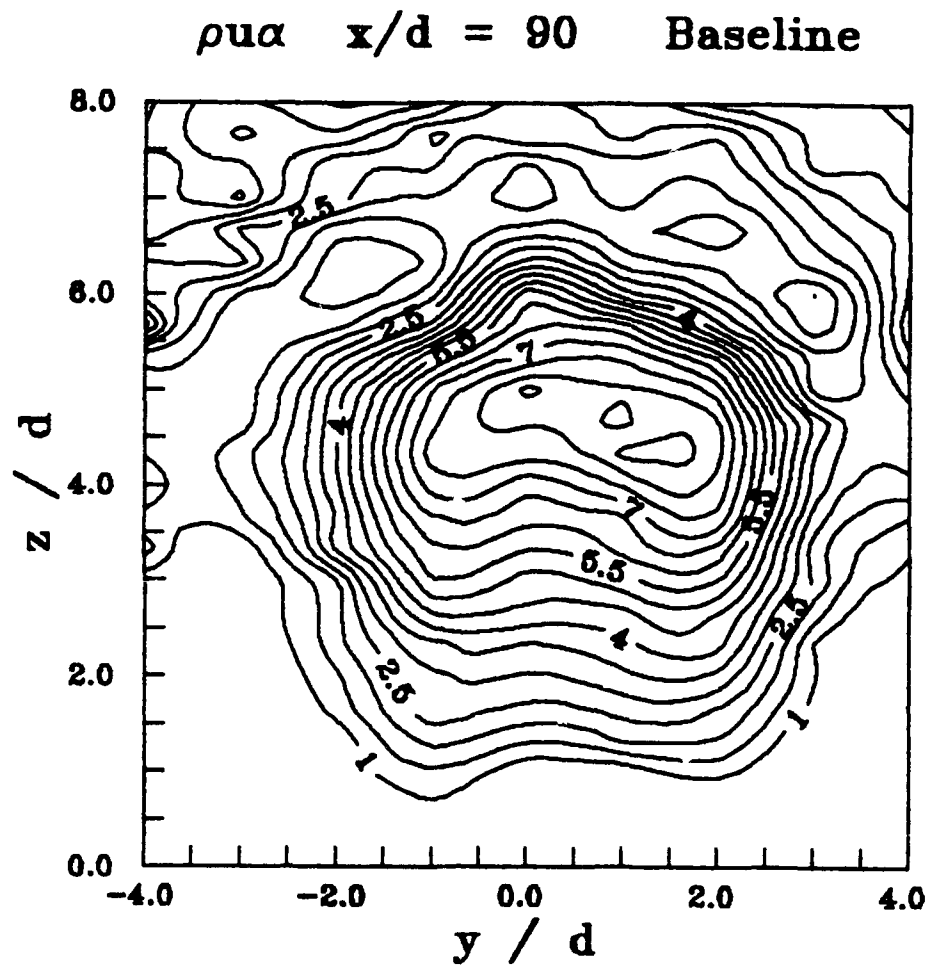


Figure 71. Helium Mass Flux, Baseline Injection,  $x/d = 90$

$\rho u \alpha \quad x/d = 90 \quad d_j = 0.159 \text{ cm.}$

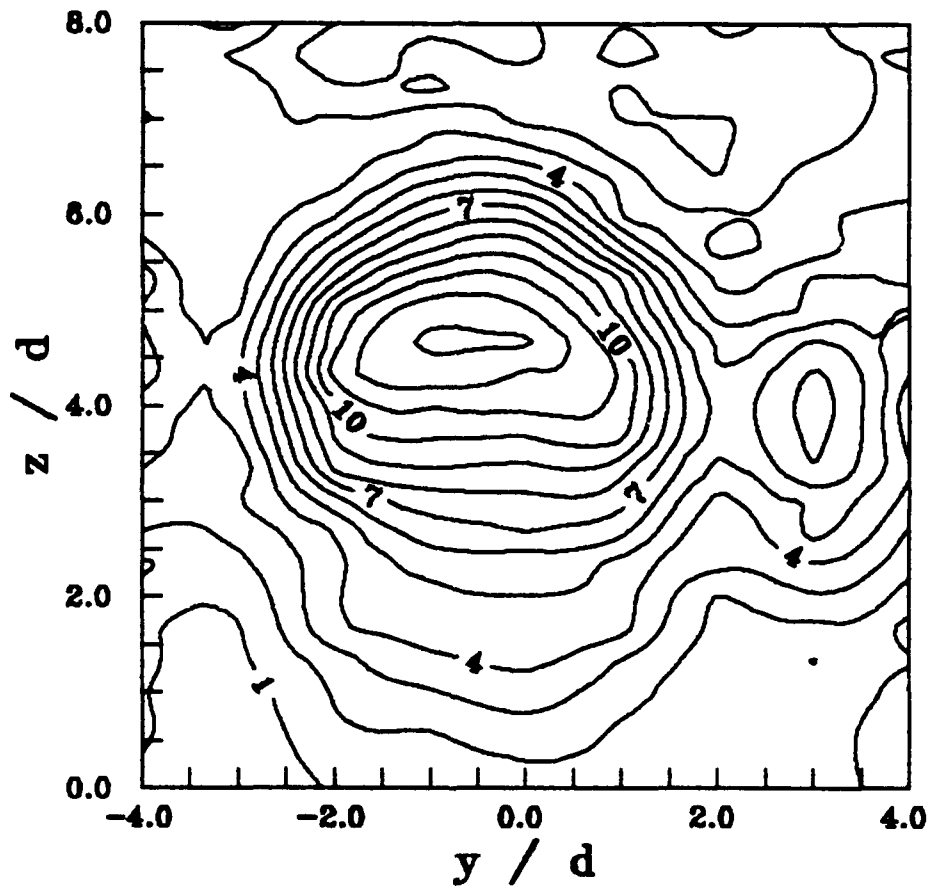


Figure 72. Helium Mass Flux, Combined Injection,  $x/d = 90$

$\rho u \alpha \quad x/d = 90 \quad d_j = 0.079 \text{ cm.}$

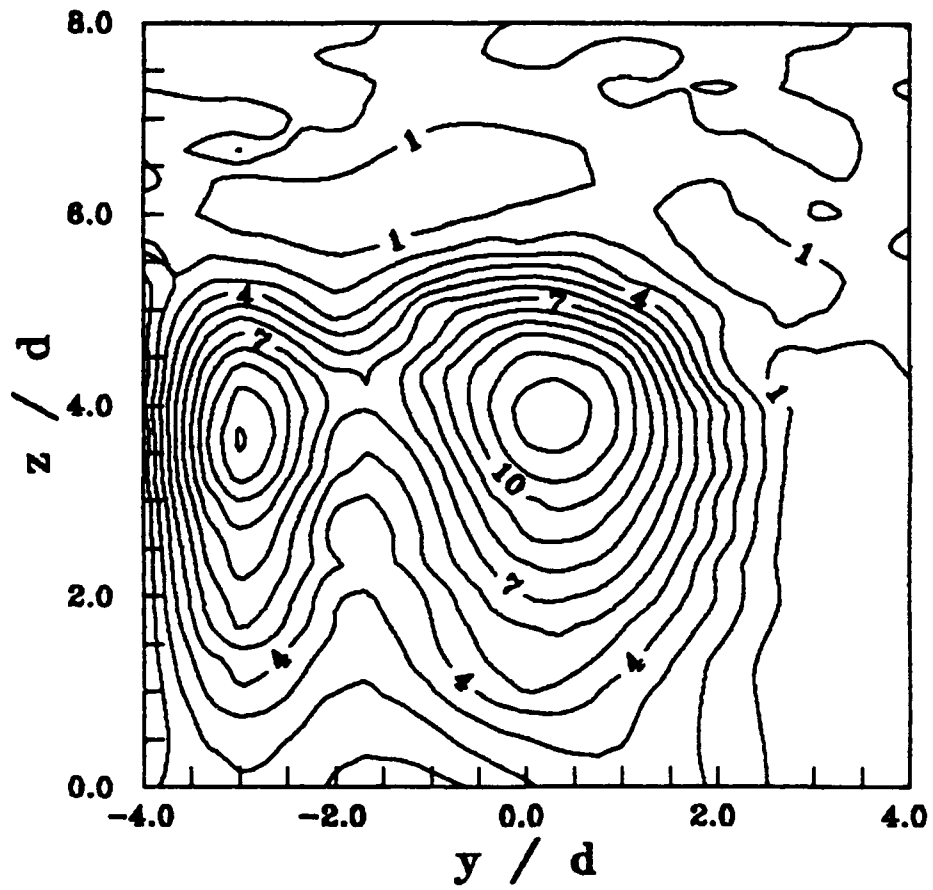


Figure 73. Helium Mass Flux, Combined Injection,  $x/d = 90$

$\rho u \alpha \quad x/d = 90 \quad d_j = 0.040 \text{ cm.}$

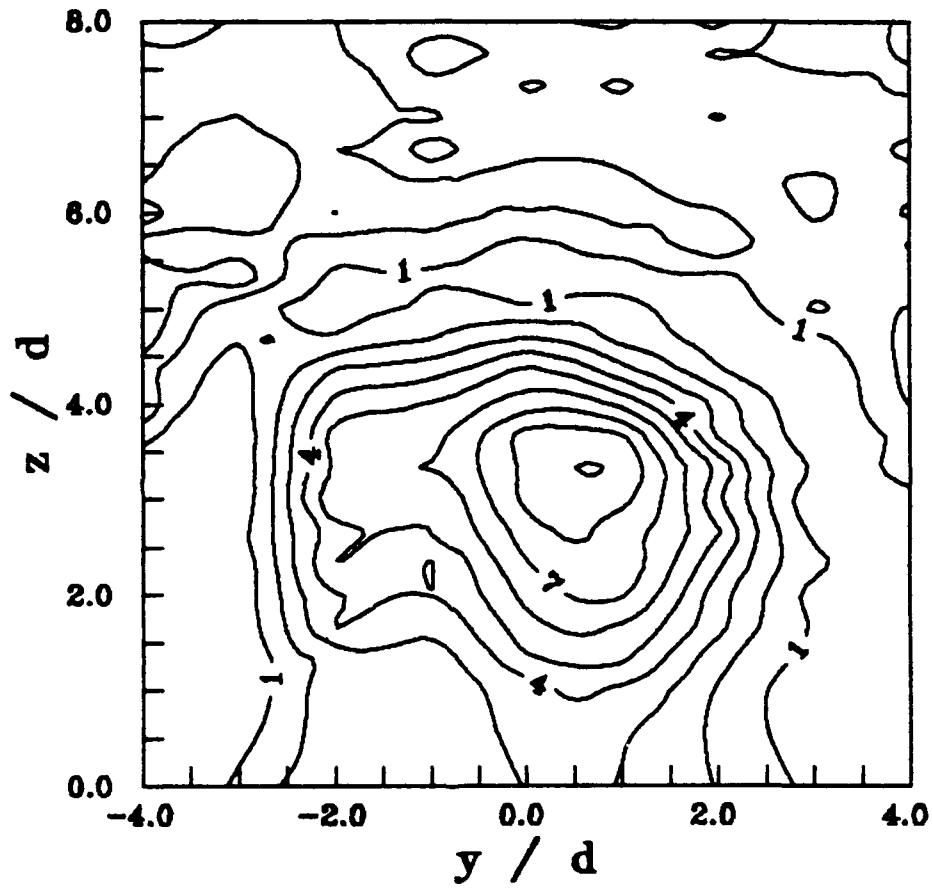


Figure 74. Helium Mass Flux, Combined Injection,  $x/d = 90$

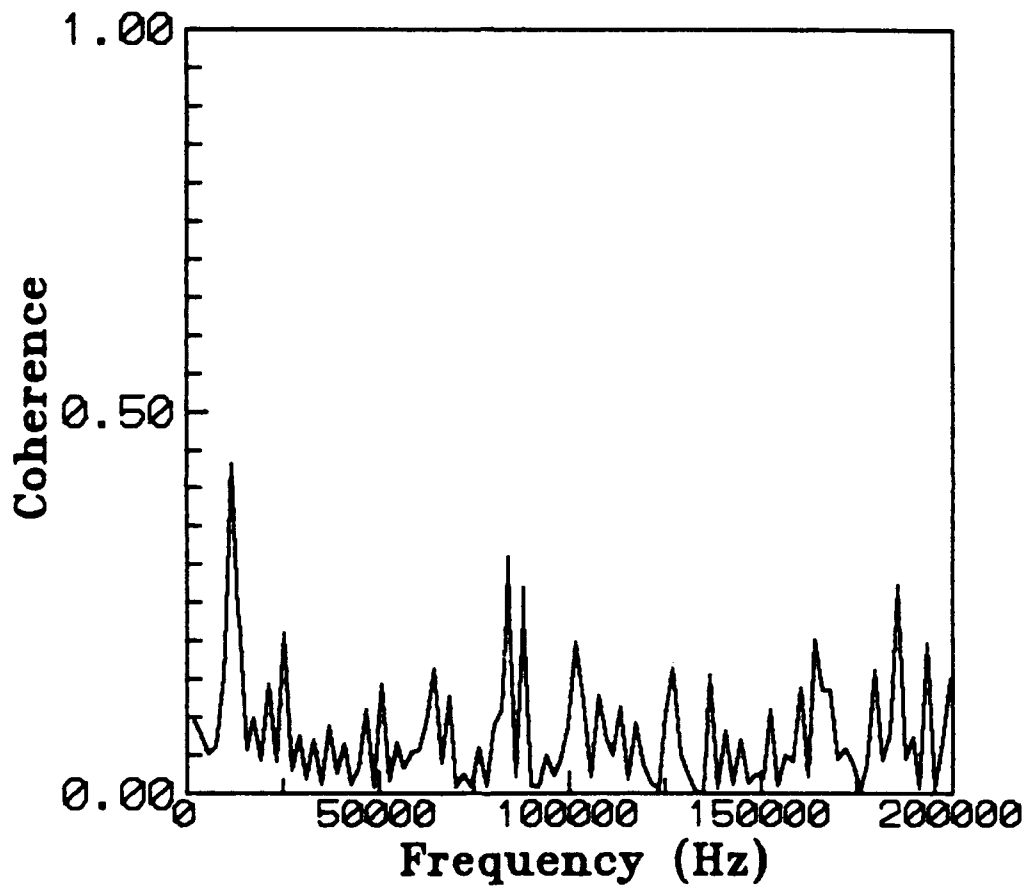


Figure 75. Coherence Function, Combined Injection ( $d, = 0.079$ )



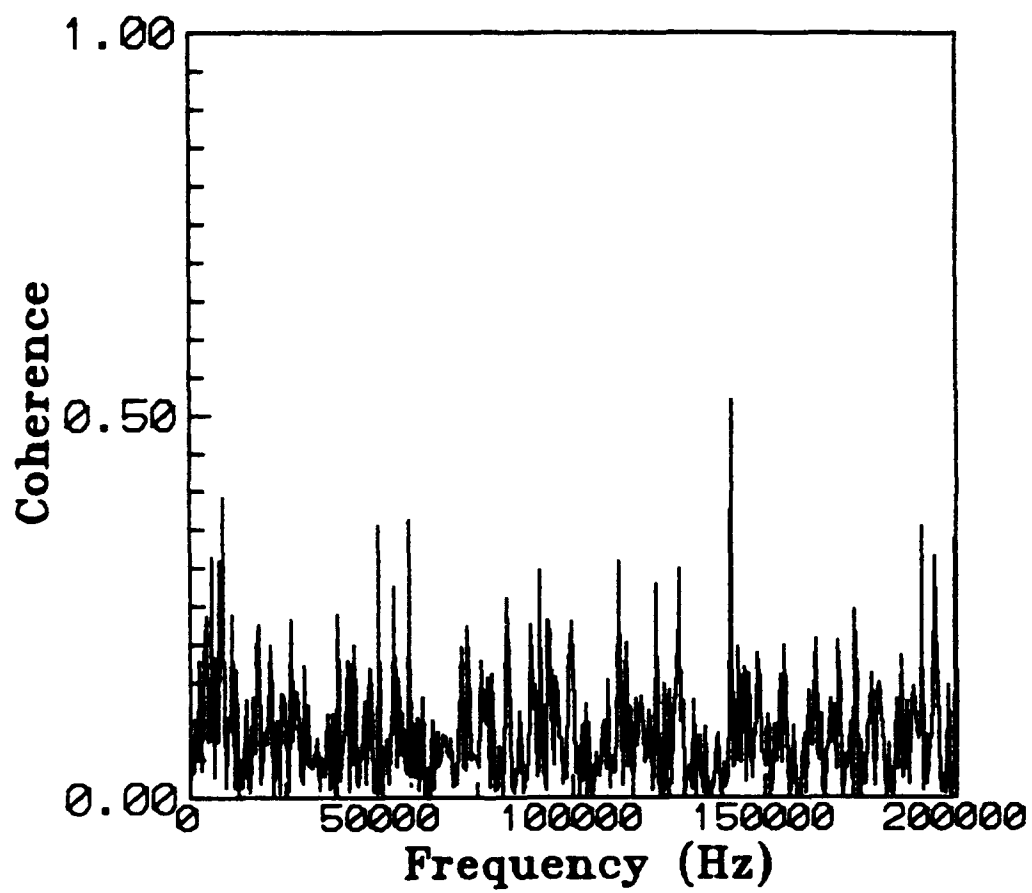


Figure 76. Coherence Function, Combined Injection ( $d, = 0.040$ )

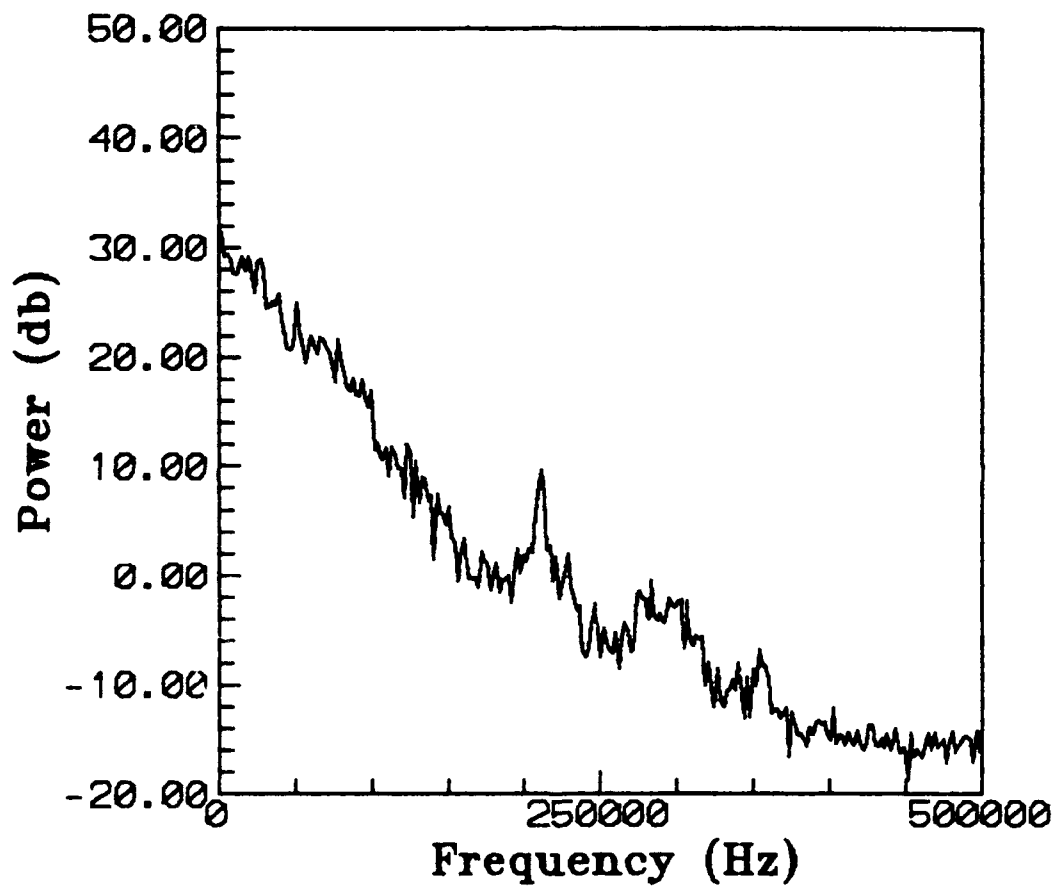


Figure 77. Hot-Wire Power Spectrum, Baseline Injection

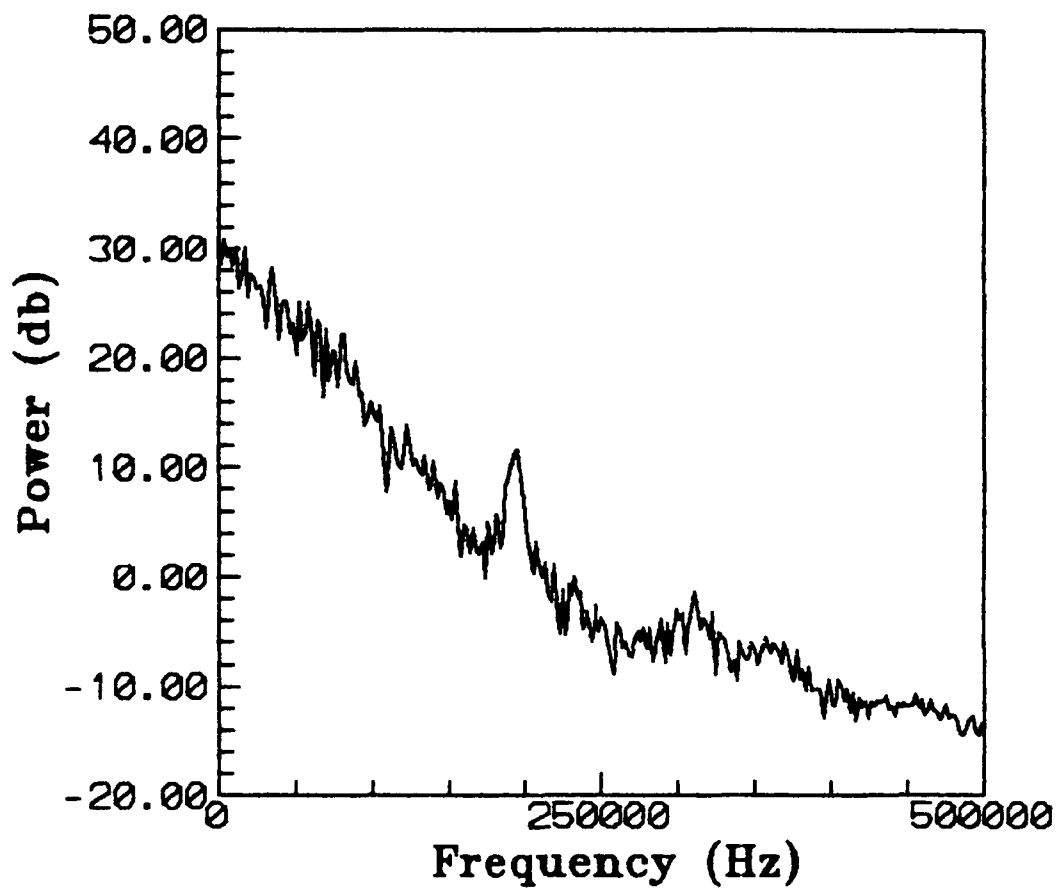


Figure 78. Hot-Wire Power Spectrum, Combined Injection ( $d, = 0.159$ )

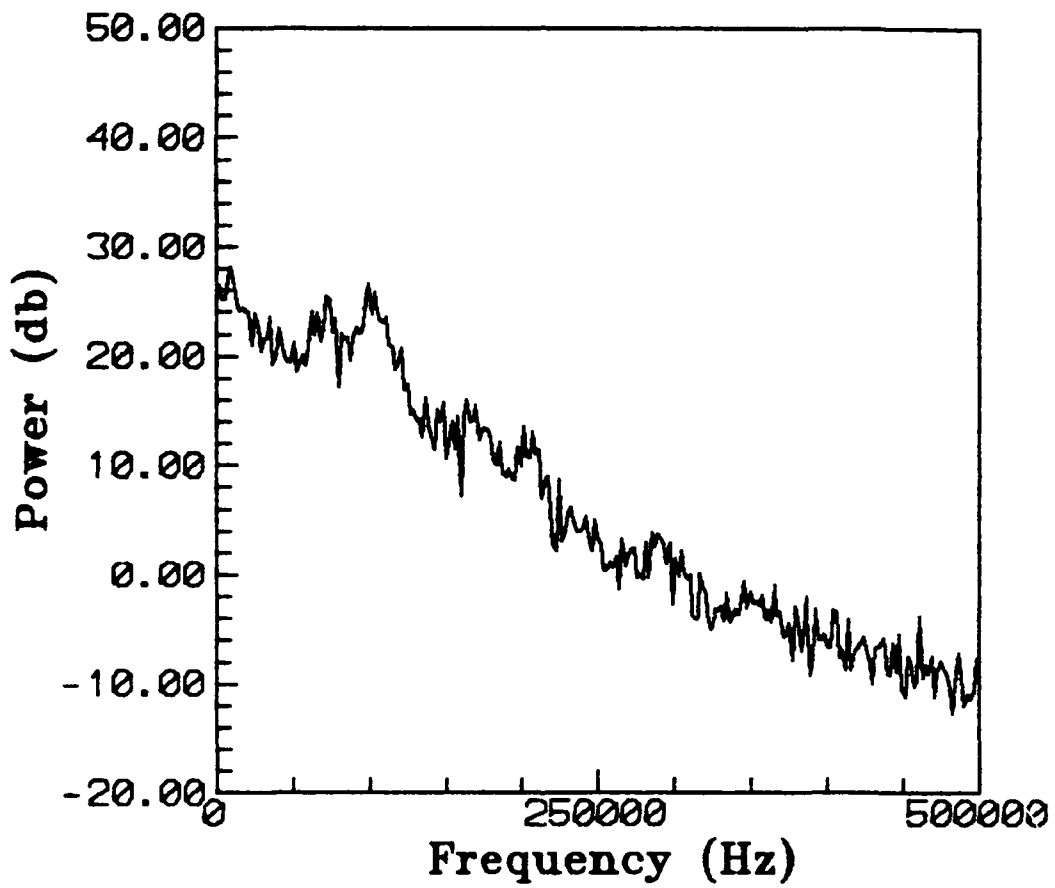


Figure 79. Hot-Wire Power Spectrum, Combined Injection ( $d, = 0.079$ )

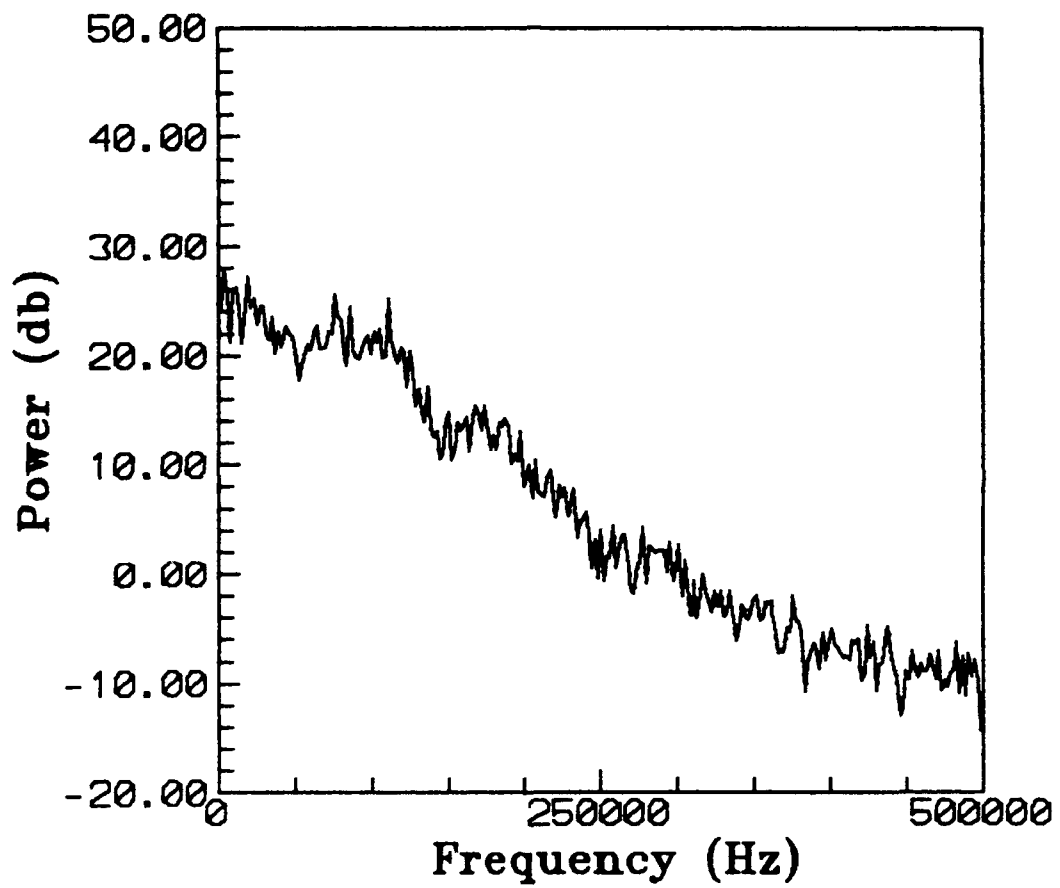


Figure 80. Hot-Wire Power Spectrum, Combined Injection ( $d = 0.040$ )

## APPENDIX A: ERROR ANALYSIS

As with any experimental investigation, the measurements taken and the calculations made from the data are subject to some errors. Some possible sources of error include: the tunnel control system, the helium and water injection control system, lateral and vertical displacement errors, probe characteristics and associated instrumentation, and electrical noise in instrumentation cables. There are also some errors due to the curve fit methods used in the data reduction procedures.

The wind tunnel maintained settling chamber total pressure to within 4% of its desired value. The tunnel total temperature also varied by about 4%. The helium supply system maintained plenum chamber pressure to within 4%. Water supply pressure was held to within 2%.

Probe vertical displacement errors were made up of a 0.5% error due to the LVDT<sup>21</sup>, a 0.6% error introduced by incorrect or faulty cathetometer readings and a 0.005% error due to errors in the curve fit generated from the probe calibration measurements. The sum of these three components gives a vertical displacement error of 1.1%. Lateral displacement errors were estimated at less than 5%.

Concentration probe errors resulted from probe measurement errors and curve fit errors. The concentration measurement error was found to be 2% in mole fraction. Another 3% error comes from the curve fit used in the concentration probe calibration and the interpolation routine used to determine the measured concentration. The result is an error in concentration measurement of approximately 5%.

Pressure measurement errors were the result of transducer performance and curve-fit errors. All pressure transducers were certified by the manufacturer to be accurate to within 1%. The errors due to calibration curve fits were on the order of 0.003% and were neglected based on comparison with other sources of error. Time response errors would cause a shift in the vertical profiles. The worst-case time response was 0.1 seconds for the cone-static probe. This was due to the small pressure taps and the small pressures being measured. At a probe speed of 3.8 mm/sec, this results in a shift of 0.38 mm. Combining this with the other LVDT errors gives a maximum total error of 0.7 mm or 2.3% of the normal traverse height.

The total temperature measurement errors were caused by insufficient venting area, heat loss through the supports and time response of the thermocouple wire. Due to the small total temperature variations encountered in these experiments, the time response of the thermocouple was neglected. A vertical shift would also cause very small errors in total temperature since the temperature gradients were small. The total error in temperature measurements was estimated at approximately 2%.

Errors in quantities derived from these measurements were the result of errors in probe measurement and errors in gas composition interpolation. These derived quantities are functions of gas composition through the gas constant,  $R$ , and the ratio of specific heats,  $\gamma$ . Interpolation errors were determined by putting a known gas composition into the data reduction program and comparing the output from the program with the input conditions. The errors due to probe uncertainties were investigated using the single-sample uncertainty analysis procedures of Kline and McClintock<sup>24</sup> and Moffat.<sup>25</sup> The two

sets of errors were combined to give the maximum expected error for each of the flow quantities and were found to be:

M	4.7%
P	9.1%
$P_t$	11.7%
$\rho U$	6.3%
T	7.7%
U	6.5%